Department of Precision and Microsystems Engineering

3D-printed piezoelectric micropump with ball valves

Xinyi Wang

Report no : 2024.086
Coach : Dr. Murali Ghatkesar, Dr. Tomas Manzaneque Garcia,
Dr. Victor Ruiz-Diez and MSc. Zhilin Wang
Professor : Dr. Vasso Giagka
Specialisation : Micro- and Nano- Engineering
Type of report : Master’s Thesis
Date : 14 October 2024

TU Delft
Delft University of Technology

Challenge the future

Master's Thesis

3D-printed piezoelectric micropump with ball valves

by

Xinyi Wang

Student Number
5695694

Supervisor:	Murali Ghatkesar Tomas Manzaneque Victor Ruiz-Diez
Daily Supervisor:	Zhilin Wang
Faculty:	Faculty of Mechanical Engineering, Delft

Contents

1

Introduction

The organ-on-a-chip (OoC) integrates biology with microtechnology to mimic human physiology in vitro [1]. In the OoC system, media are guided through micro-level channels towards the chip to mimic the in vivo microenvironment and recapitulate the functions of tissues cultivated in the chip. The OoC makes up for the shortcomings of conventional biological systems modeling and provides life science researchers with a new tool to explore human pathophysiology and disease. Although in vivo imaging has advanced rapidly in recent years, the investigation in organisms such as mice is still limited. Demonstrating physiological relevance is challenging due to the complex interactions between multiple organs. Additionally, models for in vitro cultures of 2D and 3D cells often lose significant in vivo relevance during experiments. Therefore, the OoC bridges these two technologies since it offers the possibility to culture complex organ systems in vitro. Currently, research in the OoC field has grown exponentially and extends beyond academia. Industries in pharmacy, cosmetics, food, and chemistry are investing efforts in building OoC systems. This is driven by the strong need for testing on humanized in vitro platforms, as opposed to using animals, allowing for direct observation of cell and tissue behavior.

An Organ-on-a-Chip (OoC) system includes reservoirs, microfluidic multiplexers (MUX), pumps, flow controllers, and an OoC hub [2]. Among these components, pumps work as the heart of the system by driving fluid to communicate between subsystems. Since the media flows in the human body are within the flowrates of ml/min and μl/min, devices are required to provide similar milli- or micro-level flowrates [3] and keep the media bubble-free and fluctuation-free to maintain the activity of the cells. To be more specific, flowrates vary for different OoC systems in the region between $1\mu l/min$ and $100\mu l/min$ [4]. Although traditional macro pumps such as syringe pumps can offer the required flowrate, their footprint is in centimeters. Compared to the chip, which has an external dimension of several millimeters, the peripheral system composed of macro-pumps is bulky. For example, the size of a lung-on-a-chip is that of a miniature stamp (75 $\times$ 25mm^2), while its peripheral fluid unit occupies benchtop space [4]. Complex peripheral fluid systems increase the workload by requiring the disconnection of tubing and cables for changes in media or flowrate. Additionally, they contribute to an increased dead volume in connecting tubes, posing challenges to long-term experiments and limiting the potential for complex OoC systems such as human-on-a-chip. Consequently, a need has emerged for the portability and miniaturization of pumps [2]. Since Lintel et al. invented the first miniature pump in the last century, several miniature pumps have been developed followed by [5]. The micropump operates through the periodic changes between suction mode and discharge modes, as illustrated in figure 1.1. In suction mode, the upward movement of the membrane decreases the pressure in the chamber due to the increase in the chamber volume. The internal pressure is lower than the atmospheric pressure, thereby drawing fluid in. Discharge mode is the opposite situation, the downward movement of the membrane increases the internal pressure and pushes the fluid out.

Figure 1.1: Micropump principle of operation: (a) suction mode and (b) discharge mode [2]

The micropump consists of three main components: an actuator, a chamber, and a flow rectifier. An actuator is required to change the chamber's internal volume, thereby changing the internal pressure. The piezoelectric actuator has superior performance due to its low power consumption and quick response time. The flow rectifier refers to the component that can determine the flow direction. A valve-based micropump directs fluid at low flow velocities (ml/min or µl/min) without introducing shear forces on the cells. However, the fabrication of such micropumps is complex. For example, Pan's design involved assembling thirteen different layers to form a micropump, resulting in a tedious fabrication process. 3D printing technology, as a newly emerging fabrication method, enables the manufacture of complex 3D geometries and simplifies the fabrication process. Besides, the exploration of ball valves is limited although it presents the potential for extremely high back pressure, leading to zero cross-contamination and pump valves almost never breaking due to clogging [6]. Therefore, the research question for this master's project arises: **How to manufacture a piezoelectric micropump with ball valves using rapid prototyping 3D printing technology?**

Chapter 2 will explain the state of the art of micropumps through various categorizations, including actuator types, flow rectifier types, and manufacturing methods. At the end of this chapter, the research gap in the literature will be identified, and the research question of this project will be introduced. Chapter 3 will detail the work of this project, focusing on the methodology and results of this 3D-printed piezoelectric micropump with ball valves. Following this, Appendix A presents the attempt at monolithic micropump fabrication and Appendix B provides supplementary materials for Chapter 3.

2

State of the art

2.1. Micropump

This chapter introduces the state of micropump technology. The categorization of micropumps is illustrated in the figure 2.1. Based on the driving force, micropumps can be classified as non-mechanically or mechanically actuated. As their name suggests, mechanical actuators convert mechanical energy into the kinetic energy of the fluid, whereas non-mechanical actuators derive the energy from other forms. For example, an electrochemical micropump, belonging to the non-mechanically actuated type, transports fluid through the expansion and reduction of gas bubbles in a reversible aqueous electrolysis electrochemical reaction [7]. Non-mechanically actuated micropumps mostly involve fluid properties to generate force, therefore facing limitations in fluid choice. Additionally, the reaction with the fluid can alter its properties, making non-mechanical actuators unsuitable for biomedical applications. Thus this report focuses on the mechanical actuators. The piezoelectric actuator stands out in mechanical actuators for its exceptional performance. According to different methods of controlling flow direction, piezoelectric micropumps can be further divided into valve-based and valve-less pumps. Due to structural differences, the types of micropumps are further subdivided and detailed explanations are provided below. Finally, the current manufacturing methods for micropumps will be discussed.

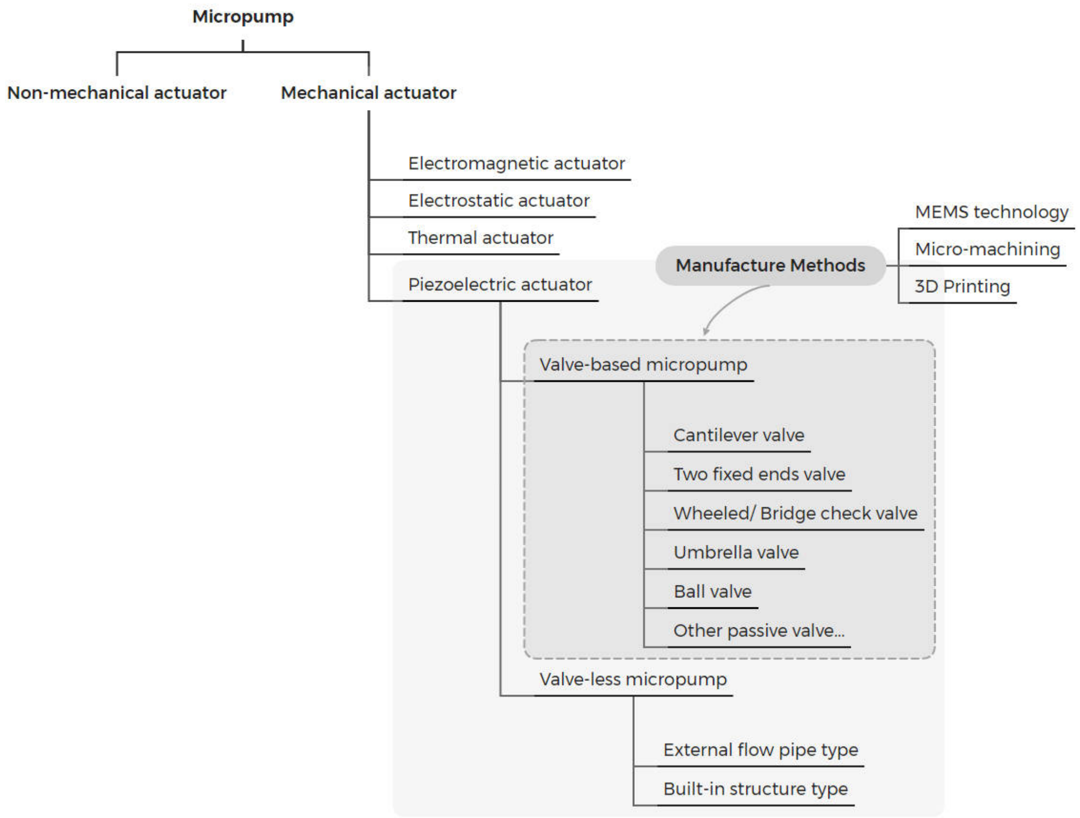

Figure 2.1: Categorization of micropump

2.1.1. Performance specifications

The significant specifications to evaluate the performance of the micropump include maximum flowrate, maximum backpressure, pump power, and efficiency [8]. The pump efficiency refers to the ratio between the electric power consumption in actuator $P_{actuator}$ and generated hydraulic power by pump P_{pump}.

$$\eta = \frac{P_{pump}}{P_{actuator}} \tag{2.1}$$

Where the maximum power generated by the pump relates to the maximum flowrate Q_{max} and maximum pressure p_{max} as shown in the equation below.

$$P_{pump(max)} = Q_{max} p_{max} \tag{2.2}$$

The maximum flowrate Q_{max} here refers to the volume of fluid per unit time flowing pass through the area A at zero backpressure as presented in equation 2.3. It can be calculated through the surface integration of flow velocity v.

$$Q = \frac{\mathrm{d}V}{\mathrm{d}t} = \int \int_A v \cdot \mathrm{d}A \tag{2.3}$$

The pressure exerted by the load device is referred to as the backpressure. The maximum backpressure P_{max} is the highest pressure from the load device that the micropump can withstand. At this pressure, the flowrate is zero. High backpressure ensures that no fluid backflow occurs when the pump is shut down, thus protecting the system and maintaining the desired fluid distribution.

To achieve a higher pumping efficiency, a higher flowrate and backpressure and lower power consumption are expected.

2.1.2. Actuation types

According to the operation methods, the mechanical actuators can be further divided as electromagnetic, electrostatic, thermo-pneumatic, shape memory alloy, and piezoelectric actuator [9].

Electromagnetic actuators

Electromagnetic actuators work through the principle that an energized coil produces a magnetic field. In this kind of micropump, a permanent magnet is installed on the top of the membrane or embedded in it and a solenoid (external magnet) with electronic assembly housing is put on top of the membrane as shown in figure 2.2 [10]. When current flows through a solenoid, the interacting magnetic fields of the permanent magnet and the magnetic field generated on the solenoid produce magnetic forces. The force attracts or repels depending on the direction of the current, and this force causes the membrane to vibrate, thus pumping the fluid in the channel.

Electromagnetic actuators can achieve a large deflection of the membrane. Additionally, since the electromagnetic field appears and dissipates quickly, these actuators can operate with a fast response. While this type of actuator requires an additional cooling structure to dissipate the generated heat, the significant electromagnetic interference further limits its application in biomedical fields [10].

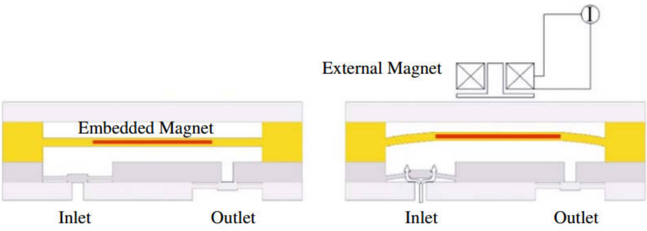

Figure 2.2: Electromagnetic actuation micropump [10]

Electrostatic actuators

Electrostatic actuators based on Coulomb force induce the displacement between two charged bodies as shown in the equation 2.4, where ε_0 is the permittivity of the air, A is the plate area, V is the applied voltage, d is the air gap.

$$F = \frac{\varepsilon_0 A V^2}{2d^2} \tag{2.4}$$

According to this theory, there are two parallel charged plates used, one of which is stationary while the other is movable as shown in figure 2.3. The magnitude of air gap d between two plates depends on the applied voltage V. When the applied voltage disappears, the displaced membrane loosens and returns to its initial position. Along the applied voltage switching periodically, the moving plate continues to vibrate. The membrane of the micropump is fixed on the moving plate and follows its movement to pump the fluid.

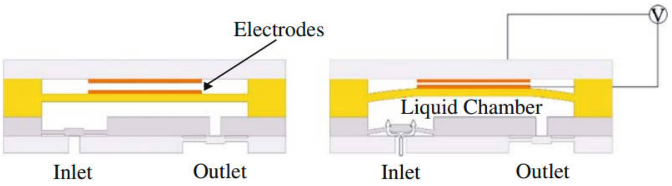

Figure 2.3: Electrostatic actuation micropump [10]

Electrostatic actuators are widely used in microdevices including micropump, microvalves, micro motors, and micro mirrors with the advantages of lower power consumption, wide operating frequency range, and convenient control. This type of actuator encounters a major limitation as a small deflection stroke that under an applied voltage of $200V$, the electrodes move only 5μm [10]. This characteristic limits the potential to further increase the flowrate [11].

Thermal actuators

Thermal actuators include thermopneumatic actuators and shape-memory actuators. Thermo-pneumatic actuators utilize the thermally induced expansion caused by volume or phase changes in the liquid sealed within the cavity, as illustrated in figure 2.4 [9]. The change in pressure ΔP with increasing temperature ΔT can be expressed by the equation 2.5, where E is elastic modulus, β is the thermal expansion coefficient and $\Delta V/V$ is the volume change percentage. This pressure change in the cavity periodically actuates the membrane motion.

$$\Delta P = E(\beta \Delta T - \Delta V/V) \tag{2.5}$$

The thermo-pneumatic actuators induce large deflections in the membrane, especially when the thermal actuators operate through a liquid-gas phase change. However, their multiple shortcomings limit the applications. Firstly, thermal actuators require high power consumption and suffer from slow response times, as heat conduction and temperature changes take time. Furthermore, the amount of generated heat can affect the media in the channel as well as the operating environment [9].

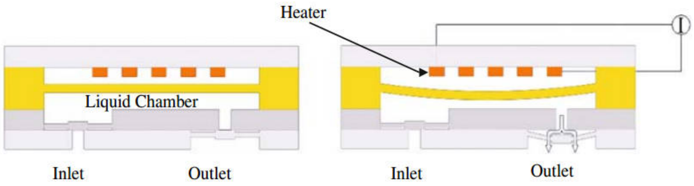

Figure 2.4: Thermopneumatic actuation micropump [10]

Shape Memory Alloy (SMA) material, illustrated in figure 2.5, can serve as a thermal actuator driven by two solid-phase transitions: austenite and martensite. SMA material at low temperatures appears as martensite, which has higher ductility than austenite, as well as withstanding higher deformation [12]. Therefore, the material is deformed by applying a bias pressure and constrained at the two ends. When the material is heated up and reaches the phase transformation temperature, it recovers to the original flat shape. This phase-driven deformation causes the upward or downward movement of the membrane. The commonly used SMA alloys include AuCu, InTi, and TiNi.

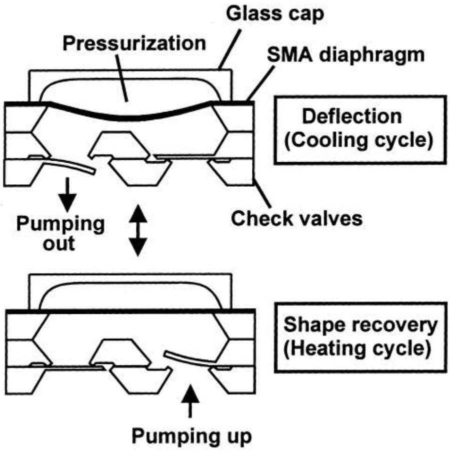

Figure 2.5: Shape memory alloy actuation micropump [12]

Although capable of generating a large stroke and possessing high damping capabilities, SMA actuators face a problem similar to that of thermopneumatic actuators, in that they require high power consumption and are unable to operate at high frequencies due to low cooling efficiency. In addition, the high-temperature sensitivity of SMA actuators makes it difficult to accurately control the deformation they produce.

Piezoelectric actuators

Piezoelectric actuators work on the principle that piezoelectric materials induce a strain under an applied voltage due to their polarized crystal structure. The structure of the piezoelectric actuation micropump is illustrated in the figure below. The magnitude of this induced strain relates to the coupling d between the strain and the electric field as shown in equation 2.6. This piezoelectric coupling is a 6×3 matrix in most of the piezoelectric materials, while d_{31} and d_{33} in this matrix are mainly used. In d_{31} mode, the electric field is applied in the vertical direction (3), and the strain forms along the horizontal direction (1) as shown in figure 2.6. In contrast, d_{33} mode refers to the vertical direction (3) voltage causes the vertical deformation (3) as shown in figure 2.7.

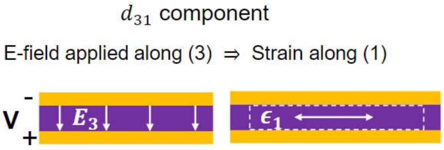

Figure 2.6: d_{31} mode

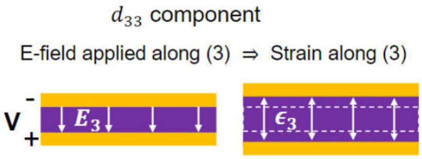

Figure 2.7: d_{33} mode

Conventionally, micropumps operate in the d_{31} mode as shown in figure 2.8, fixing the bottom of the piezoelectric material to the top of the membrane. When voltage is applied, the horizontal elongation in the piezoelectric material causes the membrane a bending moment similar to a bi-morph, making it move in the vertical direction. While micropump working on d_{33} is shown in figure 2.9. This kind of piezoelectric micropump constrains the piezoelectric material from the top with a rigid plate.

$$\epsilon = s^E \sigma + dE \tag{2.6}$$

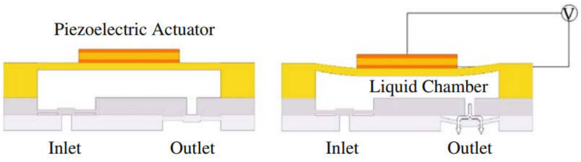

Figure 2.8: Piezoelectric micropump working on d_{31} mode [10]

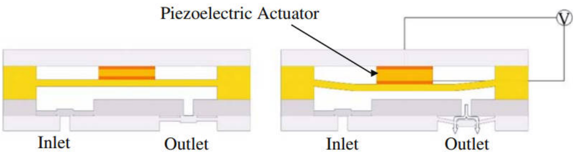

Figure 2.9: Piezoelectric micropump working on d_{33} mode [10]

Piezoelectric actuators are promising for MEMS applications because of their low power consumption, accurate control, and quick response. [11]. However, the major shortcoming of the piezoelectric actuator is its high driving voltage requirement. To produce sufficient deformation, the working voltage of most piezoelectric actuators is higher than 100V, although its power consumption may be low [10].

Comparison of actuators types

Figure 2.10 summarizes the performance of previously reported micropumps driven by different kinds of actuators [10]. Piezoelectric actuators stand out for achieving high backpressure and flowrate. In addition, other actuators face specific limitations that hinder their applicability in biology, such as electromagnetic interference in electromagnetic pumps, thermal effects on the environment, and poor control ability in either thermal-pneumatic or SMA pumps. Although electrostatic actuators are free from these limitations, their low deformation capability limits the potential to achieve high flowrates in micropump. Therefore, why not use piezoelectric micropumps in this project, which have the potential for high performance in both high backpressure and large flowrate? The only minor issue to consider is the high actuation voltage, which is acceptable compared to other types of actuators. Therefore, a piezoelectric actuator is chosen.

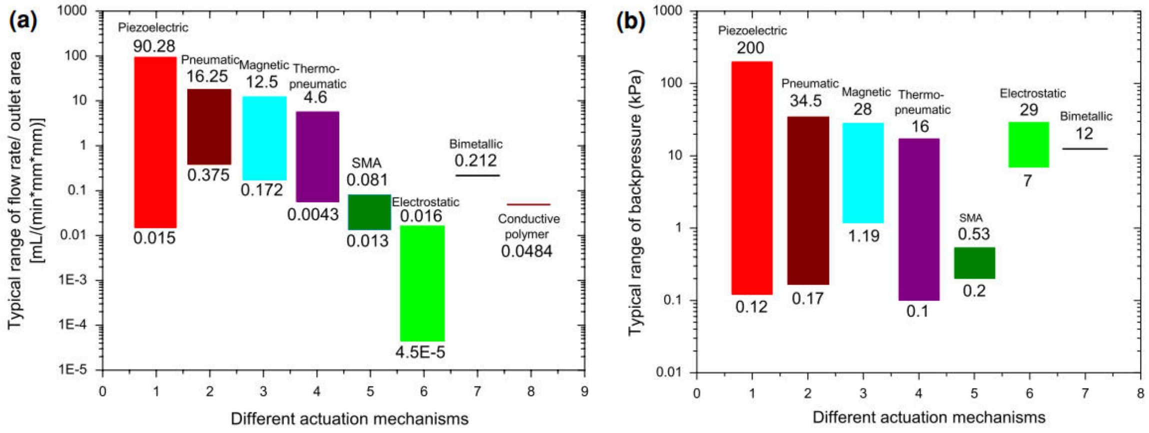

Figure 2.10: (a) Maximum flowrate and (b) maximum backpressure for micro pumps driven by different types of actuators [10]

2.2. Piezoelectric micropump

As previously mentioned, the piezoelectric micropump is driven by the coupling between electric energy and mechanical energy of the piezoelectric material. This kind of micropump has two working modes, suction mode and discharge mode, as illustrated in figure 1.1. The motion of the piezoelectric material is controlled by changing the magnitude and polarity of the applied voltage. In the suction mode, the membrane is actuated by piezoelectric material and forms an upward motion. Due to the increase in the chamber volume, the chamber pressure becomes lower. The lower chamber pressure compared with the atmospheric pressure pumping fluid in through two open channels. The existence of the valves is to control the fluid direction. With the valve at the inlet open and at the outlet closed, fluid flows from the inlet channel solely. Despite the use of valves, flow rectifiers serve as an alternative method for controlling the direction of fluid flow, which will be further explained in the following chapter. In the discharge process, the fluid is pumped out through the open outlet valve by the upward movement of the membrane.

The flowrate, as one of the important performance indicators, depends mainly on the vertical deformation of the membrane caused by the piezoelectric material. The d_{31} mode is preferred for its ability to enhance vertical deformation and achieve greater deflection. Based on d_{31} mode, Linnemann et al. conducted a simplified theoretical calculation of flowrate as shown following, not accounting for the effects of valves and membranes, and assumed that the stroke volume for each cycle of the micropump is the spherical deformation volume of the circular piezoelectric material [13]. Also, the micropump was assumed to work at its resonance frequency, where the vertical deflection in the piezoelectric actuator is maximal at a specific applied voltage U.

Based on these assumptions, the longitudinal deformation in the piezoelectric material can be described by the following equation, where represents the initial length of the piezoelectric material.

$$\frac{\Delta l}{l} = s^E \sigma + d_{31} \frac{U}{t} \tag{2.7}$$

The vertical deflection $w(r)$ on piezoelectric material can be calculated by equation 2.8, where R_p is the radius of a circular piezo disk.

$$w(r) = -\frac{3 d_{31} U}{t^2} R_p^2 (1 - \frac{r^2}{R_p^2}) \tag{2.8}$$

The maximum deflection is achieved at the center ($r = 0$) of the piezo disk as shown in equation 2.9.

$$w_{max}(r = 0) = -\frac{3 d_{31} U}{t^2} R_p^2 \tag{2.9}$$

The stroke volume V_0 can be achieved through the integrating of equation 2.9.

$$V_0 = -\frac{3\pi}{2} \frac{d_{31} U}{t^2} R_p^4 \tag{2.10}$$

Therefore, the flowrate generated is calculated as follows, where V_0 is the stroke volume and f is the frequency (pumping cycles per unit time). This flowrate is based on a simplified calculation that only considers the influence of the piezoelectric actuator and does not take into account the valve structure and membrane dimensions.

$$Q = V_0 f \tag{2.11}$$

From this rough estimation, it can be determined that the factors affecting the flowrate due to the piezoelectric material include the magnitude of d_{31}, the thickness t, and the radius R_p.

2.2.1. Piezoelectric material

Piezoelectric material possesses a non-centrosymmetric crystal structure. These materials have a piezoelectric effect: under mechanical stress, the displacement in charge centers changes, thereby generating an electric field. This material property can also be the reversed (inverse piezoelectric effect), meaning that when a voltage is applied, the material deforms. Figure 2.11 takes the Aluminium Nitride (AlN) as an example to illustrate the piezoelectric effect. This effect is modeled by 2.6.

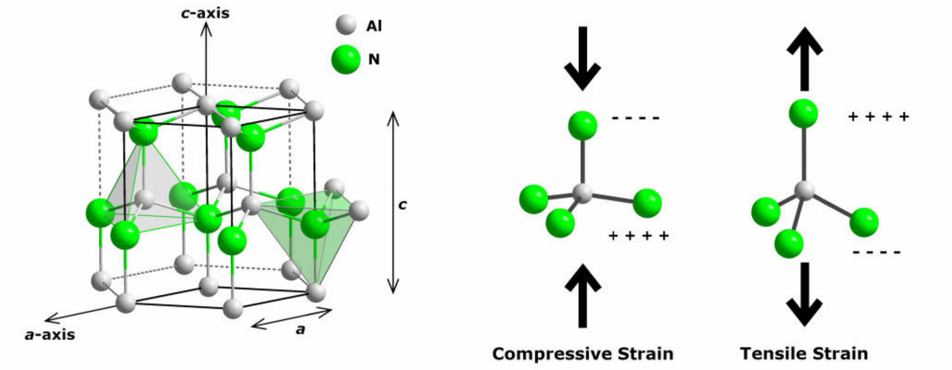

Figure 2.11: Piezoelectric effect of AlN [14]

Table 2.1 summarizes the widely used piezoelectric materials in MEMS devices with their characteristics and fabrication techniques.

Material	Abbreviation	d_{31} ($\frac{pm}{V}$)	d_{33} ($\frac{pm}{V}$)	CMOS compatibility	Bio compatibility	Deposition	Reference
Aluminum Nitride	AlN	1.28	3.15	yes	yes	Magnetron sputtering	[14]
Lead Zirconate Titanate	PZT	60	180	no	no	Pulsed laser deposition	[14]
Zinc Oxide	ZnO	3.32	5.9	no	yes	Chemical vapor deposition, sol-gel, Magnetron sputtering	[14]
Lithium Niobate	$LiNbO_3$	4.94	25.31	yes	yes	Film transfer	[14]
Polyvinylidene Fluoride	PVDF	32	28	NA	yes	Solution casting, electrospinning, hot press	[15]

Table 2.1: Overview of piezoelectric material characteristics and fabrication techniques

Among them, Lead Zirconate Titanate (PZT) as a piezoelectric ceramic material has significantly high piezoelectric coefficients, which surpass those of other materials by a factor of nine. The general chemical formula of it is $PbZr_xTi_{1-x}O_3$ indicates that PZT is a composite material prepared from the ferroelectric $PbTiO_3$ and the antiferroelectric $PbZrO_3$. Most existing piezoelectric micropumps use PZT as the piezoelectric material. Table 2.2 lists some examples of existing piezoelectric micropumps and verifies this.

Piezoelectric material	**Structure material**	**Backpressure (kPa)**	**Max flowrate (mL/min)**	**Media**	**Reference**
PZT	silicon	2	0.122	water	[16]
PZT	silicon	4	0.7	NA	[17]
PZT	PMMA	15.25	16.4	water	[18]
PZT	PMMA	40.5	318	water	[19]
PZT	PLA	NA	271	water	[20]
PZT	Silicon and photosensitive resin	50	0.09	De-ionized (DI) water	[21]

Table 2.2: Examples of piezoelectric micropumps

Meanwhile, the CMOS compatibility and bio-compatibility of the material need to be considered during fabrication along with the deposition methods. The fabrication of PZT thin film is a problem since lead is a toxic material and causes contamination in the fabrication equipment. This property is also reflected in its lack of compatibility with both CMOS and biology. Pulsed Laser Deposition (PLD) is the main technique used to deposit PZT thin films. The ability of PLD to transfer materials stoichiometrically from a multi-component target to the developing film sets it apart from other deposition techniques. This property is especially important for complicated oxides such as PZT because the precise proportional composition of PZT's chemical constituents has a significant impact on its qualities [22]. The sol-gel method is another technique for fabricating PZT, which uses propyl alcohol as a solvent and lead acetate, zirconium n-propoxide, and titanium isopropoxide as precursors [23]. The resulting solution contains $PbZr_{0.53}Ti_{0.47}O_3$ compositions. Following extensive post-processing, this solution is heated to produce the solidified PZT gel powder. The sol-gel method offers the advantage of easily controlling the microstructure growth and the material composition. However, its shortcomings include the need for high-temperature processing and associated costs [24].

The deposited thin film can be patterned through dry and wet etching. The dry etching methods include ion beam etching (IBE) and reactive ion etching (RIE), offering a high detail retention in the patterned shapes. However, dry etching has a significant shortcoming: it affects the electrical performance of PZT thin films [25]. Specifically, the ion bombardment in IBE processing induces local stress. and RIE processing is unable to achieve good surface roughness on the sidewalls. Therefore, dry etching is seldom used in the PZT thin film fabrication. In contrast, wet etching is more widely used due to its higher etching rates and lower costs. Wet etching uses HCl and HF solutions to etch PZT thin film in one step. However, HF has different reaction rates with the Ti and Zr in PZT and limits the etching accuracy. Performance loss in PZT patterning still presents a difficulty, notwithstanding Su et al.'s concept of a two-step wet etching procedure to counteract these effects [25].

Among the rest piezoelectric materials, polyvinylidene fluoride (PVDF) as a thermoplastic, shows great potential for MEMS applications due to its relatively high piezoelectric coefficients, environmental friendliness, acid resistance, lightweight and biocompatibility [26]. Additionally, the low Young's modulus of PVDF $(2.5 - 3.5GPa)$ enables it to deform in a large displacement as an actuator [27]. PVDF has five phases: α, β, γ, δ, and ε, only β phase exhibits piezoelectric properties [15]. Since PVDF initially exists in the α phase, it is essential to convert phase α to β through poling and stretching to enhance its piezoelectric capabilities. However, current fabrication methods for PVDF thin films, such as solution casting, electrospinning, and hot pressing, cannot achieve precise control for this phase transition.

Lithium niobate ($LiNbO_3$) is mainly used in surface acoustic wave (SAW) devices. $LiNbO_3$ need high deposition processing temperature of up to $1525°$C during the fabrication process [14]. Difficulty in precise control of orientation and texture during manufacturing limits the application of this material. In terms of Zinc oxide (ZnO), its low piezoelectric properties, combined with possible contamination in manufacturing lines and its reactivity with other materials, limits its usage in MEMS devices. Aluminium Nitride (AlN) has emerged as a new material choice for transducers owing to its low deposition temperature range of $20°$C to $400°$C, along with its good CMOS and biological compatibility [14]. Also, it avoids contamination during fabrication. However, an essential shortcoming of AlN is its lowest piezoelectric coefficients. To address it, doping scandium into the AlN to form the Scandium Aluminum Nitride (ScAlN) which doubles its d_{31} and d_{33} values compared with the AlN is a potential solution [28].

2.3. Flow rectifier type

For pumps lacking a flow direction component, fluid flows equally through both the inlet and outlet due to identical resistance in the channels. Therefore, a flow rectifier is a necessary component in the micropump for directing the flow. Flow rectifiers can be divided into two categories: one employs the opening and closing of a valve to control flow direction, and the other utilizes the difference in flow resistance between the forward and reverse directions. The former refers to valve-based pumps, while the latter is known as valve-less pumps.

2.3.1. Valve-based pump

The structure of a valve-based pump is complex, involving the different layers of the pump's external structure, valve, membrane, and piezoelectric actuator. Figure 2.12 takes an example of a bridge-valve-based micropump developed by Fan et al [29]. These seven layers assembled through the screw-nut connection to form the micropump is the figure 2.13.

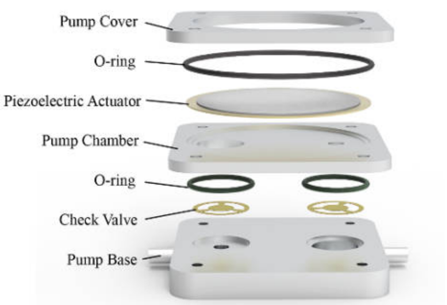

Figure 2.12: Exploded view of a valve-based micropump[29]

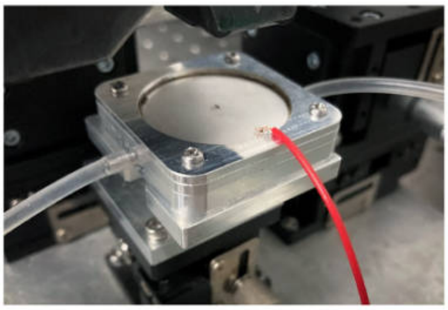

Figure 2.13: Assembled valve-based micropump [29]

Depending on the valve's state in its initial condition, valves can be categorized as normally open (NO) and normally closed (NC). The figure below illustrates the schematics of these two types of valves. In a NO valve, the channel is always open, allowing fluid to flow in its resting state. Only the movement of the membrane, as illustrated by the dashed line, will close the channel and stop the flow. Conversely, a NC valve keeps the channel closed in its resting state, and the movement of the membrane will open it. NC valves are more suitable for media delivery since the amount of media can be controlled more accurately since the media will not flow into the chip when the power is off [30].

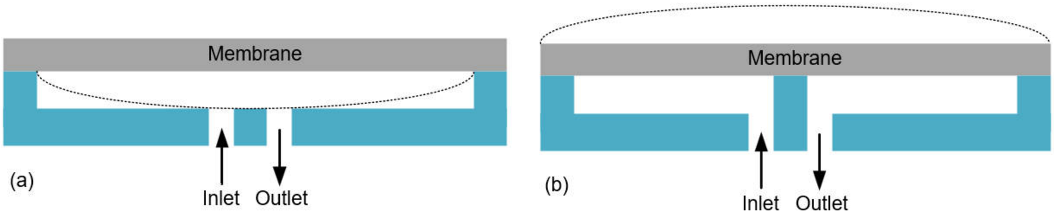

Figure 2.14: (a) Normally Open (b) Normally Closed valve

Valve-based micropumps can be categorized into passive and active valves based on their control methods. Active valves necessitate an external control system for operation, increasing the system's control complexity. In contrast, passive valves implement their open and close modes through structural design. Check valves are fabricated from materials with lower Young's modulus for easy open over their operation. Table 2.3 summarizes the common materials used in check valve fabrication. Polymers such as PLA and PET, significantly more flexible than silicon and metals by an order of magnitude, are widely used in check valve production [8]. PDMS/PMMA is also chosen as valve material for its biocompatibility and low stiffness. The PDMS check valve is fabricated using multilayer soft lithography, while the PMMA check valve is produced through laser micromachining. Rubber, known for its softness, is commonly used as an umbrella valve.

Material	Young's modulus (Gpa)	Material	Young's modulus (Gpa)
stainless steel	240	PLA	4.107
beryllium brozen	131	PET	2.8
glass	51	PMMA	2.9
silicon	10	PDMS	0.0021
		rubber	0.006

Table 2.3: Young's modulus of different materials

Depending on the structure of the valve, passive valves can be classified as cantilever valves, two-fixed ends valves, wheeled check valves, umbrella valves, ball valves, and other passive valves.

Cantilever valve

The cantilever valve is one of the simplest designs. As shown in figure 2.15, it consists of a structure with one fixed/anchored end and a free opposite end. In the suction mode, fluid comes from the top and opens the inlet valve. In the discharge mode, the fluid pushes the inlet valve upwards and closes the channel due to the existence of the upper block. The cantilever valve requires low open pressure but also results in the possibility of backflow and withstands low backpressure [31]. In addition, the cantilever valve has a shortcoming, that fluid forms a rotation motion around the open cantilever valve and induces the eddy flow at the end as shown in figure 2.16. The cantilever valve is always fixed through gluing or clamping to the substrate.

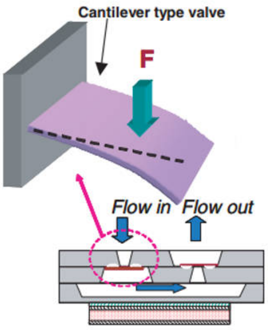

Figure 2.15: Structure of cantilever valve [17]

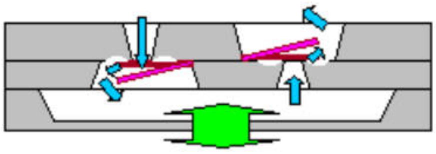

Figure 2.16: Illustration of the eddy flow around the cantilever valve [17]

Two fixed ends valve

Figure 2.17 illustrates the structure of two fixed ends valves along with their open and close modes. Two fixed valves using two valve seats sandwiched a rectangular thin plate valve in the middle. The opening of the two fixed-end valves is based on the deformation of the middle thin plate valve. The valve holes come in two shapes: rectangular and round. Valve holes are often circular since they have lower hydraulic losses than rectangular ones. [31]. The two fixed-end valves can work under high driving frequency and achieve good cut-off performance.

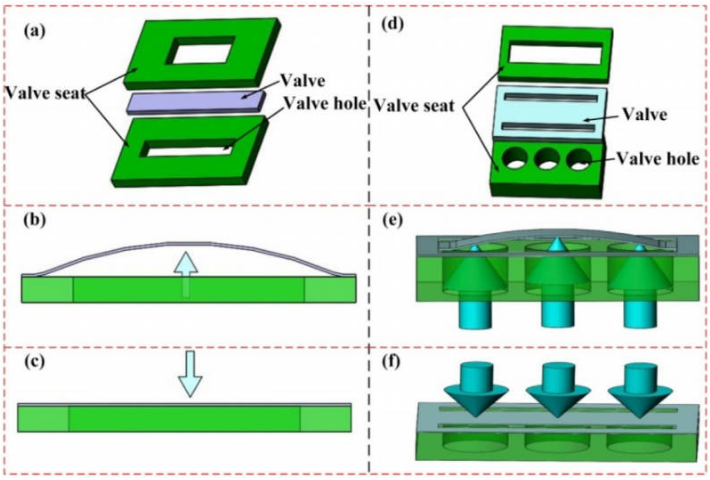

Figure 2.17: Structure of two fixed-end valves with (a) rectangular holes, along with their (b) open mode and (c) closed mode, is described. Additionally, (d) presents the structure of two fixed-end valves with circular holes, as well as their (e) open mode and (f) closed mode.[31]

Bridge (wheeled) check valve

The bridge valve, also known as a wheeled valve, consists of valve arms and a middle valve plate, as shown in Figure 2.18. When fluid flows from the top, the hydraulic pressure bends the four arms around the middle plate, allowing fluid to flow through the gap between the arms. In the reverse flow direction, the middle plate blocks the channel due to its larger dimension compared to the channel width. Some bridge valve designs feature arms as compliant orthoplanar springs to further ease the opening of the valve [32]. The bridge valve offers superior cut-off performance and flowrate compared to cantilever valves. Additionally, the fluid flow through the valves is distributed symmetrically, producing a uniform vertical force on the valves [17]. Its drawback lies in the complexity of fabrication.

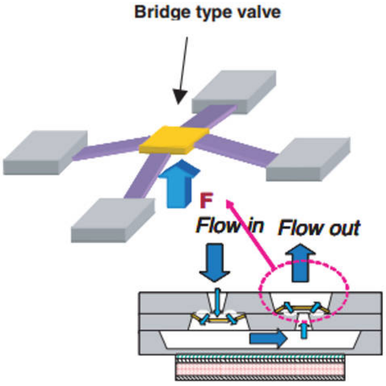

Figure 2.18: Structure of bridge valve [17]

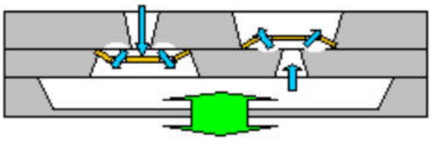

Figure 2.19: Illustration of the symmetric flow around the bridge valve [17]

Umbrella valve

Umbrella valve works through two principles. Figure 2.20 illustrates the first kind of umbrella valve, which moves limited by the clamping ring. The umbrella valve is installed to the fixing hole at the valve seat. The open mode is shown in figure 2.20 (b) as fluid moves the umbrella cover upwards and flows through the gap between the umbrella cover and valve seat. The reverse fluid flow pushes the umbrella cover in contact with the valve seat therefore closing the channel. Another type, showcased in figure 2.21, is crafted from soft rubber, chosen for its exceptional flexibility and low density, enabling rapid response of the umbrella valve [20]. Since rubber has tremendous flexibility and low density, the umbrella valve responds quickly. The clamping ring is embedded in the micropump substrate [29]. The hydraulic pressure caused by the fluid deforms the umbrella cover and controls the opening and closing of the channel through it. In the suction mode, the umbrella cover at the inlet moves upwards and opens the channel. In the discharge mode, the umbrella cover deforms downwards and touches the substrate therefore closing the inlet channel. The valve at the outlet works oppositely. An umbrella valve has better sealing capability and requires low static open pressure for the first kind of umbrella valve. However, the complex structure of umbrella valves makes it unlikely that they can be scaled down to micron sizes.

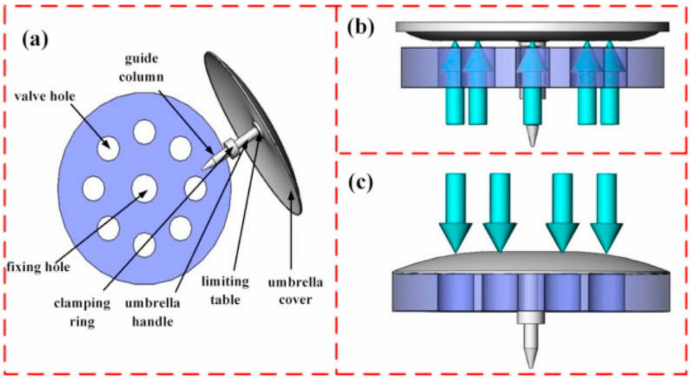

Figure 2.20: (a) Structure of umbrella valve with clamping ring at (b) open mode and (c) close mode [31].

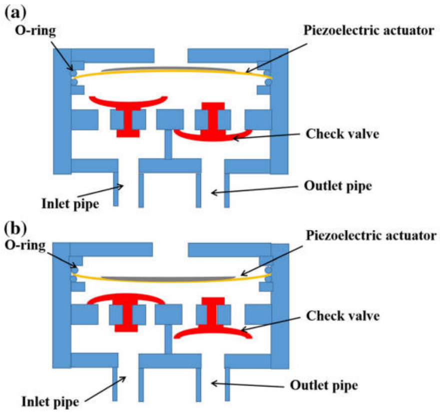

Figure 2.21: Structure of umbrella valve made of rubber at (a)suction mode (b) discharge mode of micropump [20]

Ball valve

The ball valve consists of a spherical particle and a conical valve channel. The open and close modes are controlled by the movement of the ball. As illustrated in Figure 2.26, fluid flow from the left pushes the ball towards the right [31]. Since the channel at the right end is designed to be larger than the diameter of the ball, it allows fluid to flow through the gap, thus opening the valve. In contrast, fluid flow from the left closes the valve. Ball valves are commonly used in traditional pumps due to their excellent mechanical robustness and low manufacturing costs. Given that the spherical structure can tightly fit into the round hole, ball valves can withstand high backpressure. Furthermore, the spherical structure has minimal resistance, allowing for a potentially high flowrate. However, the efficiency of ball valves decreases at high working frequencies.

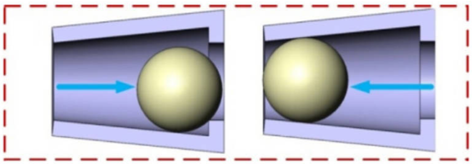

Figure 2.22: Structure of ball valve [31]

Other passive valves

Despite the above commonly used check valves, there are other structure valves illustrated in the 2.24 including ring mesa, V-shape, membrane, float, and elastomeric membrane check valves but relatively lack of use due to being worse performance and complex fabrication process.

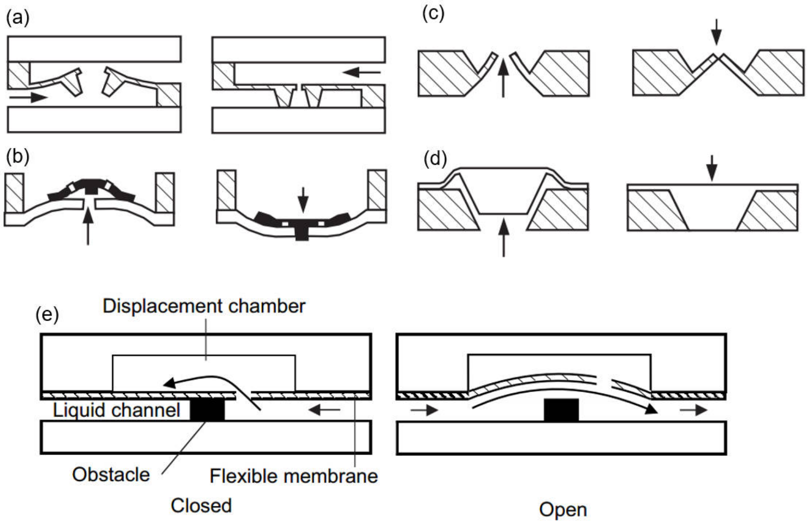

Figure 2.23: Passive check valves: (a) ring mesa, (b) membrane , (c) V-shape, (d) float and (e) elastomeric membrane. [8]

Summary of different passive check valves

Despite the research about micropump in the university, commercial companies such as Fraunhofer-Gesellschaft [33] and Bartels mikrotechnik [34] also created some high-performance valve-based micropump. Table 2.4 reported the state of art passive check valves in terms of the type of valve, valve material, backpressure, and flowrate over time.

First author	Year	Type of valve	Valve material	Backpressure (kPa)	flowrate (ml/min)	Reference
Carozza	1995	Ball	stainless steel	25	2.7	[35]
Nguyen	2004	Bridge	SU-8	2	1	[32]
Feng	2004	Bridge	silicon	4	0.7	[17]
Yamahata	2005	Ball	glass	28	5	[36]
Shen	2008	Ball	PMMA	35	6	[37]
Ma	2008	Cantilever	PDMS	6.404	2.35	[38]
Kan	2008	Cantilever	beryllium brozen	48.6	7.6	[39]
Park	2013	Cantilever	stainless steel	14	3.7	[40]
Cheng	2013	Bridge	stainless steel	32	1.82	[41]
Wang	2014	Two fixed ends	PDMS	22.5	118	[42]
Chen	2015	Two fixed ends	PDMS	85	1660	[43]
Ma	2015	Bridge	silicon	1.96	6.21	[44]
Zhang	2016	Umbrella	rubber	5.16	3.12	[45]
Zeng	2016	Umbrella	PMMA	40.5	318	[19]
Dong	2017	Bridge	beryllium brozen	4.08	1513.2	[46]
Dong	2017	Bridge	PET	0.89	2184.7	[47]
Hwang	2018	Bridge	NA	5171.25	205	[48]
Peng	2019	Umbrella	silica gel	32.47	1845	[49]
Woo	2020	Cantilever	PET	30.9	27.9	[50]
He	2020	Umbrella	rubber	NA	271	[20]
Dong	2020	Bridge	PET	0.82	2034.7	[51]
Pan	2021	Ball	polystyrene	23	99.6	[52]
He	2021	Bridge	PLA	27.41	226.4	[53]
Fan	2022	Bridge	PMDS and PI	33	162	[29]
Fraunhofer	NA	Bridge	silicon	NA	80	[33]
Bartels	NA	Cantilever	PPSU	70	10	[34]

Table 2.4: Comparison of different valve-based micropumps

Figure 2.24 summarized their performance. It can be found that bridge valves have a wide backpressure range, while other kinds of passive valves limit the backpressure to 100kPa. For the flowrate performance, two fixed ends, bridge, and umbrella valves present a relatively high flowrate up to thousands of flowrate. However, the main problem among these three valves is the complex fabrication process, especially during assembly. Ball and cantilever valves require low manufacturing costs due to their simple structure.

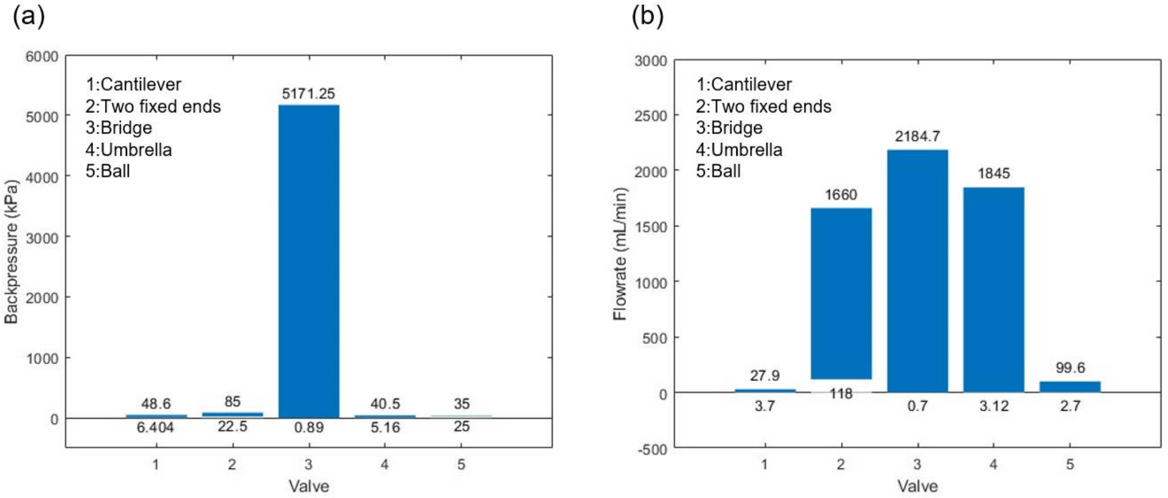

Figure 2.24: Performance of different types of passive check valve (a)Backpressure and (b) Flowrate

2.3.2. Valve-less pump

Unlike the valve-based pump, which uses a check valve to open and close the channel for directing purposes, the channel in the valve-less pump is always open, allowing fluid to flow through both the inlet and outlet during the working of the micropump. The direction of the fluid is determined by the difference in flow resistance between the forward and reverse directions in the channel, effectively performing the function of a valve [54]. The flow resistance coefficient reflects on the pressure loss coefficient and is defined as equation 2.12, where ξ is the pressure loss coefficient, Δp is the pressure difference at the inlet and outlet around the flow rectifier structure, ρ is the fluid density, v is the average flow velocity at the outlet [55].

$$\xi = \frac{\Delta p}{\rho v^2/2} \tag{2.12}$$

The impedance ratio ζ is defined as follows. Where ξ_- is the reverse flow resistance coefficient and ξ_+ is the forward flow resistance coefficient. For the pump to function effectively, ζ must be greater than one. A higher value of ζ is preferred to achieve maximum pump efficiency and a high flowrate [55].

$$\zeta = \frac{\xi_-}{\xi_+} \tag{2.13}$$

Valveless micropump can be mainly divided into two categories: external flow pipe type and built-in structure type [54]. The valveless micropump with external flow pipe achieves the one-way flow through the flow resistance difference in the special tubes such as diffuse/nozzle tubes, Y-shape tubes, and tesla valve tubes. In contrast, the built-in structure places the flow rectifier inside the pump chamber; examples include baffles of different shapes. The structure of the valve-less micropump is simpler compared to that of the valve-based micropump. Figure 2.25 presents an example of an external flow pipe type of valve-less micropump innovated by Lee et al. [56]. This micropump consists of two layers: the top layer serves as the membrane and has a PZT disc glued on top of it to act as the actuator. The bottom layer incorporates the chamber and flow rectifier structure. Here, an asymmetric obstacle acts as the flow rectifier to direct to flow.

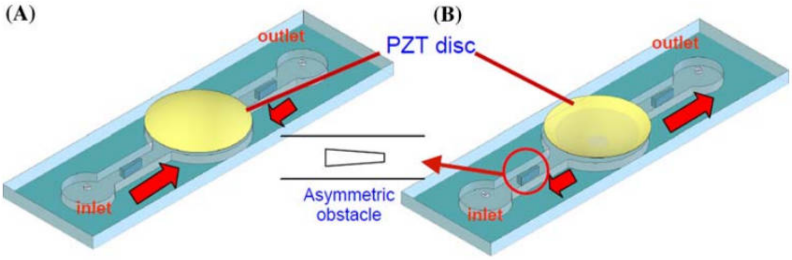

Figure 2.25: Example of valve-less micropump structure [56]

External flow pipe type

Stemme and Stemme [55] proposed the first concept of valveless piezoelectric micropump with two diffuser-nozzle channels to direct the flow in 1993. The structure of the diffuser and nozzle is illustrated in the figure below, where ϕ is volumetric flow, equaling the cross-section area of the narrowest parts of the channel times the fluid flow velocity.

$$\phi = Av \tag{2.14}$$

Since flow resistance in the diffuser direction is lower than the nozzle direction, fluid tends to come from the diffuser channel. This indicates that a bigger amount of fluid is transferred to the chamber through the inlet during the supply mode. The pump mode shows the opposite phenomenon. The channel design of the diffuser/nozzle element consists of two types: conical and flat-walled, both of which have almost the same diffuser capacity. The impedance ratio achieved as $1 < \zeta < 5$. This diffuser-nozzle micropump performs $16ml/min$ flowrate and $19.6kPa$ backpressure. The diffuser-nozzle structure is a commonly used flow rectifier in micropumps. Olsson et al. [57], Nguyen et al. [58], and Tseng et al. [59] have optimized its geometry and broadened its application.

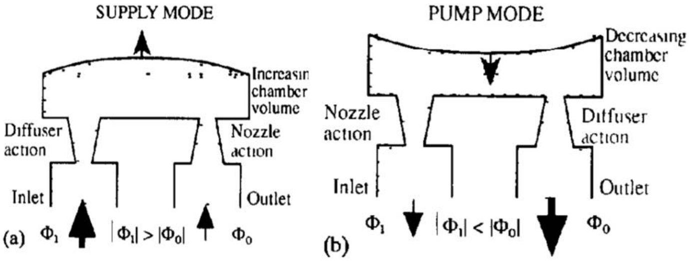

Figure 2.26: Structure of diffuser/nozzle based pump at (a) supply mode and (b) pump mode[55]

Based on the natural phenomenon that the fractal structure of a tree helps reduce flow resistance during the transportation of nutrients and moisture, Huang et al. propose the treelike Y-shaped tube as illustrated below [60]. When flowing through the Y-shape, the energy loss in the merged or divided flowing direction is different, therefore inducing one-way directing. This valveless micropump is measured at a maximum flowrate of $35.6ml/min$ and backpressure of $539Pa$ when applying $100V$ voltage to the actuator. Huang et al. continued their study about the Y-shape tube and reported that an increase in the number of branches decreases the performance of the micropump due to increased energy loss in the channel [60].

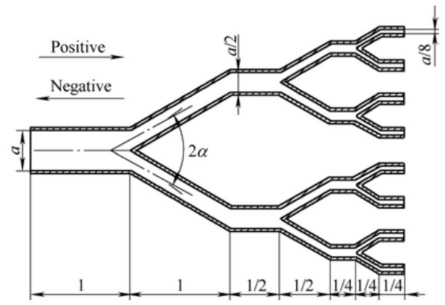

Figure 2.27: Treelike bifurcate Y-shape tubes [60]

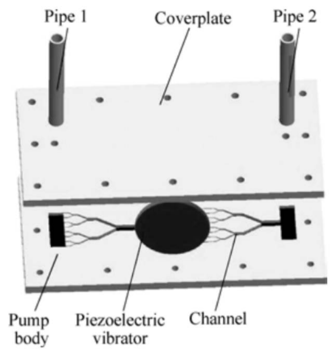

Figure 2.28: Valveless piezoelectric pump with Y-shape tubes [60]

The Tesla valve, depicted in figure 2.29, is a widely-used flow rectifier invented by Nikola Tesla in 1920. It utilizes inertial forces and viscous losses to facilitate unidirectional flow. The bottom structure in figure 2.29 illustrates the forward flow encounters minimal resistance, while the reverse flow in the upper structure will be divided into channels therefore blocking the flow of each other. Based on this principle, Yao et al used a tesla valve as a flow rectifier in the piezoelectric micropump and measured a maximum flowrate of $79.26ml/min$ [61]. However, the effectiveness of the Tesla valve's irreversibility is closely related to the flow state (laminar or turbulent), showing better one-way directionality at higher Reynolds numbers (Re) [62]. For $Re = 300 - 1500$, the impedance ratio of the Tesla valve is approximately 2.

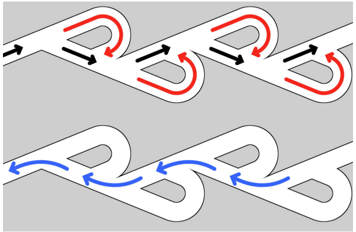

Figure 2.29: Schematic modified from Tesla's patent [62]

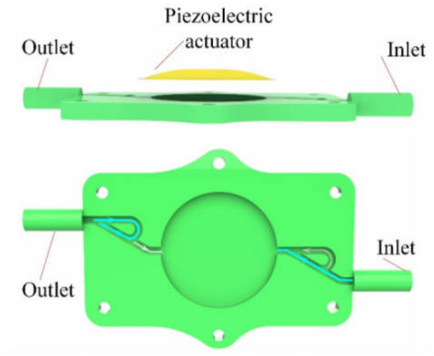

Figure 2.30: Valveless micropump with Tesla tubes [61]

Installing a baffle inside the channel to direct the flow is another option. The aerofoil-shaped structure is used as the direction-sensitive element to direct the fluid, innovated by Teng Yong Ng et al.[63] as shown in figure 2.31. This micropump comprises a hollow pump chamber in the center, with aerofoil-shaped structures at the inlet and outlet channels serving as flow rectifiers. (The individual numbers in the figure identify the structure of the parts on the micropump; for more detail, refer to the original patent document.) The working principle behind this design is that an aerofoil is a streamlined geometric shape, ellipsoidal at the front and sharp at the rear. When fluid approaches the front and flows along the shape in the laminar state, the flow resistance is small. In contrast, flow in the reverse direction significantly increases disturbance at the rear, along with the pressure gradient. Consequently, the boundary layer separates at the rear end, inducing eddy flow and thereby creating higher flow resistance. Based on this principle, positioning the round end of an aerofoil baffle at the inlet and the sharp end at the outlet causes the fluid to flow more smoothly during suction mode. Teng Yong Ng further enhanced the difference in flow resistance through the varying drag coefficients of the aerofoil at different angles of attack and by adding additional aerofoil-shaped structures.

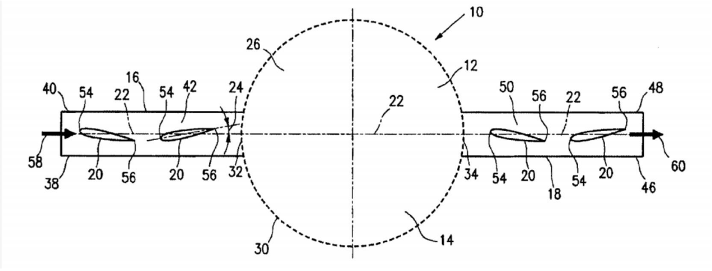

Figure 2.31: Valve-less micropump with aerofoil-shaped structure [63]

Wang et al [64] took advantage of the uneven flow resistance caused by airfoil baffles in both forward and backward directions as well, as illustrated in the figure 2.32. Wang et al. tested three geometric aerofoil structures (NACA 0015, NACA 63-412, and Clark Y) and found that the symmetric structure, NACA 0015, performs the best with the impedance ratio as 1.063. The measured maximum flowrate of the micropump with a NACA 0015 aerofoil baffle is $235.56ml/min$, and the maximum output backpressure is $842.8Pa$.

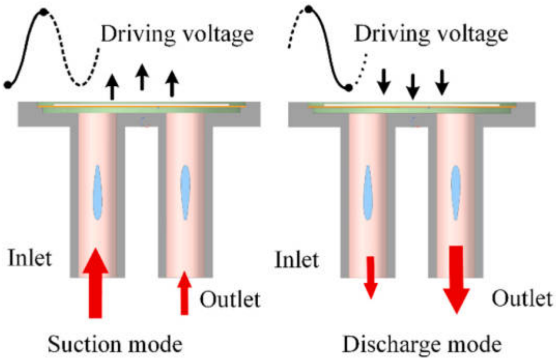

Figure 2.32: Working principle of micropump with aerofoil baffles [64]

Built-in structure type

In contrast, valveless miniature pumps with built-in structural types incorporate an asymmetric structure into the chamber. This structure directs flow through unequal resistance in forward and reverse directions by creating an imbalance. Researchers Ji et al. introduced hemisphere segments within the pump chamber as the implantable flow rectifier structure in 2014 [65]. The resistance to flow in non-streamlined shapes within the fluid arises mainly from frictional resistance and pressure drag. For instance, with a hemisphere, the drag coefficient (C_d) on the round surface is 0.42, but this coefficient increases to 1.17 at the vertical end face. Ji et al utilized half of the hemisphere as the flow-rectifying structure implanted in the micropump's chamber. The working principle of this design is illustrated in Figure 2.33, fluid tends to flow along the round surface. This micropump achieved a maximum flowrate of $30ml/min$ and a maximum backpressure of $256.76Pa$.

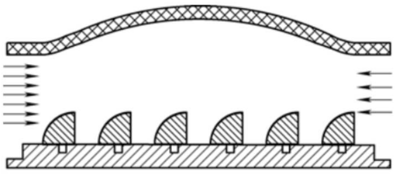

(a) Absorbing prcoess

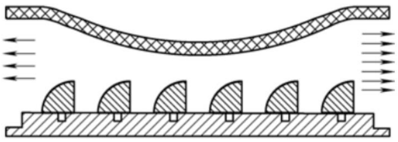

(b) Draining process

Figure 2.33: Working process of micropump with hemisphere structure at (a) absorbing process (suction mode) (b) Draining process (discharge mode) [65]

In 2019, Zhao et al. [66] proposed a crescent-shaped structure in the chamber to achieve a one-way flow direction, as illustrated in the figure 2.34 (e). The working principle behind this is that fluid flows smoothly around the external rounded angle of the crescent-shaped structure due to little energy loss. While flow from the opposite direction is easily induced the vortex inside the crescent shape due to the lower inner pressure. As a result, the fluid tends to flow from the left end to the right end either in suction mode or discharge mode. This research studies the relationship between the flowrate and the number of crescent-shaped structures. The maximum flowrate measured in this valveless micropump is $286mL/min$ at 220V and 82Hz AC voltage.

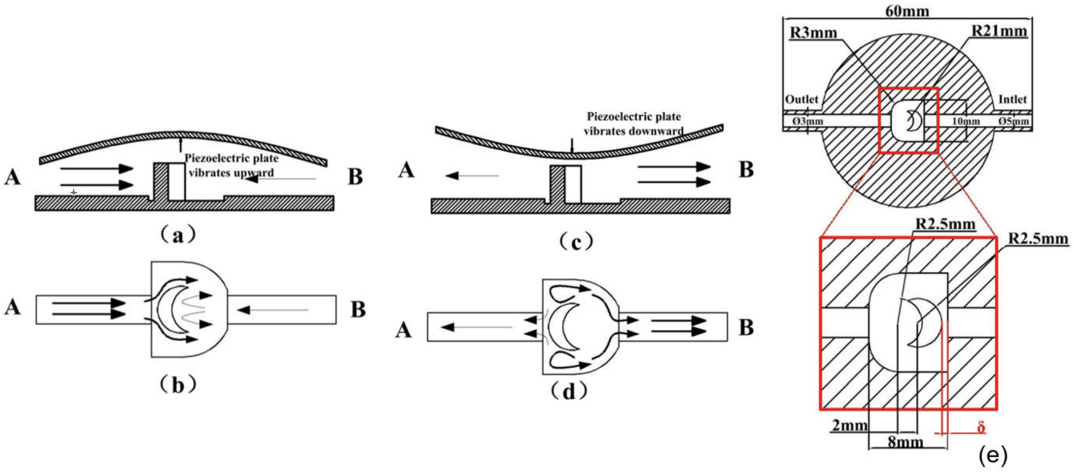

Figure 2.34: Illustration of working principle of piezoelectric micropump during (a) and (b) suction mode, (c) and (d) discharge mode. (e) presents the cross-section view of the pump body [66].

Summary of different types of valve-less micropump

Table 2.5 presents some examples of valve-less micropumps. It can be found that most valveless micropumps place the flow rectifier inside the external pipe. Compared with the valve-based micropump listed in the table 2.4, the valve-less micropump has a lower performance either in flowrate or in back-pressure. However, the fixed-flow rectifier structure simplifies the fabrication process and eliminates the need for a multi-layer structure in the valve-based micropump.

First author	Year	Pump type	Flow rectifier	Material	Backpressure (kPa)	flowrate (ml/min)	References
Stemme	1993	External pipe	Diffuser/nozzle	brass	19.6	16	[55]
Olsson	1997	External pipe	Diffuser/nozzle	silicon	74	2.3	[57]
Nguyen	2001	External pipe	Diffuser/nozzle	PCB	7	3	[58]
Tseng	2013	External pipe	Diffuser/nozzle	PMMA	2.9	0.4	[59]
Huang	2013	External pipe	Y-shape	NA	0.55	35.6	[60]
Ji	2014	Built in	Hemisphere segment structure	organic glass	0.257	30	[65]
Zhang	2019	Built in	Fluid guiding body	PLA	NA	167.8	[67]
Zhao	2019	Built in	Crescent-shaped structure	PLA	NA	286	[66]
Huang	2020	External pipe	Y-shape and diffuser/nozzle	NA	0.38	3.6	[68]
Yao	2021	External pipe	Tesla valve	polymer	NA	79.26	[61]
Wang	2023	External pipe	Airfoil baffles	photosensitive resin	0.842	235.56	[64]

Table 2.5: Comparison of different types valve-less micropump

Comparison of valve-based micropump and valve-less micropump

Valve-based micropump shows better performance in flowrate and backpressure as shown in figure 2.35. The flowrate higher than $150ml/min$ is mostly achieved by valve-based pumps. In addition, a valve-based pump manufactured by Lemke can withstand the highest backpressure as $50.5kPa$ [69]. The limitation of it is not able to work in a high-frequency region due to the phase lag of the valves and pump [11]. In addition, valve-based micropump suffers from fatigue and wear problems at the high working frequency [11]. In contrast, valve-less micropumps do not involve moving parts in fluid control; therefore, high working frequencies are possible, allowing media-containing particles to flow without the problem of clogging. While the difference in the forward and reverse flow direction for the flow rectifier structure is limited, the valve-less micropump cannot achieve a high flowrate. Also, the lack of a complete close condition for this kind of micropump causes relatively low backpressure. Typically, the working flowrate of valve-less micropump is lower than 250ml/min, and backpressure is less than 40kPa.

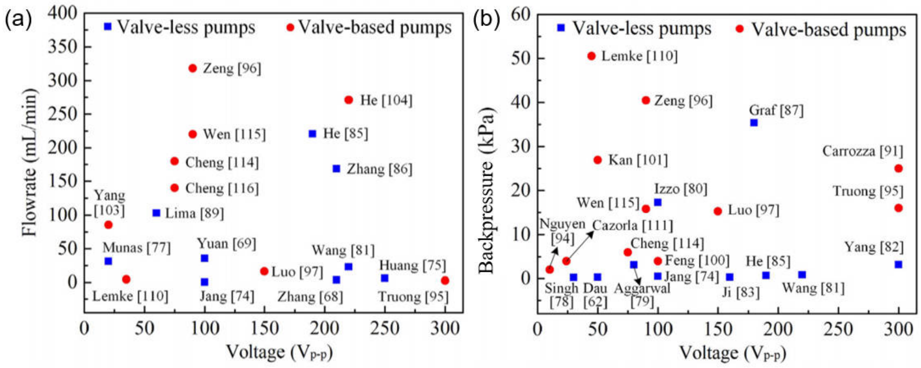

Figure 2.35: (a) Maximum flowrate and (b) maximum backpressure for valve-based micropump and valve-less micropump [11]

2.4. Manufacture methods

Manufacturing methods for piezoelectric micropumps have evolved along with the development of technology. Piezoelectric micropumps were originally manufactured using MEMS technology, as demonstrated by the micropumps made by Stemme and Stemme [55], Linnemann et al [13], Koch et al [16], Nguyen et al [32], Feng et al [17], and Kim et al [70]. These micropumps were produced by lithography of individual silicon wafers and then bonding them together. The lithography etch can achieve resolutions at the nano-level. Figure 2.36 illustrates the fabrication process of the bridge valves micropump as an example. The fabrication steps for micropumps are tedious and have limitations on the materials and geometry. Therefore, with the advancement of technology, later micropumps tend to combine micro-machining and 3D printing for fabrication.

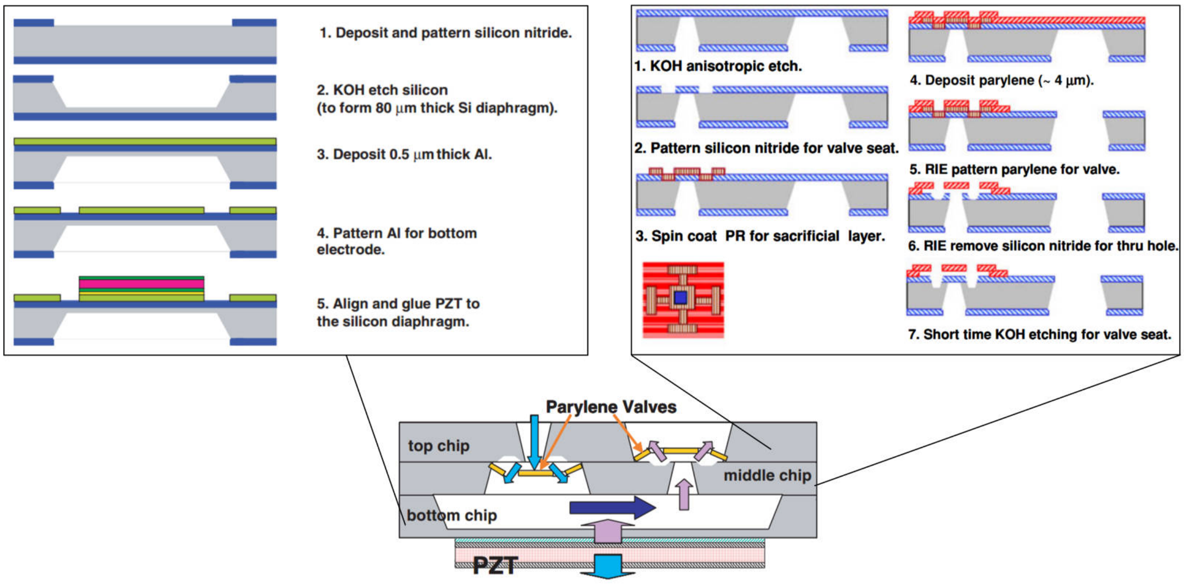

Figure 2.36: Etch and deposition fabrication steps for the piezoelectric micropump [17]

Figure 2.37 presents some examples of micropumps fabricated using micro-machining techniques. Kan et al. [71] fabricated a piezoelectric micropump with a cantilever valve in 2005, as shown in Figure 2.37(a). The pump body and upper cover are made of PMMA and were shaped by a precision-carving machine. The cantilever valve was made of a beryllium bronze membrane, 0.05mm in thickness, and was also fabricated using a precision-carving machine. The finished layers and PZT disk were stacked and glued together. Ma et al. [72] fabricated a micropump with bridge valves in 2015, as shown in Figure 2.37(b). This micropump was also made of PMMA, fabricated by milling each layer with a CNC milling machine. Two check valves were made of 0.09 mm silicon film and were cut by a laser cutting machine. Additionally, Ma et al. [44]created another type of micropump structure in the same year, as shown in Figure 2.37(c). This micropump uses PDMS as the pump material. Initially, the liquid PDMS was solidified in the mold through thermal curing. After that, a 3-axis CNC milling machine was used to cut the material into the desired geometry. Micro-machining expands the range of materials available, allowing bio-compatible materials PMMA and PDMS to be used as the material of choice for pump production.

As additive manufacturing technology matures, 3D printing is gradually becoming the third choice for micropump manufacturing due to its advantages in geometry-free and rapid fabrication. Wits et al. [73] manufactured a micropump using Selective Laser Melting (SLM), as shown in figure 2.37 (d). He et al. [20], manufactured two micropumps using a Fused Deposition Modeling (FDM) 3D printer in 2020 and 2021, as shown in figure 2.37 (e) and (f), respectively. Additionally, most valveless micropumps are 3D printed to achieve their complex geometries. However, 3D printing applications in micropump manufacturing have some shortcomings at the scale of hundreds of micrometers. Due to resolution limitations, 3D-printed micropumps are relatively larger than those fabricated with MEMS technology or micromachining.

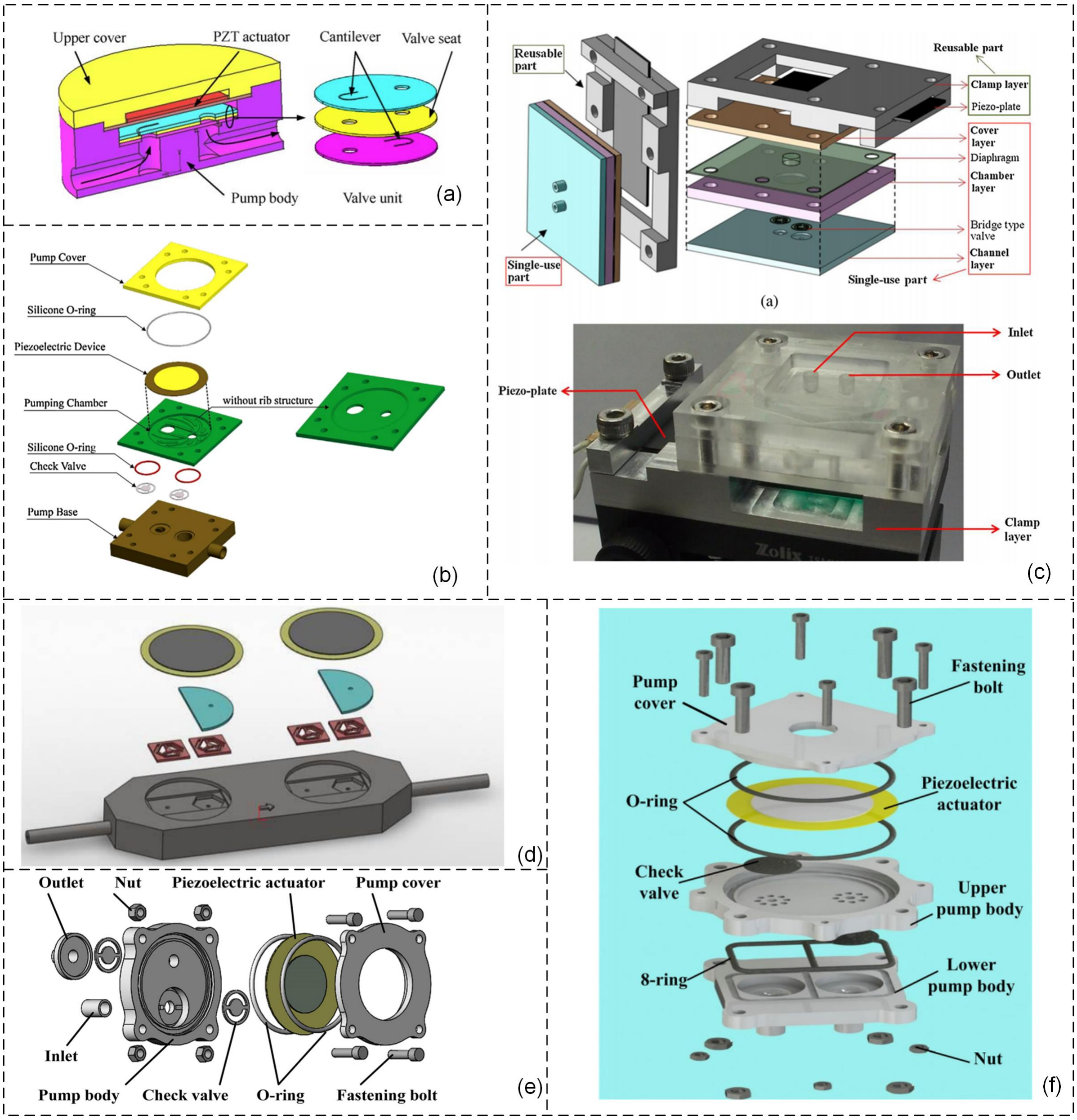

Figure 2.37: Piezoelectric micropump: (a) piezoelectric cantilever-valve micropump by Kan et al [71], (b) a piezoelectric-driven miniature pump with rib structure pumping chamber by Ma et al [72] and (c) a piezoelectric micropump with novel separable design by Ma et al [44] (d) Metal additive manufacturing micro-pump by [73], (e) micropump with straight arm bridge check valve and [53] (f) micropump with umbrella check valve [20]

2.4.1. 3D printing

3D printing belongs to a set of additive manufacturing techniques, that involve converting digital computer models into a solid 3D prototype through layer-by-layer forming [74]. The widely used additive manufacturing methods relevant to microfluidic device fabrication include Stereolithography (SLA), Fused Deposition Modeling (FDM), Multi-jet molding (MJM) and Selective Laser Sintering (SLM). Except for MJM, which uses metal powder, the other three 3D printers utilize polymers as raw materials. Among these, SLA achieves the highest resolution around $100\mu m$, while the resolution for MJM and FDM are $300\mu m$ and $350\mu m$ respectively [75]. SLA prints the model by selective polymerization of the liquid by laser or visible DLP light. Although SLA has very few topological restrictions in 3D geometry, it still requires support for some overhanging structures. The figure below shows an example of a part that needs a support structure to achieve its printability [76]. There are several slicer software options to help automatically build up the support including Cura, Lychee Slicer, Chitubox, PrusaSlicer, etc. The build orientation also influences the geometry of the required support. Removing the support requires manual work such as cutting, grinding, or milling. Additionally, the support-adding method can affect the surface roughness after post-processing.

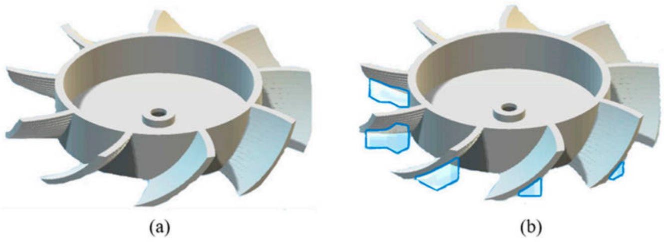

Figure 2.38: (a)Object (b)The support needed (blue part) to ensure the printability of object [76]

2.5. Research Approach

2.5.1. Research Gap

Chapters 1 and 2 have summarized the state-of-the-art in micropumps. Through the literature review, two research gaps have been identified:

1) The fabrication methods used for ball check valves fabrication in the literature include stereolithography [35], powder blasting [36] [37], and micro-machining [52]. These fabrication processes for pumps are complex in process. 3D printing technology has the advantage of free geometries. While the feasibility of 3D-printed micropumps remains unexplored.

2) Ball valves have been verified to have a simple fabrication process and excellent backpressure resistance in electro-magnetic micropumps, but their application in piezoelectric micropumps has been minimally explored.

3) Current valve-based micropumps all generate flow rates in the ml/min range, which is not ideal for OoC applications. Micropumps with flow rates in the µl/min range are mainly achieved through micropumps with valveless rectification structures. However, valveless micropumps have issues with low backpressure and significant backflow.

2.6. Research Question

Based on these research gaps, the research question is proposed:

How to manufacture a piezoelectric micropump with ball valves using rapid prototyping 3D printing technology

This research question can be further divided into the following sub-questions:

1. How to achieve the flowrate between $1\mu l/min$ and $100\mu l/min$ for the OoC applications?
2. What is the flow rate performance of a piezoelectric micropump with ball valves in terms of frequency, voltage, and backpressure?

3

Paper: 3D-printed piezoelectric micropump with ball valves

3D-printed piezoelectric micropump with ball valves

Abstract: Micropumps are essential for providing controlled fluid dynamics in Organ-on-a-Chip (OoC) devices. Additive manufacturing builds up prototypes in several hours with a free-geometry advantage. Therefore, this master's thesis investigates the utilization of additive manufacturing to produce a micropump with a flow rate in the range of several $\mu l/min$ for OoC applications. A ball valve-based piezoelectric micropump was fabricated with a mSLA 3D printer. This micropump generates unidirectional flow through the reciprocating motion of the piezoelectric actuator and the movement of a ball within the conical channel. The virtual mass due to the inertia of the fluid inside the chamber shifts the resonance frequency of the piezoelectric actuator from the 1600 Hz to 43 Hz. The maximum flow rate of $26.5\mu l/min$ was generated when the applied sinusoidal voltage was 240 Vpp at 5Hz and the maximum back pressure of 36.5 mbar was obtained under this power supply. These results confirm that additive manufacturing provides a promising option for miniature pump manufacturing.

1 Introduction

Organ-on-a-chip (OoC) technology combines biology and microtechnology to mimic human physiology in vitro [1]. To achieve this replication, biological cells are cultured on the chip, and microfluidics are used to mimic the in-vessel environment. Traditional model organisms and cell cultures, as traditional biological tools, both have their limitations. Although in vivo imaging has made significant advances, direct studies in mammals such as mice and humans remain challenging. In 2D and 3D cell cultures, some in vivo relevance must be sacrificed to facilitate experiments. For example, these cell culture methods are typically performed in static environments without fluid shear forces or compressive mechanical stress. As a novel biological system modeling tool, OoC compensates for the limitations of these two approaches by providing a higher level of in vivo relevance and allowing direct observation of cell and tissue behavior.

The required peripheral systems for OoC devices include flow controllers, micropumps, microfluidic multiplexers, and reservoirs [2]. Among these, the micropump functions as the beating heart [3]. The first miniaturized pump was developed by Thomas and Bessman in 1975 [4]. Subsequently, Spencer and Lintel et al. proposed micropumps with active and passive valves in 1978 and 1988, respectively [5] [6]. Research on micropumps increased significantly and has continued to grow in the decades since. Based on the external power source, micropumps can be categorized as non-mechanical or mechanical [7]. Non-mechanical micropumps have the advantage of generating low flow rates, typically ranging from 10 to 100 $\mu l/min$, which suits most OoC device requirements (e.g., brain-on-a-chip and liver-on-a-chip) [7]. However, the performance of non-mechanical pumps is easily affected by external pressure. In contrast, mechanical micropumps with valves can withstand high backpressure, but the flow rates they generate are commonly higher than 10 ml/min.

Based on the different actuation principles, mechanical micropumps can be further classified into shape memory alloy (SMA) actuation, electrostatic actuation, electromagnetic actuation, thermal actuation, and piezoelectric actuation [3]. Each of these actuation methods has its limitations. SMA and thermal actuation methods struggle with high-frequency operation and low cooling efficiency. Electrostatic actuators have limited membrane deflection, restricting the potential for high flow rate generation [8]. Electromagnetic actuators require additional cooling structures to dissipate heat and have electromagnetic interference. Although piezoelectric actuators require high voltage, they are still preferred for their low power consumption, quick response, and precise control. Piezoelectric micropumps have a proven track record of excellent performance, producing a wide range of flow rates and withstanding high back pressures [3].

Aside from the actuator, the valve is another significant component of the micropump, as it generates unidirectional flow. Compared to active valves, which require an additional control unit to open and close, passive valves save power and simplify the pump structure. The ball valve, which utilizes the movement of a ball to change flow resistance in a conical channel, is an excellent choice for directing flow. The ball valve demonstrated excellent performance in Yamahata's electromagnetic micropump prototype [9]. However, the exploration of ball valves in piezoelectric micropumps is rare. The first piezoelectric micropump with ball valves was created by Carozza et al. in 1994, and the second reported type was made by Pan et al. in 2021 [10] [11].

While these developed micropumps with ball valves all generate flow rates in the ml/min range, they fall far short of meeting the flow rate requirements of $\mu l/min$ for organs-on-a-chip devices. In addition, Carozza et al. used stereolithography, and Pan employed micromachining techniques, both of which involve tedious processes and high fabrication costs [10] [11]. The advent of 3D printing has introduced a novel technology capable of rapidly fabricating prototypes with free geometry ability, offering a promising option for the fabrication of micropumps.

Aiming to explore the feasibility of additive manufacturing technology in micropump fabrication for organ-on-a-chip applications, this work designed, fabricated and characterized a micropump with a footprint of $40 \times 40 \times 16mm$. Analysis and simulation were carried out during the design phase. The micropump chamber, conical channel and pump cover were 3D printed and assembled with the commercial piezoelectric actuator and polypropylene sphere to form this micropump prototype. A directional fluid flow is achieved through the reciprocating vertical deformation of the PZT film and the movement of the ball in the conical channel. To demonstrate the generated flow rate range, the micropump was tested at varying frequencies, voltages and backpressures. The measured performance results are in the table 1.

Table 1: Measured specifications of micropump

Specification	Measured value
Maximum flow rate	26.5 $\mu l/min$
Maximum backpressure	36.5 mbar
Resonance frequency	5 Hz
Maximum operating voltage	240 Vpp
Fluidic diodicity	6.93
Dimension	$40 \times 40 \times 16mm$

2 Working principle and design

The components of a micropump are illustrated in Figure 1 (a). The piezoelectric actuator comprises a commercial lead zirconate titanate (PZT) film and a brass membrane. The ball valve is composed of two polypropylene balls and conical channels. The diameter of the ball is larger than the narrow end of the conical channel. A slotted hole at the wide end of the conical channel prevents the ball from moving into the chamber. The pump body was made by a Masked Stereolithography Apparatus (mSLA) 3D printer. Three O-rings were utilized at the chamber and valve parts to ensure sealing. Figure 1 (b) shows the assembled micropump, with a small footprint of $40 \times 40 \times 16$ mm. The detailed parameters of each component are listed in Table 2.

Table 2: Parameters of the micropump prototype

Parameter	Value (mm)
Piezoelectric film diameter	25
Piezoelectric film thickness	0.26
Brass membrane diameter	35
Brass membrane thickness	0.25
Chamber diameter	28
Chamber depth	0.3
Cylinder channel diameter	1.5
Conical channel narrow end diameter	1.5
Conical channel wide end diameter	3
Conical channel depth	3.5
Channel length	18.2
Ball diameter	2.4

2.1 Micropump working principle

The prototype is a reciprocating type micropump. Applying a sinusoidal voltage to the PZT film induces periodic horizontal elongation and contraction due to the non-centrosymmetric crystal structure of the material. As the PZT film is bonded to the brass membrane, horizontal strain leads to vertical deformation due to the bending momentum. This cyclical vertical deformation drives the micropump, alternating between suction and discharge modes to pump fluid, as shown in Figure 1 (c). During the suction mode, the upward movement of the PZT film creates an upward deformation in the membrane, increasing the volume of the chamber and reducing internal pressure. This pressure differential between the chamber and external environments draws fluid into the micropump. In this mode, balls located within the conical channel move upward. In the inlet channel, the ball contacts the slotted hole while moving upward, allowing fluid to flow through the gap (Figure 1 (c) i). Meanwhile, in the outlet channel, the ball contacts the wall of the conical channel, terminating fluid flow (Figure 1 (c) ii). Discharge mode is the reverse phenomenon, where the fluid is expelled and the ball moves downward. In this situation, the inlet valve closes, and the outlet valve opens. Through this reciprocating motion within the micropump, fluid achieves unidirectional flow from the inlet to the outlet.

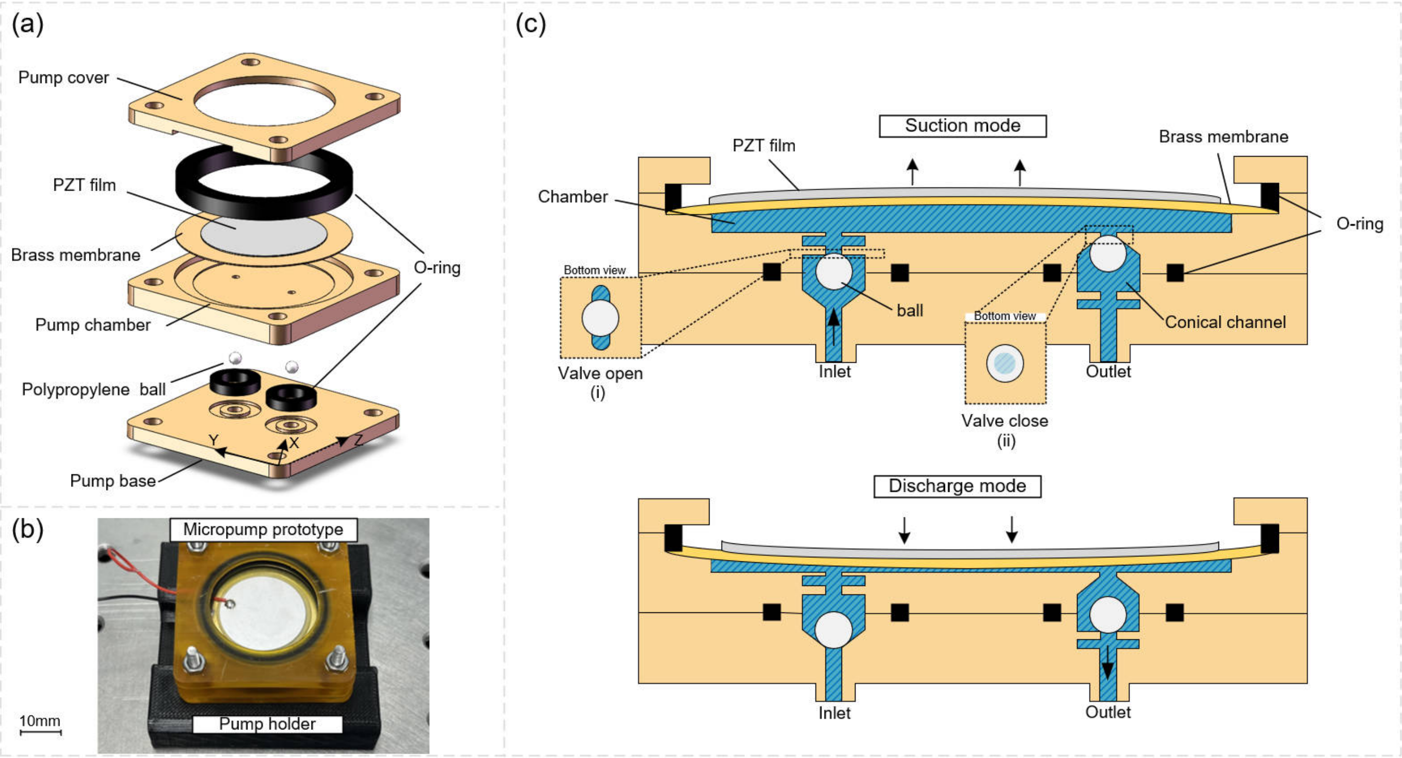

Figure 1: (a)Exploded view of the micropump structure, (b) Picture of the assembled 3D-printed micrompump, (c) The working principle of a micropump with ball valves

2.2 Design criteria

2.2.1 Deformation analysis of piezoelectric actuators

This prototype utilizes the d_{31} mode of the piezoelectric material for operation. The vertical electrical field induces a horizontal strain in the piezoelectric film. While the bottom surface of the piezoelectric film is bonded to the diaphragm, the horizontal deformation constraint causes a radial deformation by a bending moment. This phenomenon is explained in the Equation 1, where d_{31} is the piezoelectric coefficient and E_3 is the electric field [3].

$$\epsilon_1 = d_{31}E_3 \tag{1}$$

Using the piezoelectric working principle, as shown in Equation 1 and Timoshenko thin plate theory, Mo et al. investigated the deflection behavior of an unimorph circular piezoelectric actuator in an electric field [12]. When the piezoelectric layer and substrate have different diameters, the general solutions for the displacement $w(r)$ are given by:

$$w(r) = \begin{cases} \dfrac{C_5\left\{2R_1^2\ln\left(\frac{R_1}{R_2}\right)+\left[1-\left(\frac{R_1}{R_2}\right)^2\right]r^2\right\}V}{C_6-C_7\left(\frac{R_1}{R_2}\right)^2+\frac{1}{2}h_p^4S_m^2(1+\nu)\left(\frac{R_1}{R_2}\right)^4}, & r \le R_1 \\ \dfrac{C_5\left\{2R_1^2\ln(r)-R_1^2[2\ln(R_2)-1]-\left(\frac{R_1}{R_2}\right)^2r^2\right\}V}{C_6-C_7\left(\frac{R_1}{R_2}\right)^2+\frac{1}{2}h_p^4S_m^2(1+\nu)\left(\frac{R_1}{R_2}\right)^4}, & R_1 < r \le R_2 \end{cases} \tag{2}$$

where:

$C_5 = 3d_{31}h_mS_{11}^ES_m(h_m+h_p)$

$C_6 = 4S_{11}^Eh_ph_m^3S_m + 6S_{11}^Eh_m^2h_p^2S_p + 4S_{11}^Eh_mh_p^3S_m + \frac{1}{2}h_p^4S_m^2(1+\nu) + \frac{2h_m^4S_{11}^E}{1+\nu}$

$C_7 = 4S_{11}^Eh_ph_m^3S_m + 6S_{11}^Eh_m^2h_p^2S_m + 4S_{11}^Eh_mh_p^3S_m + h_p^4S_m^2(1+\nu)$

Where V is the applied voltage, r is the radial variable, E_{11} is Young's modulus of PZT film, S_{11}^E is the compliance constant of PZT film, defined as $1/E_{11}$, ν is the Poisson's ratio of PZT film, h_p is the thickness of PZT film, and r_1 is the radius of PZT film. Additionally, E_m is Young's modulus of the membrane, S_m is the compliance constant of the membrane, h_m is the thickness of the membrane, and r_2 is the radius.

The pump will be operated at low frequencies, so the deformation field will be proportional to the first vibration mode, where the maximum deflection is achieved in the central point as shown in Equation 3.

$$w_{max} = w(r=0) = \frac{2C_5 R_1^2 \ln\left(\frac{R_1}{R_2}\right) V}{C_6 - C_7\left(\frac{R_1}{R_2}\right)^2 + \frac{1}{2}h_p^4 S_m^2 (1+\nu)\left(\frac{R_1}{R_2}\right)^4} \tag{3}$$

Since the vertical displacement has been calculated in Equation 2, and its corresponding bottom area is $rd\theta dr$, the stroke volume V_0 can be obtained by integrating the product of $w(r)$ and $rd\theta dr$. The result is shown below:

$$V_0 = \int_0^{R_p} \int_0^{2\pi} w(r) r d\theta dr \tag{4}$$

Stroke volume is the amount of fluid a pump displaces per cycle. Therefore, the theoretical volumetric flow rate Q_v equals the stroke volume multiplied by the number of strokes in a unit of time f, as shown in Equation 3.

$$Q_v = V_0 f \tag{5}$$

The actual flow rate Q is also affected by the check efficiency of the valve η:

$$Q = Q_v \eta \approx \pi \times f \times w \times r^2 \times \eta \tag{6}$$

The rough estimation of the flow rate pumped by the micropump has been obtained in Equation 6 [13]. It provides valuable insight into the factors influencing the micropump's performance. An increase in the applied voltage, radius of the piezoelectric film and frequency, valve efficiency, and a decrease in the film's thickness results in a higher flow rate.

COMSOL Multiphysics was used for simulation to obtain more accurate results in piezoelectric actuator deformation. A 3D model of the piezoelectric actuator is shown in Figure 2. The simulation used multiphysics of electrostatics, solid mechanics, and the piezoelectric effect to calculate the results. The O-ring and the bottom pump body were fixed. The piezoelectric actuator is applied with a sinusoidal electrical potential at the top and a ground at the bottom.

2.2.2 Analysis of hydraulic system

To have a deeper understanding of how pump components influence the resonance frequency of the device, the micropump is further simplified as a mass-spring oscillator system as shown in Figure 3 [9]. The ball valves are considered here as ideal fluidic rectifiers. When a voltage is applied, an external pressure P_s is exerted on the membrane, resulting in a downward acceleration $\frac{d^2x}{dt^2}$ on the membrane, as shown in the Equation 7.

$$(P_s - P_2)A - Kx = M\frac{d^2x}{dt^2} \tag{7}$$

Where P_2 is the pressure in the chamber, A is the chamber area, x is the vertical displacement of the diaphragm, K is the spring constant of the diaphragm and M is the virtual mass of the diaphragm and the piezoelectric actuator.

The Equation 8 shows that the fluid with mass m is moved by the pressure in the chamber P_2.

$$P_2 a = m\frac{d^2y}{dt^2} \tag{8}$$

Since the volume of fluid pumped by the membrane is equal to the fluid flowing out through the tubing, Equation 9 can be calculated.

$$Ax = ay \tag{9}$$

Equation 9 can be further calculated as:

$$\frac{d^2y}{dt^2} = \frac{A}{a}\frac{d^2x}{dt^2} \tag{10}$$

Integrating the Equation 10 into the Equation 7, this mass-spring system can be rewritten as

$$P_s A = \left[M + \left(\frac{A}{a}\right)^2 m\right]\frac{d^2x}{dt^2} + Kx \tag{11}$$

The resonant frequency of this second-order system is calculated by Equation 12.

$$f_0 = \frac{1}{2\pi}\sqrt{\frac{K}{M + \left(\frac{A}{a}\right)^2 m}} \tag{12}$$

2.3 Equivalent RLC system

In the above mass-spring oscillator system, the damping effect caused by membrane deflection is not considered. Its performance can be analyzed through the equivalent RLC (resistance, inductance, and capacitance) circuit. Figure 4 shows the equivalent RLC model derived from the hydraulic system of a micropump with two passive valves, where the inlet valve is closed and the outlet valve is open. Here, the ball valves act as ideal diodes. The flow rate Q corresponds to the current I in the circuit. Fluid resistance is analogous to electrical resistance. Since the function of inductance is to resist changes in current, and fluid inertia serves the same purpose by resisting changes in flow velocity. Additionally, the membrane stores and releases

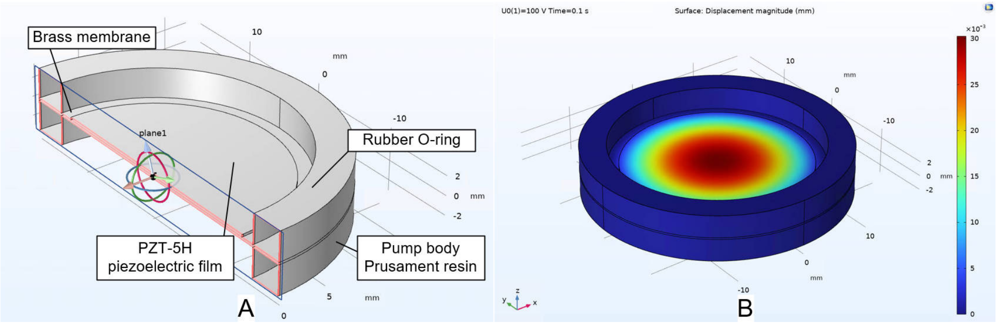

Figure 2: (A) The 3D model build of Piezoelectric actuator (B) Deflection result of the piezoelectric actuator in COMSOL Multiphysics 6.1.

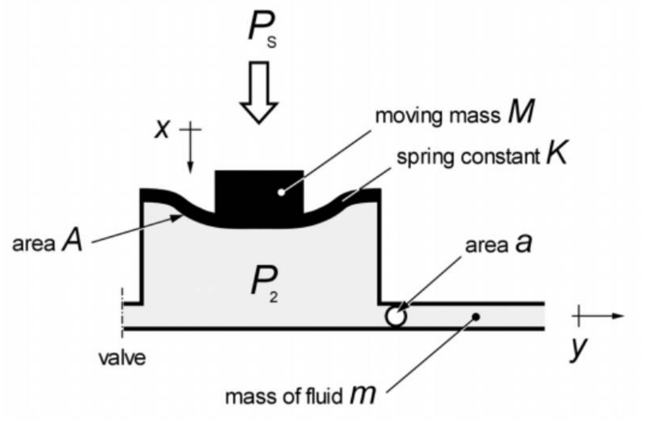

Figure 3: Schematic diagram of pump system in discharge mode [14]

mechanical energy when deformation, plays the same role as capacitance. The detailed calculation for each component is shown below.

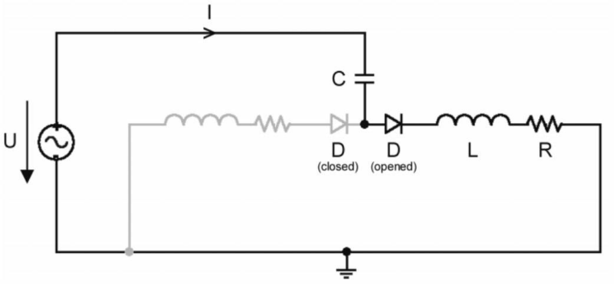

Figure 4: Equivalent RLC system of micropump with ball valves [14]

Fluid resistance is caused by the viscosity of the fluid, which results in a pressure drop as the fluid flows along the pipe. For incompressible Newtonian fluids, this pressure drop can be calculated using the Hagen-Poiseuille law, as shown in the Equation 13, where R is the fluid resistance, μ is the fluid viscosity, l is the channel length and r is the channel radius.

$$R = \frac{8\mu l}{\pi r^4} \tag{13}$$

The inertial effect of the accelerated fluid along the pipe contributes to the fluid inductance as shown in Equation 14, which is related to the fluid density ρ, the channel length l and the cross-sectional area S.

$$L = \frac{\rho l}{S} \tag{14}$$

Combining the equation 14 with the density function $\rho = \frac{m}{la}$, the inertia of the fluid can be rewritten as

$$L = \frac{m}{a^2} \tag{15}$$

The deflection of the membrane in a reciprocating pump is caused by the applied pressure and influences the volume change in the chamber. The value of this equivalent capacitance is related to the volume change ΔV and the pressure change ΔP as shown in Equation 16.

$$C = \frac{\Delta V}{\Delta P} \tag{16}$$

Since the volume change refers to the chamber area A and the deformation occurs in the membrane x as $\Delta V = Ax$ and this deformation x causes the pressure difference between P_s and P_2 as $(P_s - P_2)A = Kx$, the capacity can finally be calculated as:

$$C = \frac{A^2}{K} \tag{17}$$

The membrane is bonded to the PZT film, and they share the same displacement. Therefore, the springs can be regarded as connected in parallel and K is the sum of K_{brass} and K_{PZT-5H}.

Table 3 summarises the correspondence between the hydraulic micropump model and the electrical RLC model.

With known equivalent components, the voltage equation for the RLC system shown in Equation 18 can be con-

Table 3: Converting hydraulic micropump model to electrical RLC model

Fluidic parameter	**Electrical equivalence**
Pressure P	Voltage U
Flow rate Q	Current I
Fluidic resistance $R = \frac{8\mu l}{\pi r^4}$	Resistance R
Fluid inertia $L = \frac{\rho l}{S} = \frac{m}{a^2}$	Inductance L
$C = \frac{\Delta V}{\Delta P} = \frac{A^2}{K}$	Capacitance C
Valve	Diode D

verted to the equivalent hydraulic system of the micropump as shown in Equation

$$U(t) = \frac{1}{C}\int_0^t I(t)\,dt + L\frac{d}{dt}I(t) + RI(t) \tag{18}$$

$$P_S(t) = \frac{K}{A^2}\int_0^t Q(t)\,dt + \frac{m}{a^2}\frac{d}{dt}Q(t) + RQ(t) \tag{19}$$

The resonant frequency of this system can be calculated from the Equation 20. In the RLC equivalent circuit analysis, the mass of the membrane M is not taken into account. The remainder is the same as the resonant frequency obtained from the spring-mass system analysis (Equation 12).

$$f_0 = \frac{1}{2\pi}\sqrt{\frac{1}{LC}} = \frac{1}{2\pi}\sqrt{\frac{K}{\left(\frac{A}{a}\right)^2 m}} \tag{20}$$

Given a sinusoidal actuation $P_s(t) = P_s sin\omega t$, the average flow rate Q can be calculated as a ratio of the average flow rate Q_0 at the angular frequency ω:

$$\frac{Q}{Q_0} = 2\xi\sqrt{\frac{\left(\frac{\omega}{\omega_0}\right)^2}{\left(1-\left(\frac{\omega}{\omega_0}\right)^2\right)^2 + \left(2\xi\frac{\omega}{\omega_0}\right)^2}} \tag{21}$$

Where the damping ratio is $\xi = \frac{R}{2}\sqrt{\frac{C}{L}}$, the angular frequency is $\omega = \frac{1}{\sqrt{LC}}$.

3 Micropump fabrication

The pump cover, chamber, and base (as shown in Figure 1 (a)) were printed using the mSLA 3D printer (Prusa SL1S SPEED 3D printer) with photosensitive resin (Prusament Resin Tough Transparent Amber). This printer has an XY-axis resolution of 50μm and a minimum Z-axis resolution of 25μm. The prototype was first designed in SolidWorks, and then its STL file was sliced with PrusaSlicer to generate the G-code for printing. As the surface close to the platform needs to be supported, resulting in a lower surface quality, and the upper and lower surfaces of the pump cover, chamber and base need to be bonded to other parts, a higher surface quality is required for this contact surface. Therefore, the printing orientation for these three components is from side to side (in Z direction), not from top to bottom. The total time for printing the prototype was approximately two hours. After printing was completed, the prototypes were immersed in a Formlabs Form Wash filled with isopropyl alcohol (IPA) to remove the uncured resin. Afterward, the surface of the pump chamber and base were blown dry using compressed air. Finally, the three parts were cured under UV light at room temperature for fifteen minutes to enhance stiffness. Due to the layer-by-layer process of 3D printing, the stiffness of the printed prototype varies along the XY and Z directions (Figure 1 a). As a result, cured printed parts have a Young's modulus in the X or Y direction of 1.6GPa and a Z-direction Young's modulus of 1.2GPa.

Subsequently, the piezoelectric actuator (Huixin Electronic Piezo Ceramic Wafer Plate) was placed on the pump chamber, and an epoxy adhesive (Loctite HYSOL 3421) was injected at the contact edge between the piezoelectric actuator and the chamber's upper surface to enhance the sealing efficacy. Subsequently, an O-ring (Outer diameter: 35 mm, inner diameter: 28 mm) and the pump cover were placed on top of the piezoelectric actuator. In the valve assembly, two polypropylene balls were inserted into the conical channels and two O-rings (Outer diameter: 10 mm, inner diameter: 6 mm) were placed around them. Finally, four M3 screws and nuts were used to clamp the three layers together.

4 Experiment set up

Figure 5 presents the experimental setup for the micropump performance characterization. A power supply (DELTA ELEKTRONIKA HOLLAND) provides a 24V operating voltage to the amplifier (BD300 Dual-Channel 300V Amplifier) and the signal generator (RS PRO Arbitrary Waveform Generator) controls the magnitude and shape of the output voltage, producing a sinusoidal voltage to drive the piezoelectric actuator. This 100x amplifier requires an input threshold voltage over 0 V. Therefore, the minimum voltage of the sinusoidal voltage input to the amplifier for the flow rate testing in the experiment is 0.1V and outputs

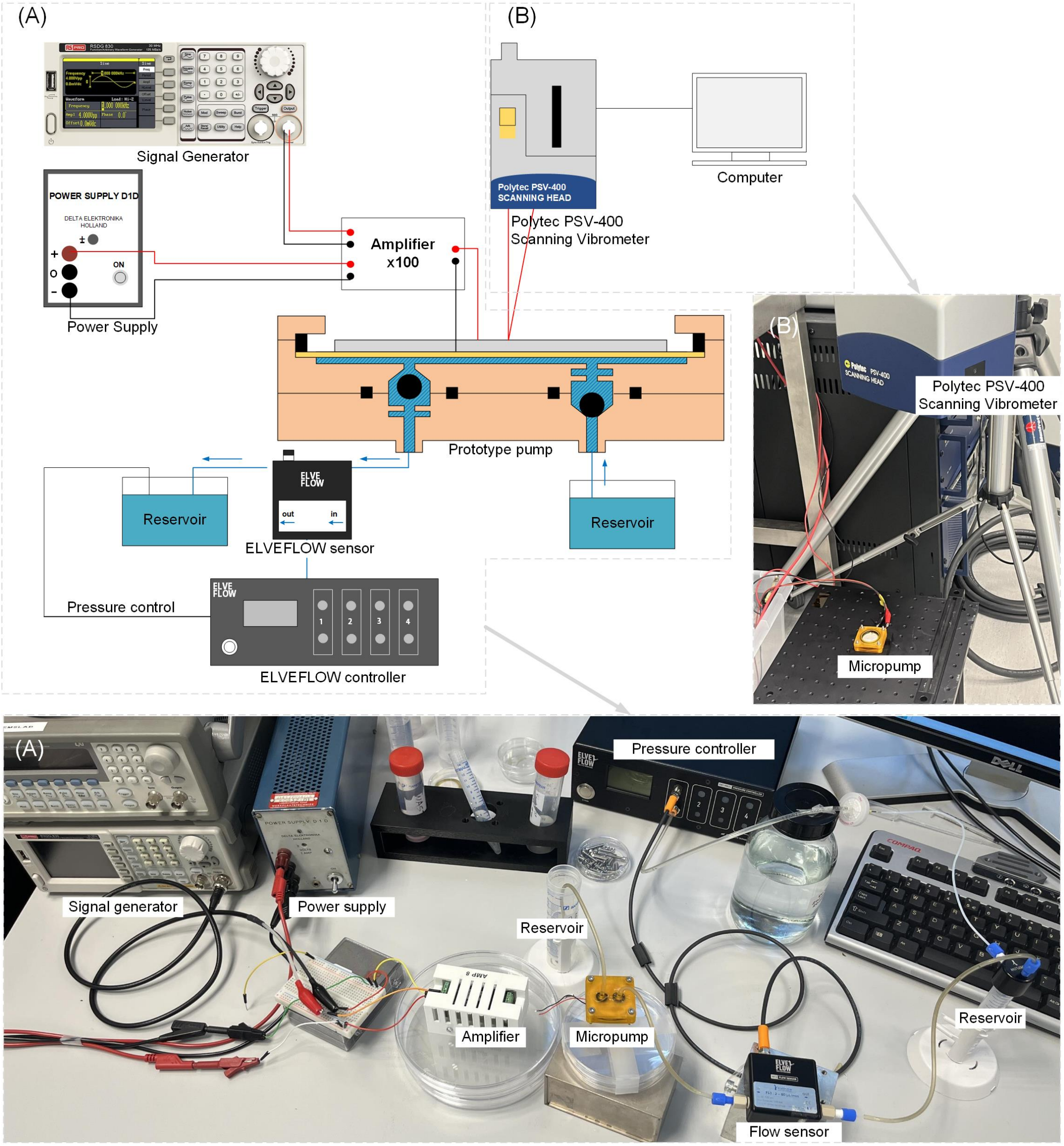

Figure 5: Schematic diagram and actual experiment setup for micropump performance characterization: (A) flow rate measurement (B) PZT film displacement measurement

10V to the micropump. The maximum voltage applied in the experiment is 240 Vpp, as the piezoelectric actuators are susceptible to damage if voltages above this value are applied. The fluid used in this project is 99.9% IPA (isopropyl alcohol). As IPA has a similar density (786 kg/m^3) to the polypropylene sphere (895 kg/m^3), the effect of the orientation on the micropump performance can be ignored.

Figure 5 (A) shows the schematic diagram and experimental setup for flow rate measurement. The inlet of the micropump is connected to a reservoir and the outlet is connected to the inlet of a flow sensor (ELVEFLOW Microfluidic Flow Sensor MFS), which can measure flow rates in the range between $2\mu L/min$ to $80\mu L/min$ in both direction. The outlet of the flow sensor is connected to another reservoir. This reservoir is connected to an integrated air pressure controller of the ELVEFLOW Microfluidic Flow Controller aims to adjust pressure at the outlet of the micropump. During the experiment, an IPA-DIW (deionized water) mixture is used as the working fluid.

Figure 5 (B) presents a schematic diagram of the displacement measurement of the PZT film as well as the experimental setup. The Polytec PSV-400 Scanning Vibrometer is used to detect the velocity change of the laser point on the PZT film. This vibrometer operates based on the laser Doppler effect, where the frequency of the emitted or reflected wave changes with the velocity of the moving object. Through this velocity information, the displacement of the piezoelectric actuator can be obtained. The sinusoidal voltage can be generated within the vibrometer machine to the piezoelectric film without the need for an external signal generator and power supply, and the minimum voltage applied in the displacement experiment is 0V. During measurement, the inlet and outlet reservoirs as well as the ELVEFLOW sensor are connected to the micropump to achieve the same fluidic resistance in the flow measurement.

In the ball valve characterization experiment, the inlet and outlet of the micropump are connected to reservoirs respectively. The reservoir is subjected to varying external pressures from 0 mbar to 100 mbar. As the generated flow rate exceeds the measurement range of the flow sensor, the flow rate generated is calculated from the weight change in another reservoir. An electronic weighing scale with a resolution of 0.1 g is used for weight measurement.

In addition, the surface roughness of the 3D-printed prototype and polypropylene balls is also characterized by Keyence Digital Microscope VHX-6000 and Bruker white light interferometer respectively.

5 Results and discussion

5.1 Surface roughness characterization

The upper surface of the 3D printed pump base at 1000x magnification is shown in Figure 6. The Figure demonstrates the layering effect inherent to 3D printing, whereby the object is constructed layer-by-layer. The measured arithmetic mean roughness (R_a) is 2.29 μm and the maximum height of the profile (R_z) is 23.19 μm. This surface roughness is lower than $R_a = 2.3\mu m$, and its effect on fluid boundary transformation is negligible [15].

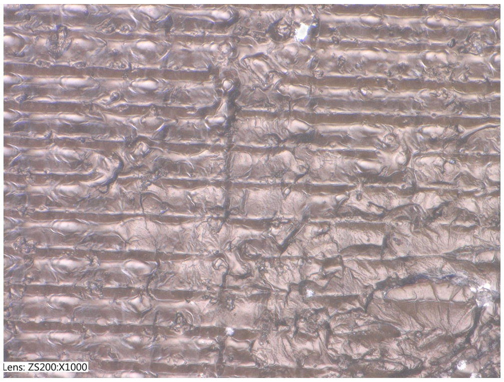

Figure 6: 3D printed prototype at 1000x magnification observed with Keyence Digital Microscope VHX-6000

The surface of the conical channel of the pump base is also shown in Figure 7. Some small cavities are noticed at 300x magnification. The conical channel also has a similar multi-layered structure and the edge of the layer is not smooth.

Figure 7: 3D printed conical channel of pump base at 300x magnification observed with Keyence Digital Microscope VHX-6000

Figure 8 shows the dome surface of a polypropylene ball under Bruker white light interferometer. The Gaussian regression filter removes the tilt and curvature in the measurement software. The measured R_a is 0.848μm and R_z is 19.15μm.

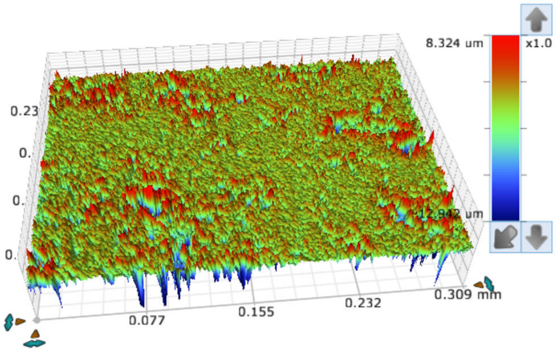

Figure 8: Polypropylene ball at 1000x magnification observed with Keyence Digital Microscope VHX-6000

5.2 Piezoelectric actuator characterization

The deformation observed by the vibrometer on a piezoelectric actuator is shown in Figure 9, with upward motion in suction mode and downward motion in discharge mode. The highest displacement is observed at the central point, with a decrease along with the radius. The displacement at the same radius is distributed uniformly and the influence of the soldering point is neglectable.

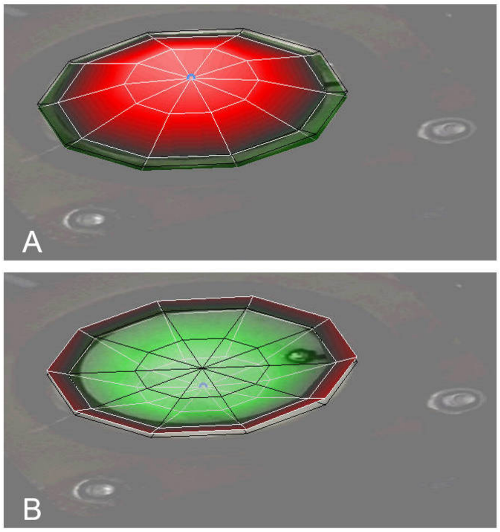

Figure 9: Piezoelectric actuator deformation in (A) suction mode and (B) discharge mode at 43 Hz when a sinusoidal voltage (120 Vpp and 43 Hz) is applied.)

The displacement of the piezoelectric actuator is proportional to the applied voltage, as illustrated in Figure 10. The relationship is linear either in simulation, theory, or experimental results, whereby an increase in the applied voltage results in a proportional increase in displacement. While the measured displacement in the experiment is slightly lower than the simulation results, this discrepancy may be due to the presence of ball valves, which increase the load even when the chamber is filled with air. As the theoretical results are based on Timoshenko's thin plate theory, which assumes the plate is moderately thick, the plate of the piezoelectric actuator used in this project is closer to a thin beam, which unavoidably causes slight differences in the theoretical results.

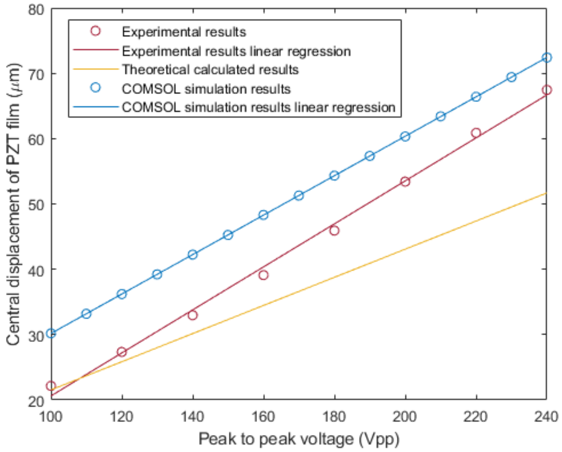

Figure 10: Central displacement-voltage characterization was performed for the experimental, theoretical, and simulated results of the piezoelectric actuator, along with their linear regression lines, as the magnitude of the applied sinusoidal voltage varied, while the frequency was held constant at 5 Hz. The theoretical results were obtained using Equation 3. The R^2 value is 0.99 for the experimental results and 1 for the simulation results.

Frequency is another key factor affecting piezoelectric actuator displacement. Figure 11 illustrates the central displacement of the PZT film concerning the voltage frequency. The micropump is fully assembled and two conditions inside the pump chamber are tested: air-filled and IPA-filled. After being clamped by the O-ring, the resonant frequency of the piezoelectric actuator is 1600 Hz. When the chamber is filled with water, the resonance frequency occurs at 43 Hz as the first mode (shown in Figure 9). This phenomenon can be explained with Equation 12. The introduction of liquid adds virtual mass to the system and therefore lowers the resonant frequency. In addition, both the ball valve and the liquid increase the load of the system and dissipate the energy, reducing the amplitude of deformation at a resonant frequency from 110 μm to 16.8 μm.

5.3 Ball valve characterization

The flow rectification efficiency of the ball valves is characterized by the change in flow rate concerning the applied pressure as illustrated in Figure 12. The tubing for connection also contributes to the fluidic resistance and this value can be calculated by Equation 13, resulting in a value of $R_{tubing} = 2.8 \times 10^8 Pa \cdot s/m^3$. This fluid resistance is neglectable compared with the fluid resistance of the valve, which is estimated in opening mode as $R_{opening} = 5.7 \times 10^{10} Pa \cdot s/m^3$, and $R_{closing} = 1.5 \times 10^{11} Pa \cdot s/m^3$ for the closing mode. Fluidic diodicity η_F is another significant parameter to characterize valve performance and is defined by the ratio of pressure loss coefficients ξ in the positive (valve opening) and negative (valve closing) directions [7]. The calculated η is 6.93.

$$\eta_F = \frac{\xi_-}{\xi_+} \tag{22}$$

Where the pressure loss coefficient ξ is calculated from

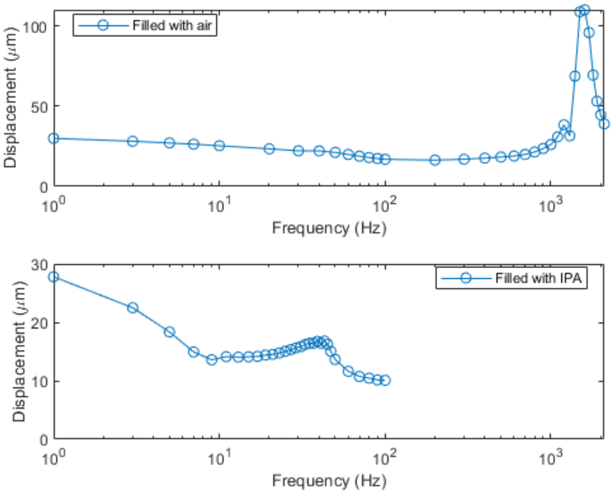

Figure 11: Displacement-frequency characterization of the piezoelectric actuator in a micropump filled with air and IPA, respectively. In all measurements, a sinusoidal voltage of 120 Vpp was applied, while the frequency was varied.

the pressure loss p, fluid density ρ, and average flow velocity u, as shown in Equation 23. The average flow velocity u is related to the flow rate Q and the channel cross-sectional area A as $Q = uA$.

$$\Delta p = \xi \frac{\rho u^2}{2} \tag{23}$$

The flow rectification function of the ball valve is shown in Figure 13. This flow ripple is measured at the outlet of the micropump. The continuous switching between suction and discharge modes causes the flow rate to be displayed as ripples. Although there is some backflow, more fluid tends to flow in the forward direction, with a maximum positive flow rate of 28.7 $\mu L/min$, almost 4.7 times greater than the minimum negative flow rate of 6.1 $\mu L/min$. The low sealing ability may be caused by the cavities in the 3D printed conical channel as shown in Figure 7. Additionally, the poor roundness of the printed conical channel is another possible factor contributing to backflow. Even when the ball makes contact with the wall of the conical channel, fluid can still flow through the gap, preventing the channel from fully closing.

5.4 Micropump characterization

Figure 14 demonstrates the pumping ability of the micropump through the movement of a bubble within the tubing. This figure is intercepted from the video Youtube: micropump working, and the video of the ball valve working is stored at Youtube: ball valve movement.

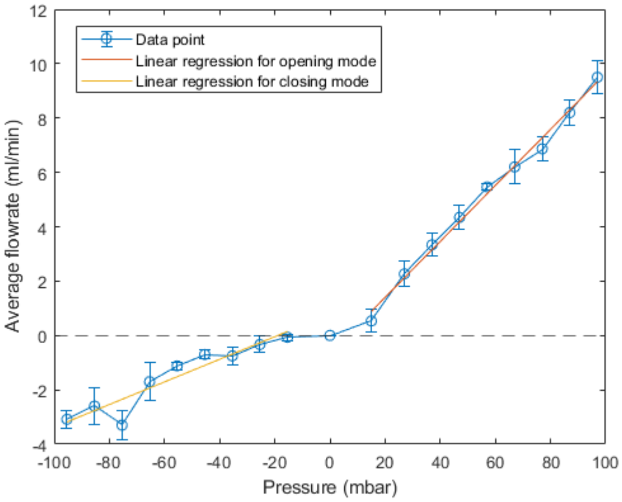

Figure 12: Pressure-average flow rate characterization of the ball valve. Vertical lines indicate the standard deviation of the flow rate in three tests. The red line and yellow line represent linear regressions of the measured points at the valve opening and closing modes, respectively. The R^2 for linear regression is 0.99 for the red line and 0.88 for the yellow line.

The pumping flow rate is mainly influenced by the frequency and voltage applied to the piezoelectric actuator and backpressure.

5.4.1 Flow rate-frequency characterization

Figure 15 illustrates the flow rate change with increasing frequency under 140 Vpp, 190 Vpp, and 240 Vpp sinusoidal voltage. The flow rate follows the same trend across the frequency domain under these three applied voltages. When the frequency is lower than 10Hz, the flow rate increases with the rise in frequency. The maximum flow rate is 26.5 $\mu l/min$ when Vpp 240V sinusoidal voltage with 5Hz is applied. The flow rate remains similar up to several frequencies, which vary slightly according to the changing voltage. At around 10 Hz, the flow rate decreases rapidly until it reaches a low value at 20 Hz. After that, the flow rate decreases slowly. This phenomenon also occurs when the applied voltage is 140 Vpp and 190 Vpp. While the flow rate generated by 240 Vpp shows a slight difference at 35 Hz, where a second flow rate peak is observed. This phenomenon is specific and does not occur in other assembled micropumps (the measured flow rate-frequency characterization results of another two prototypes are listed in the Appendix B: Flow rate - frequency characterization of prototype 1 and prototype 4).

Four prototypes were successfully fabricated and their flow rate-frequency characterization is shown in Figure 16.

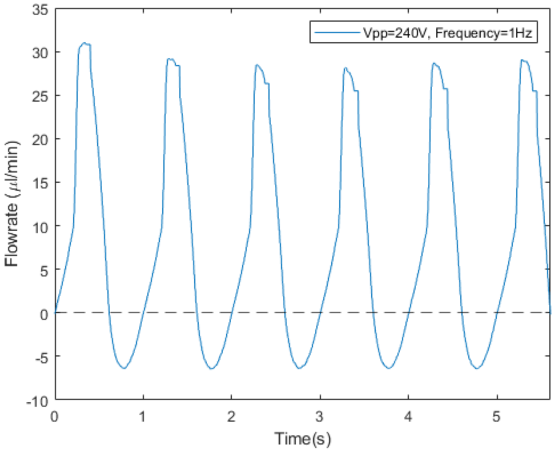

Figure 13: Flow ripple characterization of the micropump when a 240Vpp voltage at 1Hz frequency is applied

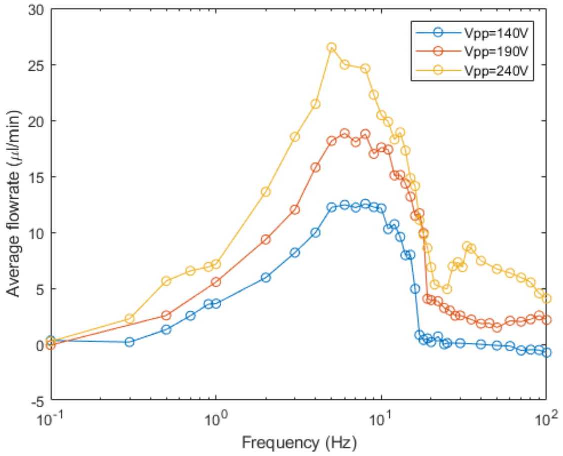

Figure 15: Flow rate-frequency characterization of the micropump at applied voltages of 140 Vpp, 190 Vpp, and 240 Vpp. The data points show the average flow rate of flow ripple.

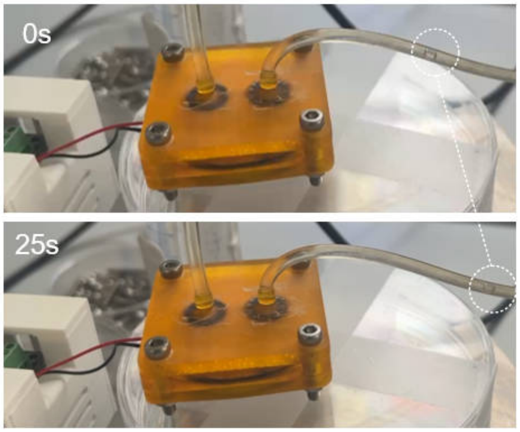

Figure 14: Movement of a bubble in the tubing under low voltage and low-frequency conditions

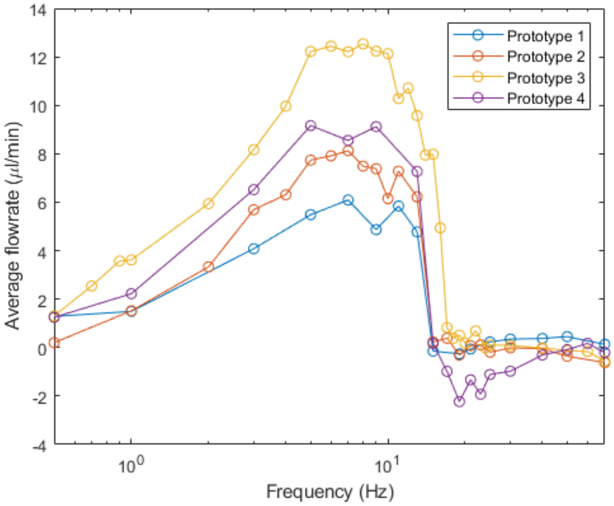

Figure 16: Reproducibility characterization of the micropump. Four prototypes are tested for flow rate-frequency performance when applied with a 140 Vpp sinusoidal voltage.

All of them generate the highest flow rate between 5Hz and 10Hz and have a similar decreasing trend in frequency far away from 10 Hz. However, the flow rate generated by each prototype varies. The standard deviation of the maximum flow rate among these four prototypes is 2.692 $\mu l/min$. Since the device is assembled manually, human error including the addition of different amounts of epoxy, the application of non-uniform force to each clamping nut, the manufacturing tolerances of the PZT film as well as the 3D printed parts all contribute to the specification of prototypes. Since prototype 3 has the best performance among these four devices, the following experiments will be performed with prototype 3.

The ripple frequency characterization measured under 190 Vpp sinusoidal voltage is shown in Figure 17. Vertical lines represent the maximum and minimum flow rate of the ripple compared with the average flow rate. The ripple increases with the frequency and reaches a maximum value of 19.9 $\mu l/min$ at 8 Hz. After 10 Hz, the ripple decreases slowly while this slowing down is less than the rate of decrease of the flow rate. Therefore, the maximum backflow of 6.79 $\mu l/min$ appears at 19 Hz, where the flow rate has decreased to 4.05 $\mu l/min$, but the ripple remains high at 10.84 $\mu l/min$.

Figure 18 compares the experimental results and the theoretical analysis with an equivalent RLC model. The resonance frequency calculated by Equation 20 is 7.16 Hz, slightly higher than the 6 Hz in the experimental results. This difference could be attributed to the ignorance of the membrane mass M in the analysis and the assumption of an ideal valve. However, the trend of the analytical results closely aligns with the experimental data.

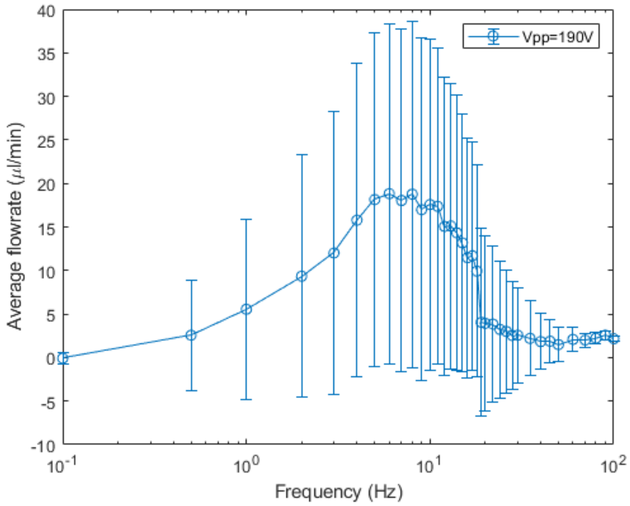

Figure 17: Flow ripple-frequency characterization. The data points are measured under 190 Vpp with sinusoidal voltage and vertical lines indicating the flow ripple's magnitude.

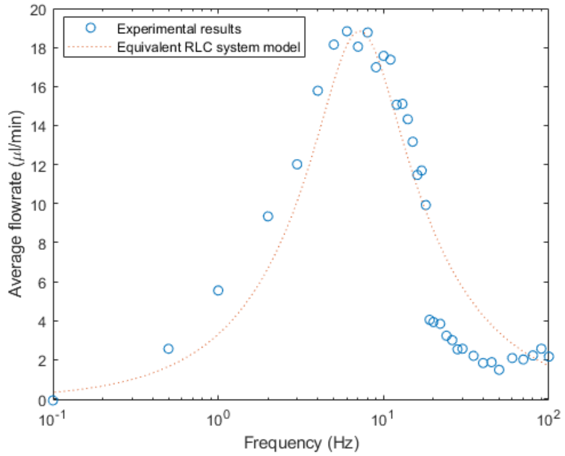

Figure 18: The comparison of flow rate-frequency characterization. The red line is the theoretical calculation results using the Equation 21 and parameters of Table 4. The data points are obtained from the measured flow rate when the applied voltage is 190 Vpp.

Table 4: Parameters for RLC model analysis

Parameters	**Values**
Viscosity of IPA	$2.43 \times 10^{-3} Nsm^{-2}$
Density of IPA	$785 kg/m^3$
Young's modulus of brass	$100 Gpa$
Poisson's ratio of brass	0.34
Young's modulus of PZT-5H	$60 Gpa$
Poisson's ratio of PZT-5H	0.31
Flow rate at resonance frequency	$18.83 \mu l/min$

In summary of the flow rate-frequency behavior of the micropump, the peak flow rate happens around 5 Hz, while theoretical analysis based on the RLC equivalent model gives a close estimate of 7.16 Hz. The difference between these two values may be caused by simplifications in calculating the fluid resistance in the conical channel as well as from ignoring the effects of the membrane's mass and the spring constant generated by the piezoelectric film. However, this frequency is significantly lower than the measured resonant frequency of the piezoelectric actuator as 43 Hz. Kan et al. have verified that valve check efficiency influences flow rate behavior and this difference in frequency is likely due to the check efficiency [16]. Therefore, a hypothesis regarding the reason for the flow rate peak and its rapid drop from 11 Hz is put forward.

As the ball valve operates by the movement of the ball to make contact with the duct wall, and the designed travel is 1.1 mm, the ball valve operates differently at low and high frequencies as shown in Figure 19. In the low-frequency range ($f < f_v$), the ball has sufficient time to move to the closing point and make contact with the wall. The fluid in the reverse direction is stopped by the valve, thereby generating a positive average flow rate. However, in the high-frequency range ($f_v < f$), the ball cannot respond quickly enough, staying nearly stationary within the channel, which compromises its rectification function. Under this condition, the ball loses its function and the flow rate profile becomes symmetric, resulting in a zero average flow rate. The rapid drop observed at 11 Hz in figure 18 of the experimental data confirms this possibility. Due to fluid inertia, a small positive average flow rate persists in the high-frequency range.

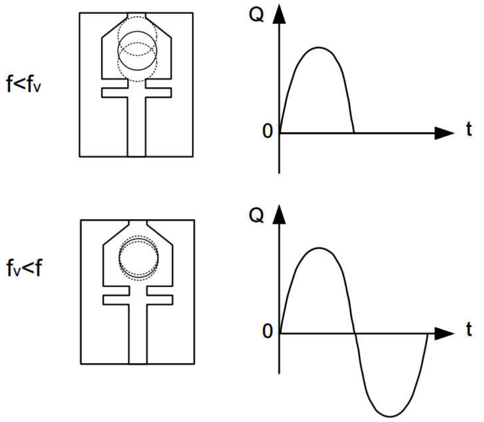

Figure 19: Schematic representation of the state of the ball moving at different frequencies. The dotted line shows the position of the ball after movement.

The displacement-frequency behavior of the piezoelectric actuator when filled with liquid has been measured in figure 11 and is simply illustrated in figure 20 (a). Before f_v, the valve maintains excellent check efficiency to alternate between closing and opening modes. While this efficiency rapidly decreases after f_v, as shown in figure 20(b), where the ball cannot respond in time. This decreasing trend becomes more gradual when the check efficiency approaches zero, with the ball becoming almost stationary, as illustrated in figure 19 for $f_v < f$. The product of check efficiency and frequency results in a peak at f_v. Since flow rate is proportional to frequency, the displacement of the piezoelectric film, and check efficiency (refer to Equation 6), the reduction trend in displacement shifts the frequency of peak flow rate to the lower f_0. Additionally, since the piezoelectric actuator generates a large displacement at its resonance frequency f_a, this may lead to the appearance of a second flow rate peak. This is possibly the reason why a second peak is observed in figure 15 around 35 Hz when a 240 Vpp voltage is applied. The second peak is only observed at the maximum voltage applied because the check efficiency is already very close to zero at f_a. Since the displacement is proportional to to the applied voltage, at lower voltages, displacement increase is not sufficient to produce a significant flow rate due to the effect of the low check efficiency and thus the second peak is not observed in other applied voltage conditions.

5.4.2 Flow rate-voltage characterization

The relationship between flow rate and voltage is shown in the Figure 21. The flow rate is measured at sinusoidal voltages of different frequencies. These results show a similar trend that the flow rate increases as the applied voltage increases. However, the rate of the increase varies with frequency. The gradient is largest at the flow rate peak frequency of 5 Hz and decreases away from this frequency.

Figure 22 shows the change in ripple as the voltage increases. As the voltage increases, the magnitude of the ripple increases with the average flow rate. Note that the minimum flow rate of ripple is almost the same and the maximum flow rate increases. This means an increased closing force on the ball valve failed to achieve an increased closing efficiency. This further confirms the hypothesis that the 3D-printed conical channel wall is not fully in contact with the ball due to the presence of voids, not because the pumping force is insufficient to bring the ball to the closed position.

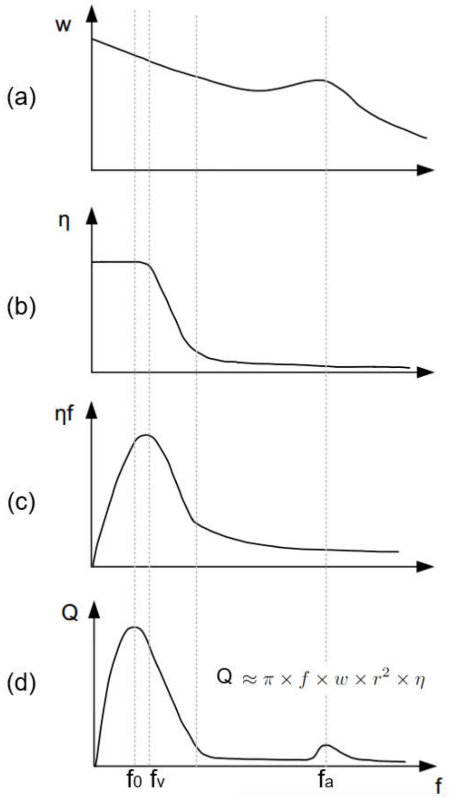

Figure 20: Schematic diagram of the operating frequency's effect on (a) displacement of the piezoelectric actuator (b/c) check efficiency of the valve and (d) flow rate, where f_0 is the frequency of flow rate peak, f_v is the frequency of valve with ideal check efficiency and f_a is the resonance frequency of actuator

5.4.3 Flow rate-backpressure characterization

The flow generated by the micropump is affected by the pressure at the outlet. This pressure is called backpressure. As shown in Figure 23, the introduction of pressure at the outlet does not change the waveform of the generated flow ripple but causes a backflow to the initial zero flow rate. For example, a backpressure of 30 mbar applied at the outlet of the micropump causes a backflow of 24.79 $\mu l/min$, while no backpressure results in a zero flow rate.

Figure 24 illustrates the relationship between the backpressure and flow rate. To eliminate the backflow caused by pressure, the micropump's maximum backpressure must occur at the power setting that delivers the maximum flow rate. Therefore, this maximum back pressure is measured at a threshold voltage of 240 Vpp with the 5Hz. As the backpressure increases, the flow rate decreases linearly. From the linear regression of the measured data points, 36.5 mbar is the maximum backpressure of this unit, at this point the flow drops to zero and further increases in backpressure result in negative flow. Theoretically, applying a backpressure larger than the maximum

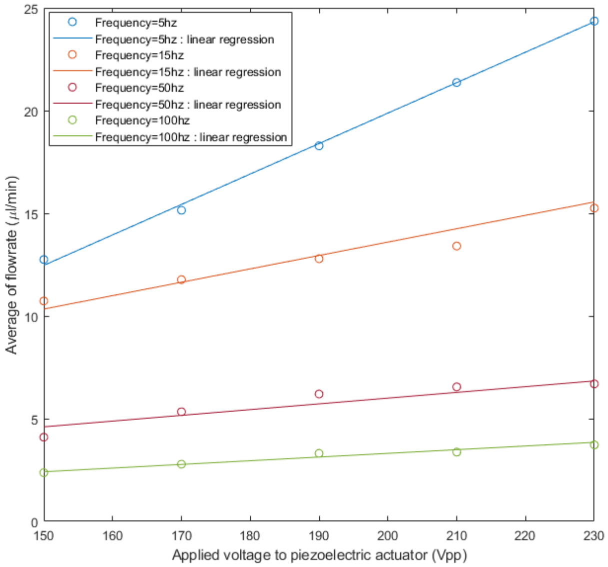

Figure 21: flow rate-voltage characterization of the micropump when voltage with different frequencies is applied. The data points show the average flow rate of flow ripple. The solid line for each frequency represents the linear regression of the data points. The R^2 values for 5 Hz, 15 Hz, 50 Hz, and 100 Hz are 0.99, 0.95, 0.89, and 0.96, respectively.

backpressure should not cause negative backflow but keep the flow rate at zero, as no valve failure occurs. The reason this phenomenon occurs here is that there are still gaps allowing liquid to flow through when the ball is in contact with the channel wall. The complete sealing is not achieved for the closing mode. Small cavities and the low roundness of the 3D-printed channel are two possible reasons for this. As a result, further increases in backpressure lead to an increase in backflow.

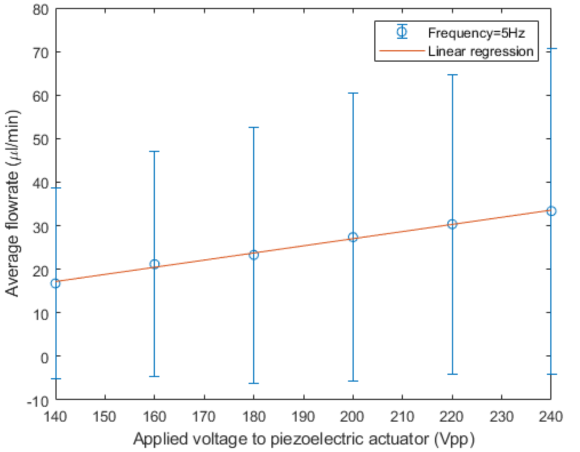

Figure 22: Flow rate-voltage characterization of the micropump when the sinusoidal voltage at 5Hz is applied. The data points show the average flow rate of flow ripple and vertical lines indicate the magnitude of flow ripple compared with the average flow rate. The solid line represents the linear regression of the data points, with an R^2 value of 0.99.

5.5 Micropump Performance comparison

Table 5 lists reported micropumps with ball valves and compare their performance with my prototype. All existing micropumps produce flow rates in the ml/min range, which does not meet the $\mu l/min$ requirements of organ-a-chip devices. In addition, Yamahata et al. and Shen et al. used an electromagnetic actuator to provide power, which increases the external dimension due to the presence of an electromagnet [9] [17]. Carroza et al. utilized stereolithography for fabrication and tedious steps were needed including mask design and complex etching [10]. Pan et al. assembled thirteen layers to form the micropump, the process is rather inconvenient [18]. Whereas the proposed design in this work, the generated flow range matches the

Table 5: Performance comparison of reported micropump with ball valves

First author	Year	Type of actuator	Fabrication method	Maximum backpressure (kPa)	Maximum flow rate (ml/min)	Pressure effect on flow rate (Kpa · min/ml)
Carozza [10]	1995	Piezoelectric actuator	Stereolithography	25	2.7	9.26
Yamahata [9]	2005	Electromagnetic actuator	Powder blasting	28	5	5.6
Shen [17]	2008	Electromagnetic actuator	Powder blasting, precision milling and casting	35	6	5.83
Pan [11]	2021	Piezoelectric actuator	NA	23	99.6	0.2309
This work	2024	Piezoelectric actuator	mSLA 3D printing	3.65	0.0265	137.7358

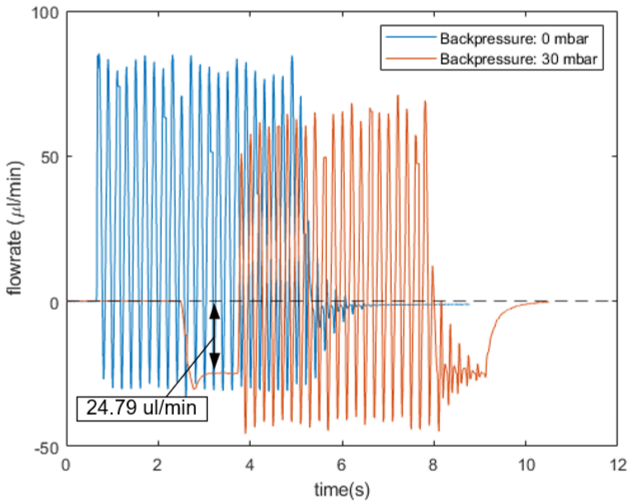

Figure 23: Flow ripple comparison with and without 30 mbar back pressure, where the blue line is the flow ripple with no pressure at the outlet and the orange line is with 30 mbar back pressure.

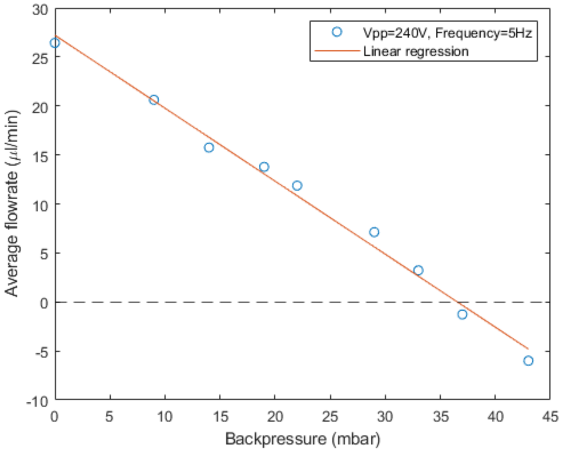

Figure 24: Backpressure-flow rate characterization of micropump when 5Hz, 240 Vpp sinusoidal voltage is applied. The red line is the linear regression result with an R^2 value of 0.99.

flow range of OoC devices. Additionally, the pump's additive manufacturing and assembly can be completed in three hours. Although the maximum backpressure is lower than other reported devices due to the lower maximum flow rate generated. Lower flow rates inevitably result in a lower maximum backpressure that can be withstood compared to a high flow rate pump, as there is not as much forward flow to resist the backflow. Defining the ratio of backpressure versus flow rate as the effect of air pressure on flow rate, it can be seen that the micropump of this work has the highest withstanding capacity of 137.74 KPa · min/ml.

5.6 Optimization discussion

Up to this section, all measured results have been reported and discussed. This section focuses on reviewing the optimization made during the project.

The project started with the fabrication of a monolithic micropump. However, after several attempts at 3D printing and testing, this design had been evidenced to suffer from performance issues. Specifically, the low sphericity of the ball as it was removed from the support and the inertial deformation in the membrane led to the low overall performance of the micropump. Further details on these issues can be found in Appendix A: Additive manufacture of a monolithic micropump.

After that, a new design was proposed. It involves assembling three 3D printed layers with the commercial piezoelectric disk to form a micropump as shown in Figure 1. Failure modes occured during the experiment and some of them were resolved:

5.6.1 Leakage

The pump was initially sealed with four O-rings. The piezoelectric actuator was clamped by two o-rings from top and bottom. However, during the experiments, leakage was still observed as water escaped from the connection of layers as shown in Figure 25 A. This leakage affected the measurement results. Firstly, the flow generated sometimes became a symmetric flow, meaning that the valve did not function, even though the ball had been inserted into the conical channel. Secondly, the measured resonance frequency when the chamber is filled with IPA is almost the same as when it is filled with air.

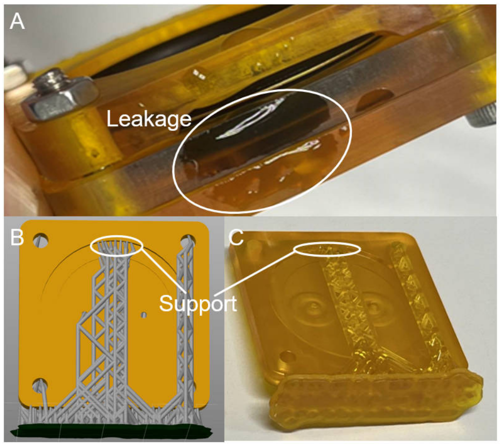

Figure 25: (A) Leakage occurs between clamped 3D printed layers. (B) Printable support is required for printing of the pump chamber part (C) the actual printed support.

Although 30% of the O-ring thickness was reserved as its deformation allowance during the design process, leakage still occurred. The possible reason for the leak is that the 3D-printed surface in contact with the O-ring does not seal. The upper part of the circular chamber is an overhanging structure during printing and requires support to make it printable. Supports are automatically generated in the slicer software. After printing is finished and the supports are removed, small cavities or tips are left at the support points, making the surface not completely flat. Therefore, when the O-ring is placed on the chamber surface and sealed with clamping force, the sealing in these points is weak, making it prone to leakage when the piezoelectric actuator vibrates. Also, To address this problem, epoxy is added to the edge of this joint and remove the rubber under the piezoelectric actuator. To prevent leakage between the pump chamber and the pump base, epoxy is also added to the cavity around the conical channels.

5.6.2 Fluid type

Water was first chosen as pumping fluid, while the flow rate generated was not stable. The maximum ripple in each cycle at the same frequency and voltage applied had a high difference. This was caused by the bubble observed in the water. In addition, the surface tension of water is as high as 72.8 mN/m, which reduces liquid lubrication performance and increases the friction force for the ball movement. Compared with water, IPA has three times lower surface tension at 21.7 mN/m. In addition to reducing fluid friction in the ball valve, it also reduces the tendency for air bubbles to form. The generated flow rate became stable after changing the pumping fluid to IPA.

5.6.3 Crack of piezoelectric actuator

While there is still a problem that can not be solved is about the short lifetime of the piezoelectric actuator. There are summarised reasons for the failure mode of the piezoelectric actuator. Applying a voltage exceeding 240 Vpp and a frequency over 1000 Hz when the chamber is filled with liquid, will result in noticeable cracks on the piezoelectric film, as shown in Figure 26. An electric spark is observed when the crack occurs and the sound emitted by the piezoelectric actuator in the audible frequency range (over 500 Hz) becomes muffled. Even if this critical voltage and frequency are not applied, the piezoelectric actuator will still lose its function after several tests. This problem causes each micropump to have a rather short lifetime, resulting in tens of micropumps being manufactured while only a few of them can successfully be measured. This may be since piezoelectric ceramic is brittle and the higher forces generated can cause it to break during the deformation process.

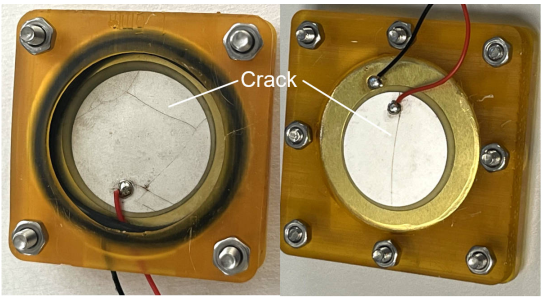

Figure 26: Crack occurs on the piezoelectric film

6 Conclusion

In conclusion, a piezoelectric micropump was fabricated using additive manufacturing in this project. The actuation elements include a piezoelectric film and a brass membrane. The pump cover, chamber, and base were fabricated with an mSLA 3D printer. Several research goals have been achieved:

1. The performance of the micropump is analyzed using equivalent RLC electrical modeling, and a simulation is carried out for the displacement of the piezoelectric actuator.

2. The performance of the micropump is characterized by either its resonance frequency of the piezoelectric actuator or flow rate concerning frequency, voltage, and back pressure. This micropump produces the maximum flow rate of 26.5 $\mu l/min$ when the applied sinusoidal voltage is 240 Vpp at 5 Hz. The maximum back pressure of 36.5 mbar is reported at the power condition.

3. This work confirms the possibility of a valve-based micropump to produce a $\mu l/min$ flow rate and provides a new pump option for OoC applications.

7 Future recommendation

The theoretical analysis of this micropump is limited, as several assumptions are made in both the mass-spring analysis and the RLC equivalent circuit analysis.

Furthermore, the performance of micropump has been characterized and obtained several results. However, there are still some unsubstantiated explanations for certain phenomena. The reason why the flow rate peak occurs at 5 Hz instead of the resonance frequency of the piezoelectric actuator at 43 Hz could be due to the check efficiency of the valve. While this is merely speculation, with no method to verify it. If the check efficiency profile of the ball valve could be obtained, this hypothesis could be further checked and give guidance to expand the working frequency range. Additionally, the rapid drop in flow rate at 11 Hz might be caused by the valve losing its function, suggesting that reducing the ball's moving distance or changing to another type of check valve may address this issue.

References

[1] Chak Ming Leung et al. "A guide to the organ-on-a-chip". en. In: *Nature Reviews Methods Primers* 2.1 (May 2022). Number: 1 Publisher: Nature Publishing Group, pp. 1–29. ISSN: 2662-8449. DOI: 10.1038/s43586-022-00118-6. URL: https://www.nature.com/articles/s43586-022-00118-6 (visited on 12/23/2023).

[2] Gürhan Özkayar et al. "Toward a modular, integrated, miniaturized, and portable microfluidic flow control architecture for organs-on-chips applications". en. In: *Biomicrofluidics* 16.2 (Mar. 2022), p. 021302. ISSN: 1932-1058. DOI: 10.1063/5.0074156. URL: https://pubs.aip.org/bmf/article/16/2/021302/2835420/Toward-a-modular-integrated-miniaturized-and (visited on 09/18/2023).

[3] Farid Amirouche, Yu Zhou, and Tom Johnson. "Current micropump technologies and their biomedical applications". en. In: *Microsystem Technologies* 15.5 (May 2009), pp. 647–666. ISSN: 0946-7076, 1432-1858. DOI: 10.1007/s00542-009-0804-7. URL: http://link.springer.com/10.1007/s00542-009-0804-7 (visited on 09/20/2023).

[4] L. J. Jr Thomas and S. P. Bessman. "PROTOTYPE FOR AN IMPLANTABLE MICROPUMP POWERED BY PIEZOELECTRIC DISK BENDERS". en-US. In: *ASAIO Journal* 21.1 (Apr. 1975), p. 516. ISSN: 1058-2916. URL: https://journals.lww.com/asaiojournal/Citation/1975/21000/Prototype_for_An_Implantable_Micropump_Powered_By.69.aspx (visited on 03/01/2024).

[5] W.J. Spencer et al. "An electronically controlled piezoelectric insulin pump and valves". en. In: *IEEE Transactions on Sonics and Ultrasonics* 25.3 (May 1978), pp. 153–156. ISSN: 0018-9537. DOI: 10.1109/T-SU.1978.31006. URL: http://ieeexplore.ieee.org/document/1539082/ (visited on 03/01/2024).

[6] H. T. G. van Lintel, F. C. M. van De Pol, and S. Bouwstra. "A piezoelectric micropump based on micromachining of silicon". In: *Sensors and Actuators* 15.2 (Oct. 1988), pp. 153–167. ISSN: 0250-6874. DOI: 10.1016/0250-6874(88)87005-7. URL: https://www.sciencedirect.com/science/article/pii/0250687488870057 (visited on 01/22/2024).

[7] Nam-Trung Nguyen, Steven T. Wereley, and Seyed Ali Mousavi Shaegh. *Fundamentals and applications of microfluidics*. en. Third edition. Artech House integrated microsystems series. OCLC: on1056196789. Norwood, Massachusetts: Artech House, 2019. ISBN: 978-1-63081-364-2.

[8] Hengyu Li et al. "A review of recent studies on piezoelectric pumps and their applications". en. In: *Mechanical Systems and Signal Processing* 151 (Apr. 2021), p. 107393. ISSN: 08883270. DOI: 10.1016/j.ymssp.2020.107393. URL: https://linkinghub.elsevier.com/retrieve/pii/S0888327020307792 (visited on 07/27/2023).

[9] Christophe Yamahata et al. "A ball valve micropump in glass fabricated by powder blasting". In: *Sensors and Actuators B: Chemical* 110.1 (Sept. 2005), pp. 1–7. ISSN: 0925-4005. DOI: 10.1016/j.snb.2005.01.005. URL: https://www.sciencedirect.com/science/article/pii/S0925400505000833 (visited on 08/15/2024).

[10] M C Carrozza et al. "A piezoelectric-driven stereolithography-fabricated micropump". en. In: *Journal of Micromechanics and Microengineering* 5.2 (June 1995), pp. 177–179. ISSN: 0960-1317, 1361-6439. DOI: 10.1088/0960-1317/5/2/032. URL: https://iopscience.iop.org/article/10.1088/0960-1317/5/2/032 (visited on 01/22/2024).

[11] Qiaosheng Pan et al. "Development of a piezoelectric pump with ball valve structure". en. In: *Journal of Intelligent Material Systems and Structures* 32.18-19 (Nov. 2021). Publisher: SAGE Publications Ltd STM, pp. 2289–2299. ISSN: 1045-389X. DOI: 10.1177/1045389X21994179. URL: https://doi.org/10.1177/1045389X21994179 (visited on 05/17/2024).

[12] Changki Mo et al. "Behaviour of a unimorph circular piezoelectric actuator". en. In: *Smart Materials and Structures* 15.4 (Aug. 2006), pp. 1094–1102. ISSN: 0964-1726, 1361-665X. DOI: 10.1088/0964-1726/15/4/023. URL: https://iopscience.iop.org/article/10.1088/0964-1726/15/4/023 (visited on 09/18/2023).

[13] Yiwen Fan et al. "Development of a piezoelectric pump with unfixed valve". en. In: *Journal of Micromechanics and Microengineering* 32.5 (May 2022), p. 055004. ISSN: 0960-1317, 1361-6439. DOI:

10.1088/1361-6439/ac60a7. URL: https://iopscience.iop.org/article/10.1088/1361-6439/ac60a7 (visited on 07/29/2023).

[14] Christophe Yamahata. “Magnetically Actuated Micropumps”. PhD thesis. ÉCOLE POLYTECHNIQUE FÉDÉRALE DE LAUSANNE, 2005.

[15] Zhaolin liu and Yan Feng. *Effect of microchannel size and surface roughness on friction coefficient at different pressure differences*. 2012. URL: /article/id/em_5644.

[16] Kan Junwu et al. “Design and test of a high-performance piezoelectric micropump for drug delivery”. en. In: *Sensors and Actuators A: Physical* 121.1 (May 2005), pp. 156–161. ISSN: 09244247. DOI: 10.1016/j.sna.2004.12.002. URL: https://linkinghub.elsevier.com/retrieve/pii/S0924424704008581 (visited on 05/28/2024).

[17] M Shen, C Yamahata, and M A M Gijs. “A high-performance compact electromagnetic actuator for a PMMA ball-valve micropump”. en. In: *Journal of Micromechanics and Microengineering* 18.2 (Feb. 2008), p. 025031. ISSN: 0960-1317, 1361-6439. DOI: 10.1088/0960-1317/18/2/025031. URL: https://iopscience.iop.org/article/10.1088/0960-1317/18/2/025031 (visited on 07/04/2024).

[18] Qiaosheng Pan et al. “Development of a piezoelectric pump with ball valve structure”. en. In: *Journal of Intelligent Material Systems and Structures* 32.18-19 (Nov. 2021). Publisher: SAGE Publications Ltd STM, pp. 2289–2299. ISSN: 1045-389X. DOI: 10.1177/1045389X21994179. URL: https://doi.org/10.1177/1045389X21994179 (visited on 02/12/2024).

References

[1] Chak Ming Leung et al. “A guide to the organ-on-a-chip”. In: *Nature Reviews Methods Primers* 2.1 (May 12, 2022). Number: 1 Publisher: Nature Publishing Group, pp. 1–29. ISSN: 2662-8449. DOI: `10.1038/s43586-022-00118-6`. URL: `https://www.nature.com/articles/s43586-022-00118-6` (visited on 12/23/2023).

[2] Gürhan Özkayar et al. “Flow Ripple Reduction in Reciprocating Pumps by Multi-Phase Rectification”. In: *Sensors* 23.15 (Aug. 5, 2023), p. 6967. ISSN: 1424-8220. DOI: `10.3390/s23156967`. URL: `https://www.mdpi.com/1424-8220/23/15/6967` (visited on 09/18/2023).

[3] L R Williams and R W Leggett. “Reference values for resting blood flow to organs of man”. In: *Clinical Physics and Physiological Measurement* 10.3 (Aug. 1989), pp. 187–217. ISSN: 0143-0815. DOI: `10.1088/0143-0815/10/3/001`. URL: `https://iopscience.iop.org/article/10.1088/0143-0815/10/3/001` (visited on 12/15/2023).

[4] Gürhan Özkayar et al. “Toward a modular, integrated, miniaturized, and portable microfluidic flow control architecture for organs-on-chips applications”. In: *Biomicrofluidics* 16.2 (Mar. 1, 2022), p. 021302. ISSN: 1932-1058. DOI: `10.1063/5.0074156`. URL: `https://pubs.aip.org/bmf/article/16/2/021302/2835420/Toward-a-modular-integrated-miniaturized-and` (visited on 09/18/2023).

[5] H. T. G. van Lintel, F. C. M. van De Pol, and S. Bouwstra. “A piezoelectric micropump based on micromachining of silicon”. In: *Sensors and Actuators* 15.2 (Oct. 1, 1988), pp. 153–167. ISSN: 0250-6874. DOI: `10.1016/0250-6874(88)87005-7`. URL: `https://www.sciencedirect.com/science/article/pii/0250687488870057` (visited on 01/22/2024).

[6] Abdou Mbaye et al. “3D Printed Micro Check Valve for Biomedical Applications”. In: *IOP Conference Series: Materials Science and Engineering* 417 (Oct. 19, 2018), p. 012041. ISSN: 1757-899X. DOI: `10.1088/1757-899X/417/1/012041`. URL: `https://iopscience.iop.org/article/10.1088/1757-899X/417/1/012041` (visited on 01/22/2024).

[7] I V Uvarov et al. “A simple electrochemical micropump: Design and fabrication”. In: *Journal of Physics: Conference Series* 741 (Aug. 2016), p. 012167. ISSN: 1742-6588, 1742-6596. DOI: `10.1088/1742-6596/741/1/012167`. URL: `https://iopscience.iop.org/article/10.1088/1742-6596/741/1/012167` (visited on 03/02/2024).

[8] Nam-Trung Nguyen, Steven T. Wereley, and Seyed Ali Mousavi Shaegh. *Fundamentals and applications of microfluidics*. Third edition. Artech House integrated microsystems series. OCLC: on1056196789. Norwood, Massachusetts: Artech House, 2019. 548 pp. ISBN: 978-1-63081-364-2.

[9] Hamid Asadi Dereshgi, Huseyin Dal, and Mustafa Zahid Yildiz. “Piezoelectric micropumps: state of the art review”. In: *Microsystem Technologies* 27.12 (Dec. 2021), pp. 4127–4155. ISSN: 0946-7076, 1432-1858. DOI: `10.1007/s00542-020-05190-0`. URL: `https://link.springer.com/10.1007/s00542-020-05190-0` (visited on 09/18/2023).

[10] Farid Amirouche, Yu Zhou, and Tom Johnson. “Current micropump technologies and their biomedical applications”. In: *Microsystem Technologies* 15.5 (May 2009), pp. 647–666. ISSN: 0946-7076, 1432-1858. DOI: `10.1007/s00542-009-0804-7`. URL: `http://link.springer.com/10.1007/s00542-009-0804-7` (visited on 09/20/2023).

[11] Hengyu Li et al. “A review of recent studies on piezoelectric pumps and their applications”. In: *Mechanical Systems and Signal Processing* 151 (Apr. 2021), p. 107393. ISSN: 08883270. DOI: `10.1016/j.ymssp.2020.107393`. URL: `https://linkinghub.elsevier.com/retrieve/pii/S0888327020307792` (visited on 07/27/2023).

[12] Eiji Makino, Takashi Mitsuya, and Takayuki Shibata. “Fabrication of TiNi shape memory micropump”. In: *Sensors and Actuators A: Physical* 88.3 (Jan. 5, 2001), pp. 256–262. ISSN: 0924-4247. DOI: `10.1016/S0924-4247(00)00522-7`. URL: `https://www.sciencedirect.com/science/article/pii/S0924424700005227` (visited on 12/24/2023).

[13] R. Linnemann et al. “A self-priming and bubble-tolerant piezoelectric silicon micropump for liquids and gases”. In: *Proceedings MEMS 98. IEEE. Eleventh Annual International Workshop on Micro Electro Mechanical Systems. An Investigation of Micro Structures, Sensors, Actuators, Machines and Systems (Cat. No.98CH36176*. Proceedings IEEE Eleventh Annual International Workshop on Micro Electro Mechanical Systems An Investigation of Micro Structures, Sensors, Actuators, Machines and Systems. Heidelberg, Germany: IEEE, 1998, pp. 532–537. ISBN: 978-0-7803-4412-9. DOI: `10.1109/MEMSYS.1998.659814`. URL: `https://ieeexplore.ieee.org/document/659814/` (visited on 09/18/2023).

[14] Rui M. R. Pinto et al. “CMOS-Integrated Aluminum Nitride MEMS: A Review”. In: *Journal of Microelectromechanical Systems* 31.4 (Aug. 2022), pp. 500–523. ISSN: 1057-7157, 1941-0158. DOI: `10.1109/JMEMS.2022.3172766`. URL: `https://ieeexplore.ieee.org/document/9774849/` (visited on 09/25/2023).

[15] Liangke Wu et al. “Recent advances in the preparation of PVDF-based piezoelectric materials”. In: *Nanotechnology Reviews* 11.1 (Mar. 25, 2022), pp. 1386–1407. ISSN: 2191-9097. DOI: `10.1515/ntrev-2022-0082`. URL: `https://www.degruyter.com/document/doi/10.1515/ntrev-2022-0082/html` (visited on 12/19/2023).

[16] Michael Koch et al. “A novel micromachined pump based on thick-film piezoelectric actuation”. In: *Sensors and Actuators A: Physical* 70.1 (1998), pp. 98–103. ISSN: 0924-4247. DOI: `https://doi.org/10.1016/S0924-4247(98)00120-4`. URL: `https://www.sciencedirect.com/science/article/pii/S0924424798001204`.

[17] Guo-Hua Feng and Eun Sok Kim. “Micropump based on PZT unimorph and one-way parylene valves”. In: *Journal of Micromechanics and Microengineering* 14.4 (Apr. 1, 2004), pp. 429–435. ISSN: 0960-1317, 1361-6439. DOI: `10.1088/0960-1317/14/4/001`. URL: `https://iopscience.iop.org/article/10.1088/0960-1317/14/4/001` (visited on 09/26/2023).

[18] Yi Luo, Miao Lu, and Tianhong Cui. “A polymer-based bidirectional micropump driven by a PZT bimorph”. In: *Microsystem Technologies* 17.3 (Mar. 2011), pp. 403–409. ISSN: 0946-7076, 1432-1858. DOI: `10.1007/s00542-010-1199-1`. URL: `http://link.springer.com/10.1007/s00542-010-1199-1` (visited on 01/25/2024).

[19] Ping Zeng et al. “Structure design and experimental study on single-bimorph double-acting check-valve piezoelectric pump”. In: *Proceedings of the Institution of Mechanical Engineers, Part C: Journal of Mechanical Engineering Science* 230.14 (Aug. 2016), pp. 2339–2344. ISSN: 0954-4062, 2041-2983. DOI: `10.1177/0954406215596357`. URL: `http://journals.sagepub.com/doi/10.1177/0954406215596357` (visited on 01/25/2024).

[20] Lipeng He et al. “Exploration on relationship between flow rate and sound pressure level of piezoelectric pump”. In: *Microsystem Technologies* 26.2 (Feb. 1, 2020), pp. 609–616. ISSN: 1432-1858. DOI: `10.1007/s00542-019-04553-6`. URL: `https://doi.org/10.1007/s00542-019-04553-6` (visited on 10/04/2023).

[21] Arun Gunda et al. “Proportional Microvalve Using a Unimorph Piezoelectric Microactuator”. In: *Micromachines* 11.2 (Jan. 24, 2020), p. 130. ISSN: 2072-666X. DOI: `10.3390/mi11020130`. URL: `https://www.mdpi.com/2072-666X/11/2/130` (visited on 09/18/2023).

[22] M D Nguyen et al. “Characterization of epitaxial Pb(Zr,Ti)O $_3$ thin films deposited by pulsed laser deposition on silicon cantilevers”. In: *Journal of Micromechanics and Microengineering* 20.8 (Aug. 1, 2010), p. 085022. ISSN: 0960-1317, 1361-6439. DOI: `10.1088/0960-1317/20/8/085022`. URL: `https://iopscience.iop.org/article/10.1088/0960-1317/20/8/085022` (visited on 11/13/2023).

[23] Bing-Huei Chen et al. “Fabrication of PZT BY sol-gel method”. In: *Proceedings of the 2010 Symposium on Piezoelectricity, Acoustic Waves and Device Applications*. 2010 Symposium on Piezoelectricity, Acoustic Waves, and Device Applications (SPAWDA 2010). Xiamen, China: IEEE, Dec. 2010, pp. 310–314. ISBN: 978-1-4244-9822-2. DOI: `10.1109/SPAWDA.2010.5744326`. URL: `http://ieeexplore.ieee.org/document/5744326/` (visited on 03/04/2024).

[24] B. Naveen Kumar et al. “Review on PZT as a mechanical engineering material”. In: *Ferroelectrics* 618.1 (Jan. 2, 2024), pp. 125–138. ISSN: 0015-0193, 1563-5112. DOI: `10.1080/00150193.2023.2271321`. URL: `https://www.tandfonline.com/doi/full/10.1080/00150193.2023.2271321` (visited on 03/04/2024).

[25] Yongquan Su et al. “A two-step wet etching process of PZT thin film with ultra-low undercut for MEMS applications”. In: *Sensors and Actuators A: Physical* 349 (Jan. 2023), p. 114014. ISSN: 09244247. DOI: `10.1016/j.sna.2022.114014`. URL: `https://linkinghub.elsevier.com/retrieve/pii/S0924424722006495` (visited on 01/25/2024).

[26] Gulnur Kalimuldina et al. “A Review of Piezoelectric PVDF Film by Electrospinning and Its Applications”. In: *Sensors* 20.18 (Sept. 12, 2020), p. 5214. ISSN: 1424-8220. DOI: `10.3390/s20185214`. URL: `https://www.mdpi.com/1424-8220/20/18/5214` (visited on 12/19/2023).

[27] Yao Fu et al. “Design, fabrication and testing of piezoelectric polymer PVDF microactuators”. In: *Smart Materials and Structures* 15.1 (Feb. 1, 2006), S141–S146. ISSN: 0964-1726, 1361-665X. DOI: `10.1088/0964-1726/15/1/023`. URL: `https://iopscience.iop.org/article/10.1088/0964-1726/15/1/023` (visited on 12/19/2023).

[28] Laixia Nian et al. “Preparation, Characterization, and Application of AlN/ScAlN Composite Thin Films”. In: *Micromachines* 14.3 (Mar. 2023). Number: 3 Publisher: Multidisciplinary Digital Publishing Institute, p. 557. ISSN: 2072-666X. DOI: `10.3390/mi14030557`. URL: `https://www.mdpi.com/2072-666X/14/3/557` (visited on 09/26/2023).

[29] Yiwen Fan et al. “Development of a piezoelectric pump with unfixed valve”. In: *Journal of Micromechanics and Microengineering* 32.5 (May 1, 2022), p. 055004. ISSN: 0960-1317, 1361-6439. DOI: `10.1088/1361-6439/ac60a7`. URL: `https://iopscience.iop.org/article/10.1088/1361-6439/ac60a7` (visited on 07/29/2023).

[30] Yi-Ning Yang, Suz-Kai Hsiung, and Gwo-Bin Lee. “A pneumatic micropump incorporated with a normally closed valve capable of generating a high pumping rate and a high back pressure”. In: *Microfluidics and Nanofluidics* 6.6 (June 2009), pp. 823–833. ISSN: 1613-4982, 1613-4990. DOI: `10.1007/s10404-008-0356-7`. URL: `http://link.springer.com/10.1007/s10404-008-0356-7` (visited on 02/18/2024).

[31] Xiaoqiang Wu et al. “Advances in passive check valve piezoelectric pumps”. In: *Sensors and Actuators A: Physical* 323 (June 2021), p. 112647. ISSN: 09244247. DOI: `10.1016/j.sna.2021.112647`. URL: `https://linkinghub.elsevier.com/retrieve/pii/S0924424721001096` (visited on 09/18/2023).

[32] Nam-Trung Nguyen and Thai-Quang Truong. “A fully polymeric micropump with piezoelectric actuator”. In: *Sensors and Actuators B: Chemical* 97.1 (Jan. 1, 2004), pp. 137–143. ISSN: 0925-4005. DOI: `10.1016/S0925-4005(03)00521-5`. URL: `https://www.sciencedirect.com/science/article/pii/S0925400503005215` (visited on 10/03/2023).

[33] Fraunhofer. *Micropumps*. Feb. 21, 2024. URL: `https://www.emft.fraunhofer.de/en/research-development/micropumps.html`.

[34] mikrotechnik Bartels. *mp6 micropumps for liquids and gases*. Feb. 21, 2024. URL: `https://www.bartels-mikrotechnik.de/en/micropumps/`.

[35] M C Carrozza et al. “A piezoelectric-driven stereolithography-fabricated micropump”. In: *Journal of Micromechanics and Microengineering* 5.2 (June 1, 1995), pp. 177–179. ISSN: 0960-1317, 1361-6439. DOI: `10.1088/0960-1317/5/2/032`. URL: `https://iopscience.iop.org/article/10.1088/0960-1317/5/2/032` (visited on 01/22/2024).

[36] Christophe Yamahata et al. “A ball valve micropump in glass fabricated by powder blasting”. In: *Sensors and Actuators B: Chemical* 110.1 (Sept. 30, 2005), pp. 1–7. ISSN: 0925-4005. DOI: `10.1016/j.snb.2005.01.005`. URL: `https://www.sciencedirect.com/science/article/pii/S0925400505000833` (visited on 02/21/2024).

[37] Meng Shen, Christophe Yamahata, and Martin A. M. Gijs. “Miniaturized PMMA ball-valve micropump with cylindrical electromagnetic actuator”. In: *Microelectronic Engineering*. Proceedings of the Micro- and Nano-Engineering 2007 Conference 85.5 (May 1, 2008), pp. 1104–1107. ISSN: 0167-9317. DOI: `10.1016/j.mee.2007.12.013`. URL: `https://www.sciencedirect.com/science/article/pii/S0167931707007654` (visited on 02/12/2024).

[38] H. K. Ma et al. “Development and application of a diaphragm micro-pump with piezoelectric device”. In: *Microsystem Technologies* 14.7 (July 2008), pp. 1001–1007. ISSN: 0946-7076, 1432-1858. DOI: `10.1007/s00542-007-0462-6`. URL: `http://link.springer.com/10.1007/s00542-007-0462-6` (visited on 02/12/2024).

[39] Junwu Kan et al. “Development of serial-connection piezoelectric pumps”. In: *Sensors and Actuators A: Physical* 144.2 (June 15, 2008), pp. 321–327. ISSN: 0924-4247. DOI: `10.1016/j.sna.2008.01.016`. URL: `https://www.sciencedirect.com/science/article/pii/S0924424708000848` (visited on 02/12/2024).

[40] J.-H. Park et al. “A study on high-output piezoelectric micropumps for application in DMFC”. In: *Journal of Electroceramics* 30.1 (Apr. 1, 2013), pp. 102–107. ISSN: 1573-8663. DOI: `10.1007/s10832-012-9740-5`. URL: `https://doi.org/10.1007/s10832-012-9740-5` (visited on 02/12/2024).

[41] Chiang-Ho Cheng and Yi-Pin Tseng. “Characteristic studies of the piezoelectrically actuated micropump with check valve”. In: *Microsystem Technologies* 19.11 (Nov. 2013), pp. 1707–1715. ISSN: 0946-7076, 1432-1858. DOI: `10.1007/s00542-013-1857-1`. URL: `http://link.springer.com/10.1007/s00542-013-1857-1` (visited on 02/12/2024).

[42] Xue Yan Wang et al. “A compact and high flow-rate piezoelectric micropump with a folded vibrator”. In: *Smart Materials and Structures* 23.11 (Sept. 2014). Publisher: IOP Publishing, p. 115005. ISSN: 0964-1726. DOI: `10.1088/0964-1726/23/11/115005`. URL: `https://dx.doi.org/10.1088/0964-1726/23/11/115005` (visited on 02/12/2024).

[43] Jian Chen, Dan Huang, and Zhi Hua Feng. “A U-shaped piezoelectric resonator for a compact and high-performance pump system”. In: *Smart Materials and Structures* 24.10 (Sept. 2015). Publisher: IOP Publishing, p. 105009. ISSN: 0964-1726. DOI: `10.1088/0964-1726/24/10/105009`. URL: `https://dx.doi.org/10.1088/0964-1726/24/10/105009` (visited on 02/12/2024).

[44] Hsiao-Kang Ma, Wen-Fu Luo, and Jui-Yu Lin. “Development of a piezoelectric micropump with novel separable design for medical applications”. In: *Sensors and Actuators A: Physical* 236 (Dec. 1, 2015), pp. 57–66. ISSN: 0924-4247. DOI: `10.1016/j.sna.2015.10.010`. URL: `https://www.sciencedirect.com/science/article/pii/S0924424715301710` (visited on 02/20/2024).

[45] Zhonghua Zhang et al. “Development of a self-sensing piezoelectric pump with a bimorph transducer”. In: *Journal of Intelligent Material Systems and Structures* 27.5 (Mar. 1, 2016). Publisher: SAGE Publications Ltd STM, pp. 581–591. ISSN: 1045-389X. DOI: `10.1177/1045389X15575082`. URL: `https://doi.org/10.1177/1045389X15575082` (visited on 02/12/2024).

[46] Jing Shi Dong et al. “Design and experimental research on piezoelectric pump with triple vibrators”. In: *Microsystem Technologies* 23.8 (Aug. 2017), pp. 3019–3026. ISSN: 0946-7076, 1432-1858. DOI: `10.1007/s00542-016-3029-6`. URL: `http://link.springer.com/10.1007/s00542-016-3029-6` (visited on 02/12/2024).

[47] Jing Shi Dong et al. “Design of a piezoelectric pump with dual vibrators”. In: *Sensors and Actuators A: Physical* 257 (Apr. 2017), pp. 165–172. ISSN: 09244247. DOI: `10.1016/j.sna.2017.02.001`. URL: `https://linkinghub.elsevier.com/retrieve/pii/S0924424717302078` (visited on 02/12/2024).

[48] Jai-Hyuk Hwang et al. “Pressurization Characteristics of a Piezoelectric-Hydraulic Pump for UAV Brake Systems”. In: *International Journal of Aeronautical and Space Sciences* 19.3 (Sept. 1, 2018), pp. 776–784. ISSN: 2093-2480. DOI: `10.1007/s42405-018-0058-7`. URL: `https://doi.org/10.1007/s42405-018-0058-7` (visited on 02/12/2024).

[49] Taijiang Peng et al. “A high-flow, self-filling piezoelectric pump driven by hybrid connected multiple chambers with umbrella-shaped valves”. In: *Sensors and Actuators B: Chemical* 301 (Dec. 12, 2019), p. 126961. ISSN: 0925-4005. DOI: `10.1016/j.snb.2019.126961`. URL: `https://www.sciencedirect.com/science/article/pii/S0925400519311608` (visited on 02/12/2024).

[50] Jangmi Woo, Dong Kee Sohn, and Han Seo Ko. “Performance and flow analysis of small piezo pump”. In: *Sensors and Actuators A: Physical* 301 (Jan. 1, 2020), p. 111766. ISSN: 0924-4247. DOI: `10.1016/j.sna.2019.111766`. URL: `https://www.sciencedirect.com/science/article/pii/S0924424719317005` (visited on 02/12/2024).

[51] Jingshi Dong et al. “Performance of single piezoelectric vibrator micropump with check valve”. In: *Journal of Intelligent Material Systems and Structures* 31.1 (Jan. 1, 2020). Publisher: SAGE Publications Ltd STM, pp. 117–126. ISSN: 1045-389X. DOI: `10.1177/1045389X19880024`. URL: `https://doi.org/10.1177/1045389X19880024` (visited on 02/12/2024).

[52] Qiaosheng Pan et al. “Development of a piezoelectric pump with ball valve structure”. In: *Journal of Intelligent Material Systems and Structures* 32.18 (Nov. 1, 2021). Publisher: SAGE Publications Ltd STM, pp. 2289–2299. ISSN: 1045-389X. DOI: `10.1177/1045389X21994179`. URL: `https://doi.org/10.1177/1045389X21994179` (visited on 02/20/2024).

[53] Lipeng He et al. “Experiment analysis of high output pressure piezoelectric pump with straight arm wheeled check valve”. In: *Journal of Intelligent Material Systems and Structures* 32.17 (Oct. 1, 2021). Publisher: SAGE Publications Ltd STM, pp. 1987–1996. ISSN: 1045-389X. DOI: `10.1177/1045389X20987003`. URL: `https://doi.org/10.1177/1045389X20987003` (visited on 10/23/2023).

[54] Qiufeng Yan et al. “Advances in Valveless Piezoelectric Pumps”. In: *Applied Sciences* 11.15 (Jan. 2021). Number: 15 Publisher: Multidisciplinary Digital Publishing Institute, p. 7061. ISSN: 2076-3417. DOI: `10.3390/app11157061`. URL: `https://www.mdpi.com/2076-3417/11/15/7061` (visited on 10/24/2023).

[55] Erik Stemme and Göran Stemme. “A valveless diffuser/nozzle-based fluid pump”. In: *Sensors and Actuators A: Physical* 39.2 (Nov. 1993), pp. 159–167. ISSN: 09244247. DOI: `10.1016/0924-4247(93)80213-Z`. URL: `https://linkinghub.elsevier.com/retrieve/pii/092442479380213Z` (visited on 10/24/2023).

[56] Ching-Jiun Lee et al. “A study of PZT valveless micropump with asymmetric obstacles”. In: *Microsystem Technologies* 15.7 (July 2009), pp. 993–1000. ISSN: 0946-7076, 1432-1858. DOI: `10.1007/s00542-009-0839-9`. URL: `http://link.springer.com/10.1007/s00542-009-0839-9` (visited on 02/26/2024).

[57] A. Olsson et al. “Micromachined flat-walled valveless diffuser pumps”. In: *Journal of Microelectromechanical Systems* 6.2 (June 1997), pp. 161–166. ISSN: 10577157. DOI: `10.1109/84.585794`. URL: `http://ieeexplore.ieee.org/document/585794/` (visited on 02/14/2024).

[58] Nam-Trung Nguyen and Xiaoyang Huang. “Miniature valveless pumps based on printed circuit board technique”. In: *Sensors and Actuators A: Physical* 88.2 (Feb. 15, 2001), pp. 104–111. ISSN: 0924-4247. DOI: `10.1016/S0924-4247(00)00500-8`. URL: `https://www.sciencedirect.com/science/article/pii/S0924424700005008` (visited on 02/14/2024).

[59] Li-Yu Tseng et al. “Investigation of a piezoelectric valveless micropump with an integrated stainless-steel diffuser/nozzle bulge-piece design”. In: *Smart Materials and Structures* 22.8 (July 2013). Publisher: IOP Publishing, p. 085023. ISSN: 0964-1726. DOI: `10.1088/0964-1726/22/8/085023`. URL: `https://dx.doi.org/10.1088/0964-1726/22/8/085023` (visited on 02/14/2024).

[60] Jun Huang et al. “Theory and experimental verification on valveless piezoelectric pump with multistage Y-shape treelike bifurcate tubes”. In: *Chinese Journal of Mechanical Engineering* 26.3 (May 2013), pp. 462–468. ISSN: 1000-9345, 2192-8258. DOI: `10.3901/CJME.2013.03.462`. URL: `http://link.springer.com/10.3901/CJME.2013.03.462` (visited on 02/13/2024).

[61] Yongming Yao et al. “Valveless Piezoelectric Pump with Reverse Diversion Channel”. In: *Electronics* 10.14 (Jan. 2021). Number: 14 Publisher: Multidisciplinary Digital Publishing Institute, p. 1712. ISSN: 2079-9292. DOI: `10.3390/electronics10141712`. URL: `https://www.mdpi.com/2079-9292/10/14/1712` (visited on 02/14/2024).

[62] Quynh M. Nguyen, Joanna Abouezzi, and Leif Ristroph. “Early turbulence and pulsatile flows enhance diodicity of Tesla’s macrofluidic valve”. In: *Nature Communications* 12.1 (May 17, 2021). Number: 1 Publisher: Nature Publishing Group, p. 2884. ISSN: 2041-1723. DOI: `10.1038/s41467-021-23009-y`. URL: `https://www.nature.com/articles/s41467-021-23009-y` (visited on 02/13/2024).

[63] Teng Yong Ng and Khin Yong Lam. “(73) Assignee: Institute of High Performance”. U.S. pat. 6,910,869 B2. July 28, 2005. URL: `https://patentimages.storage.googleapis.com/ca/3b/08/f7d60cdf818588/US6910869.pdf`.

[64] Lu Wang et al. “A high flow-rate single-chamber valveless piezoelectric pump with airfoil baffles”. In: *Sensors and Actuators A: Physical* 354 (May 2023), p. 114229. ISSN: 09244247. DOI: `10.1016/j.sna.2023.114229`. URL: `https://linkinghub.elsevier.com/retrieve/pii/S092442472300078X` (visited on 12/17/2023).

[65] Jing Ji et al. “Theoretical analysis and experimental verification on valve-less piezoelectric pump with hemisphere-segment bluff-body”. In: *Chinese Journal of Mechanical Engineering* 27.3 (May 2014), pp. 595–605. ISSN: 1000-9345, 2192-8258. DOI: `10.3901/CJME.2014.03.595`. URL: `http://link.springer.com/10.3901/CJME.2014.03.595` (visited on 01/17/2024).

[66] Da Zhao et al. “Experimental analysis of a valve-less piezoelectric micropump with crescent-shaped structure”. In: *Journal of Micromechanics and Microengineering* 29.10 (Oct. 1, 2019), p. 105004. ISSN: 0960-1317, 1361-6439. DOI: `10.1088/1361-6439/ab3278`. URL: `https://iopscience.iop.org/article/10.1088/1361-6439/ab3278` (visited on 02/14/2024).

[67] Bangcheng Zhang et al. “Research on double-outlet valveless piezoelectric pump with fluid guiding body”. In: *Sensors and Actuators A: Physical* 302 (Feb. 1, 2020), p. 111785. ISSN: 0924-4247. DOI: `10.1016/j.sna.2019.111785`. URL: `https://www.sciencedirect.com/science/article/pii/S0924424718322167` (visited on 02/14/2024).

[68] Jun Huang et al. “Development and performance comparison of valveless piezoelectric pumps with asymmetrical channels”. In: *Sensors and Actuators A: Physical* 314 (Oct. 15, 2020), p. 112241. ISSN: 0924-4247. DOI: `10.1016/j.sna.2020.112241`. URL: `https://www.sciencedirect.com/science/article/pii/S0924424719322332` (visited on 02/13/2024).

[69] Thomas Lemke et al. “A high performance bidirectional micropump utilizing advanced low voltage piezo multilayer actuator technology for a novel artificial sphincter system”. In: *4th European Conference of the International Federation for Medical and Biological Engineering*. Ed. by Jos Vander Sloten et al. Berlin, Heidelberg: Springer Berlin Heidelberg, 2009, pp. 1517–1520. ISBN: 978-3-540-89208-3.

[70] Jin-Ho Kim et al. “A disposable thermopneumatic-actuated micropump stacked with PDMS layers and ITO-coated glass”. In: *Sensors and Actuators A: Physical* 120.2 (May 17, 2005), pp. 365–369. ISSN: 0924-4247. DOI: `10.1016/j.sna.2004.12.024`. URL: `https://www.sciencedirect.com/science/article/pii/S0924424704008805` (visited on 10/19/2023).

[71] Kan Junwu et al. “Design and test of a high-performance piezoelectric micropump for drug delivery”. In: *Sensors and Actuators A: Physical* 121.1 (2005), pp. 156–161. ISSN: 0924-4247. DOI: `https://doi.org/10.1016/j.sna.2004.12.002`. URL: `https://www.sciencedirect.com/science/article/pii/S0924424704008581`.

[72] H. K. Ma, R. H. Chen, and Y. H. Hsu. “Development of a piezoelectric-driven miniature pump for biomedical applications”. In: *Sensors and Actuators A: Physical* 234 (Oct. 1, 2015), pp. 23–33. ISSN: 0924-4247. DOI: `10.1016/j.sna.2015.08.003`. URL: `https://www.sciencedirect.com/science/article/pii/S0924424715300959` (visited on 02/20/2024).

[73] Wessel W. Wits, Sander J. Weitkamp, and Johannes Van Es. “Metal Additive Manufacturing of a High-pressure Micro-pump”. In: *Procedia CIRP* 7 (2013), pp. 252–257. ISSN: 22128271. DOI: `10.1016/j.procir.2013.05.043`. URL: `https://linkinghub.elsevier.com/retrieve/pii/S2212827113002503` (visited on 11/23/2023).

[74] Anthony K. Au et al. “3D□Printed Microfluidics”. In: *Angewandte Chemie International Edition* 55.12 (Mar. 14, 2016), pp. 3862–3881. ISSN: 1433-7851, 1521-3773. DOI: `10.1002/anie.201504382`. URL: `https://onlinelibrary.wiley.com/doi/10.1002/anie.201504382` (visited on 03/05/2024).

[75] Nirveek Bhattacharjee et al. “The upcoming 3D-printing revolution in microfluidics”. In: *Lab on a Chip* 16.10 (2016). Publisher: Royal Society of Chemistry, pp. 1720–1742. DOI: `10.1039/C6LC00163G`. URL: `https://pubs.rsc.org/en/content/articlelanding/2016/lc/c6lc00163g` (visited on 03/05/2024).

[76] Jingchao Jiang, Xun Xu, and Jonathan Stringer. “Support Structures for Additive Manufacturing: A Review”. In: *Journal of Manufacturing and Materials Processing* 2.4 (Dec. 2018). Number: 4 Publisher: Multidisciplinary Digital Publishing Institute, p. 64. ISSN: 2504-4494. DOI: `10.3390/jmmp2040064`. URL: `https://www.mdpi.com/2504-4494/2/4/64` (visited on 03/05/2024).

A

Additive manufacture of a monolithic micropump

This project starts with a monolithic methodology to fabricate a micropump with a ball valve as a single part using 3D printing. However, this method has been shown to fail due to poor performance in either flow infusion or membrane surface quality. The following section will explain the reasons.

The Prusa SL1S SPEED 3D printer is used to produce parts using Prusament resin (Tough Prusa Orange). The mechanical properties of this resin are shown in table A.1.

Property	**Uncured XY**	**Cured XY**	**Uncured YZ**	**Cured YZ**
Young's modulus (Gpa)	0.6	1.6	0.7	1.2
Tensile strength (Mpa)	24.3	41.6	22.4	28.5

Table A.1: Mechanical properties of Prusament Resin Tough Prusa Orange

A.1. Fabrication challenge in monolithic ball valve

One of the major challenges in monolithic manufacturing is the printing of ball valves. The ball must be a moving part of the ball valve. While 3D printing produces layer-by-layer solidification, it cannot directly produce a floating part. Supports are automatically generated in the slicer software to make the designed model printable. The support generated is related to the printing direction of the model. To find a feasible way to print the sphere, half of a ball valve with a support is attempted. Four support generation methods as well as their print results and descriptions are shown in the table A.2. The ball has a radius of 0.62mm and the cylindrical support has a radius of 0.12mm. One side cylindrical support printed from the channel wall (Method No.3) can be found to be the least supported but printable solution for the ball.

Table A.2: Support generation methods for ball

No.	Method	Printed figure	Description
1	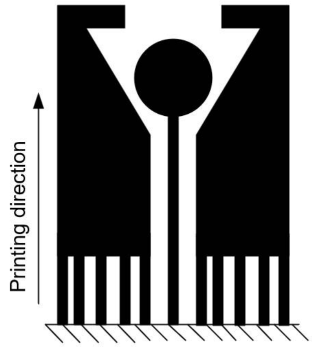	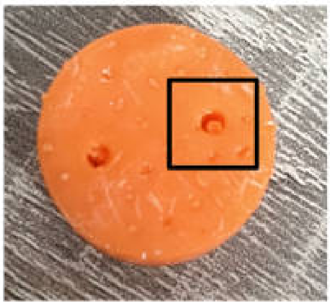	As shown in the circled area, the lower support cracked during removal and could not be removed from the ball.
2	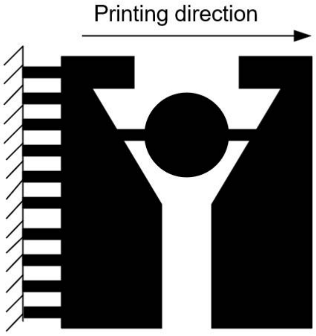	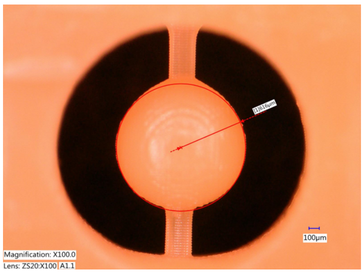	Ball is successfully printed with this type of support. Support is removed with the needle tip.
3	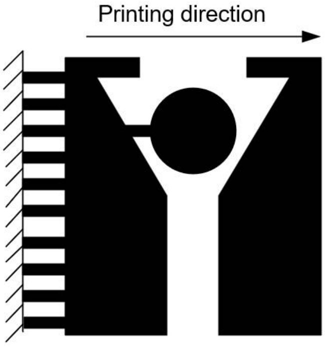	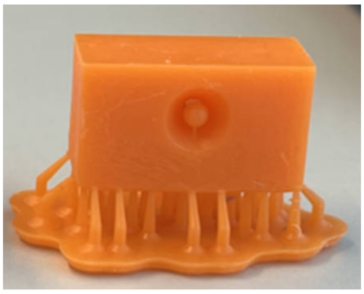	Ball is successfully printed with this type of support. Applying an air pressure of 3200 mbar did not remove the support. Finally, a needle tip is used to remove the support.
4	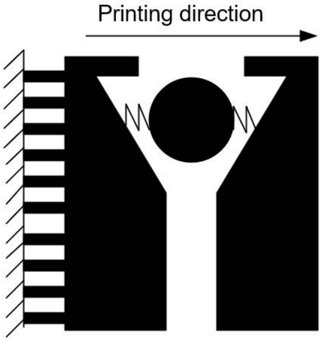		The support is to be printed in the form of a low stiffness spring to allow the ball to move. However, the spring support is not sufficient to support the ball and failed to print the ball inside the channel.

After that, the complete ball valve is printed with a varied ratio between the ball radius and gap radius. The model of the designed ball valve is shown in figure A.1. The ball has a 0.6 mm radius, the channel has a 0. 5mm radius and the varied ratios are 1.5, 2, 3, 4, 5 and 6. After printing is finished, the support is removed by the needle tip.

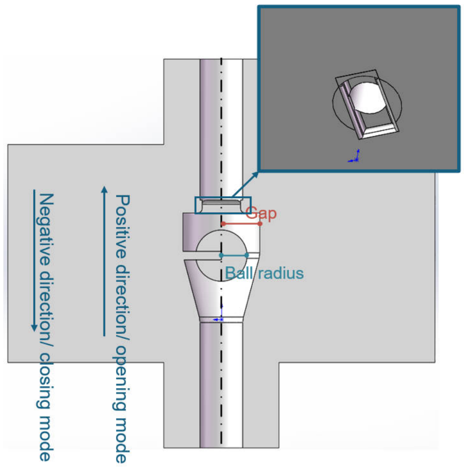

Figure A.1: Cross section view of monolithic ball valve

The schematic diagram of the experiment set up for flow rate measurement is shown in the figure A.2. An external pressure is added to the pressure of the server connected to the inlet of the ball valve and this pressure is controlled by the ELVEFLOW microfluidic flow controller. With applied pressure, water is pumped into the inlet of the ball valve, and its outlet flow rate is measured with a flow sensor. As the flow ranges that can be measured by the ELVEFLOW flow sensors are $\pm 90\mu l/min$, the external valve is added between the ball valve and the flow sensor to proportionally reduce the flow generated to bring it within the measured range.

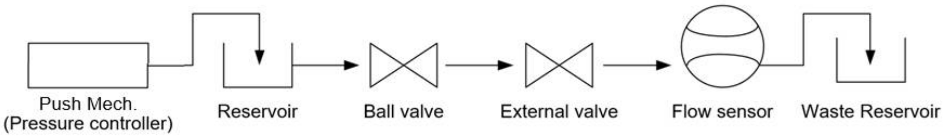

Figure A.2: Schematic diagram of flow measuring experiment set up

The results that were measured are given in the table A.3. In the opening state, the flow rate shows an increase along with the applied pressure in a proportional way. While when it is closing, the flow rate is supposed to drop down rapidly when the ball is in contact with the conical channel wall. However, this reduction trend is not found and there is some unsteadiness in the flow rate. Two possible reasons might cause this phenomenon. First, the broken support inside the channel affects the movement of the ball. Second, since the valve was printed using a material that is not transparent, observing if the ball has been fully detached from the support is not possible. Though transparent resin (Clear Resin V5) can be used in printing, the issue of over-exposure will lead to a ball that does not maintain a round shape.

Table A.3: Measured flow rate of monolithic ball valve with varied ratio

Ratio	Flow rate in opening mode	Flow rate in closing mode
1.5	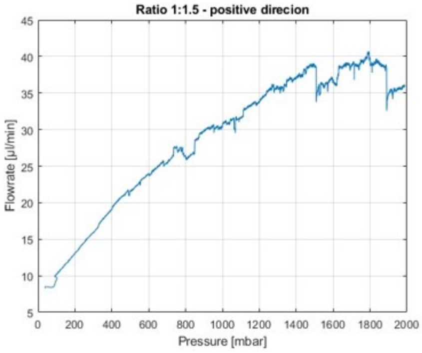	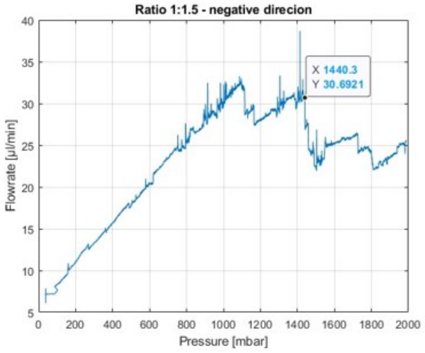
2	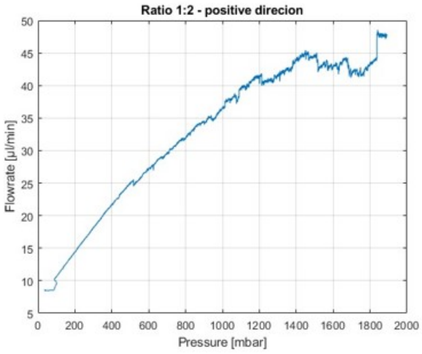	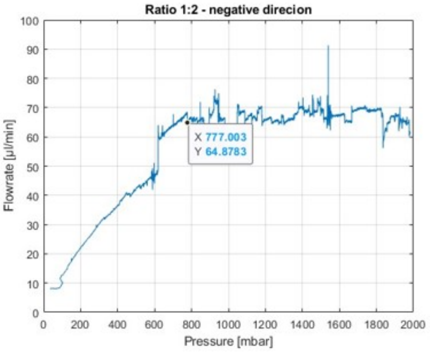
3	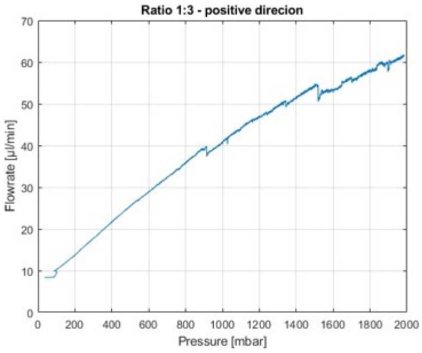	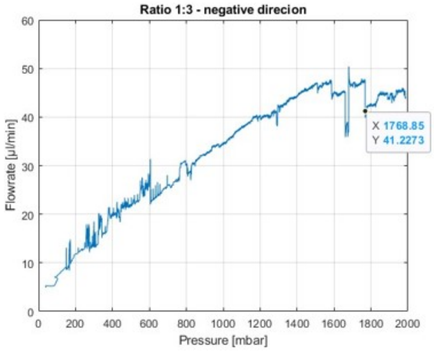
4	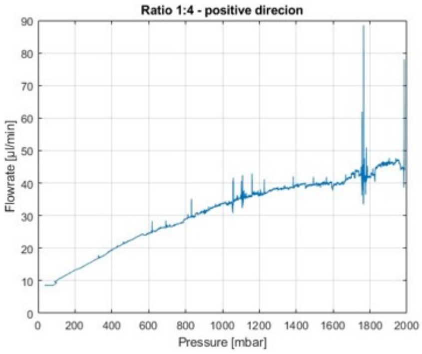	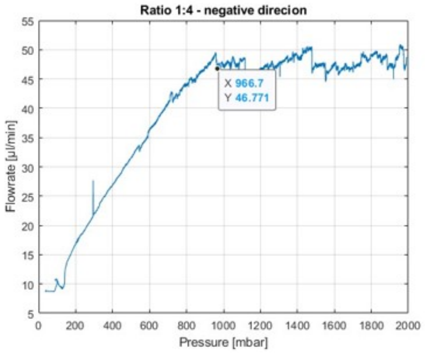

Ratio	Flow rate in opening mode	Flow rate in closing mode
5	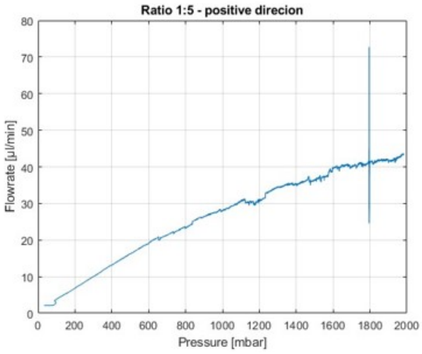	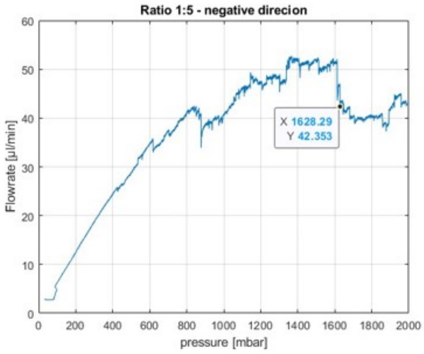

A.2. Fabrication of two-part 3D printed ball valve

Because of the unsatisfactory outcomes, the ball valve is fabricated in two distinct components, as illustrated in figure A.3 (A). Formlabs Clear Resin V5 is used to manufacture the valve body as the transparency makes it easier to observe the movement of the ball. Table A.4 lists its mechanical properties. The assembly of this valve comprises the introduction of a ball into the upper component 1 and the subsequent bonding of this component with the lower component 2 via an epoxy adhesive. The epoxy adhesive layer has a uniform thickness of 73.5 μm as illustrated in figure A.3 (B).

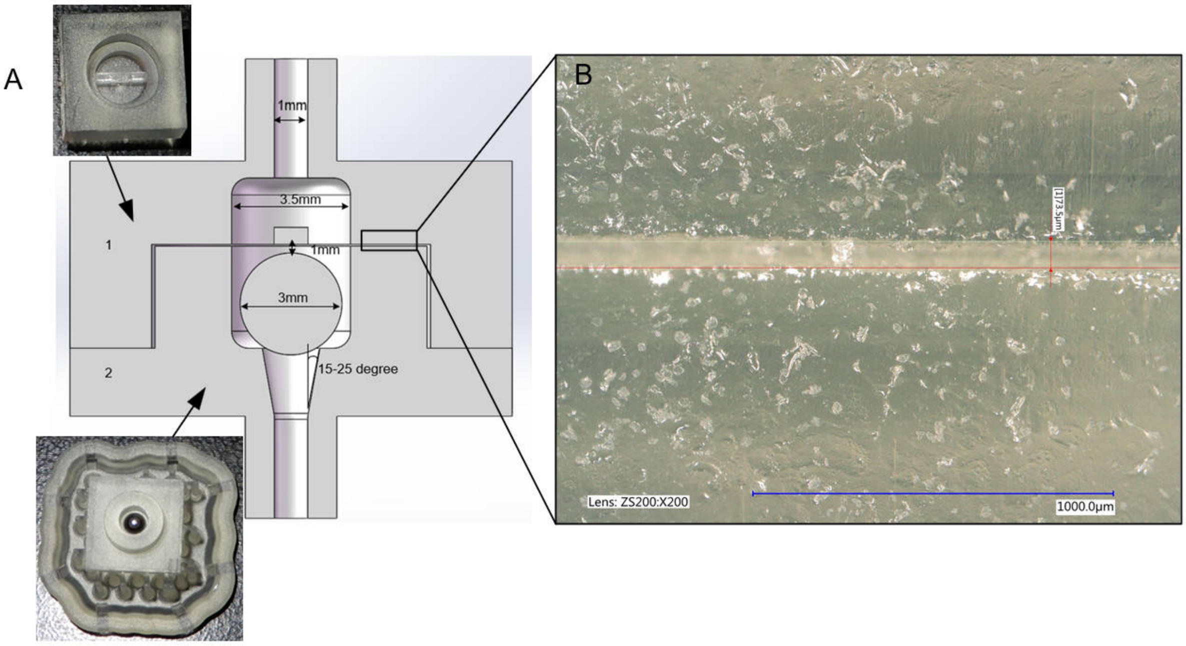

Figure A.3: (A) Cross-section view of a two-part valve and their printed prototypes. (B) The layer of epoxy adhesive under the x200 KEYENCE microscopy

Property	Post-cured at room temperature	Post-cured at $60°C$
Young's modulus (Mpa)	2575	2750
Ultimate tensile strength (Mpa)	51	60

Table A.4: Mechanical properties of Formlabs Clear Resin V5

As the generated flow rate is far from the flow sensor measuring range, the scale is used. Figure A.4 illustrates the schematic diagram for flow sensor measurement. An external pressure is added to the inlet reservoir to pump the fluid into the valve. The scale is used to measure the weight of the fluid in a certain pumping time and by this fluid mass to calculate the flow rate.

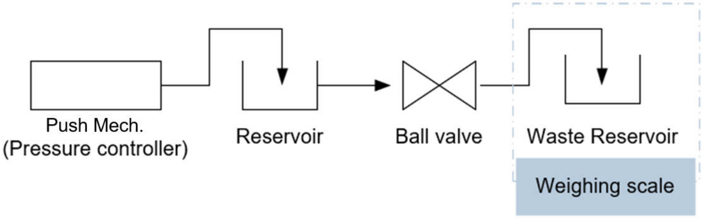

Figure A.4: Schematic diagram of flow measurement

The ball valve is measured with different groove angles and ball materials. Figure A.7 shows the measurement results of the ball valve with different groove shapes and angles. The valve is measured three times at each applied pressure and the error bar shows the sample standard deviation of this repeatability. In opening mode, where the applied pressure is greater than 0 mbar, the flow rate trend is almost the same in different groove types. While in the closing mode, there is a significant difference, where a sharper conical channel results in lower leakage. Although the spherical channel has a similar low leakage as the 10-degree conical groove, it has a higher flow fluctuation between the three tests.

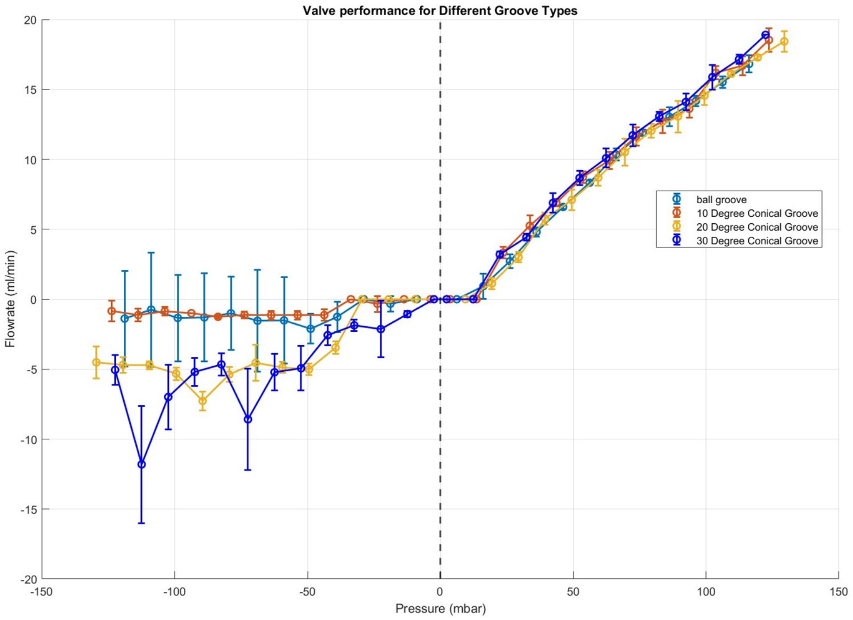

Figure A.5: Flowrate-pressure characterization of valve performance of valves with the different groove types. Error bars indicate the sample standard deviation of three repeated tests at the same applied pressure.

With the known flow rate and applied pressure, the fluid resistance of the valve can be calculated with the equation A.1 where ΔP is a pressure differential, R is the fluid resistance and Q is the flow rate. This fluid resistance includes the resistance caused by the connecting tubing.

$$R = \frac{\Delta P}{Q} \tag{A.1}$$

Due to the laminar flow, the fluid resistance caused by the tubing can be calculated by Poiseuille's law as shown in the equation A.2, where r is the radius of the cylindrical channel, η is the viscosity and L is the channel length. The tubing contributes to $2.925 \times 10^{10} \frac{Pas}{m^3}$ fluid resistance.

$$Q = \frac{\Delta P \pi r^4}{8 \eta L} \tag{A.2}$$

The calculated flow resistances of the ball valve without tubing fluid resistance are listed in the table

	Ball groove	Groove with 10 degree	Groove with 20 degree	Groove with 30 degree
Opening mode fluid resistance ($\frac{Pas}{m^3}$)	8.45×10^9	1.15×10^{10}	9.45×10^9	9.55×10^9
Closing mode fluid resistance ($\frac{Pas}{m^3}$)	3.97×10^{12}	2.58×10^{12}	8.94×10^{11}	6.48×10^{10}

The micropump is also tested for performance with the 3D-printed, steel, and plastic ball. The groove angle for the ball valve in the designed model is 10 degrees. The measured flow rate results are shown in figure A.6 and the calculated fluid resistance without tubing contribution is shown in the table below. Among them, the steel ball performs best as it has the highest flow resistance in the closing mode and the lowest flow resistance in the opening mode. In addition, the flow fluctuation is quite stable in repeatability. Meanwhile, the 3D-printed ball has the worst behavior. It has a high flow fluctuation in closing mode and its flow resistance ratio in closing and opening mode is only 4.81. This may be because the 3D-printed ball is detached from the support and has low sphericity at that detached position. The performance of the polystyrene plastic ball is in between. In opening mode, its flow resistance is close to the 3D printed ball as 1.86×10^{10} and the ratio between the flow resistance in closing and opening mode is 7.9. Due to the effect of gravity, the valve is set in a vertical direction and changes direction during the mode change. Therefore, the above-measured results get rid of the pressure above result eliminate the need for additional force to move the ball to the closed or open position due to its gravity. These three types of balls are also measured to investigate their opening pressure. The opening pressure for the 3D printed ball and the plastic ball are both as low as 50 mbar and 40 mbar respectively. While the required opening pressure for steel ball is above the pressure generation range of 3000 mbar.

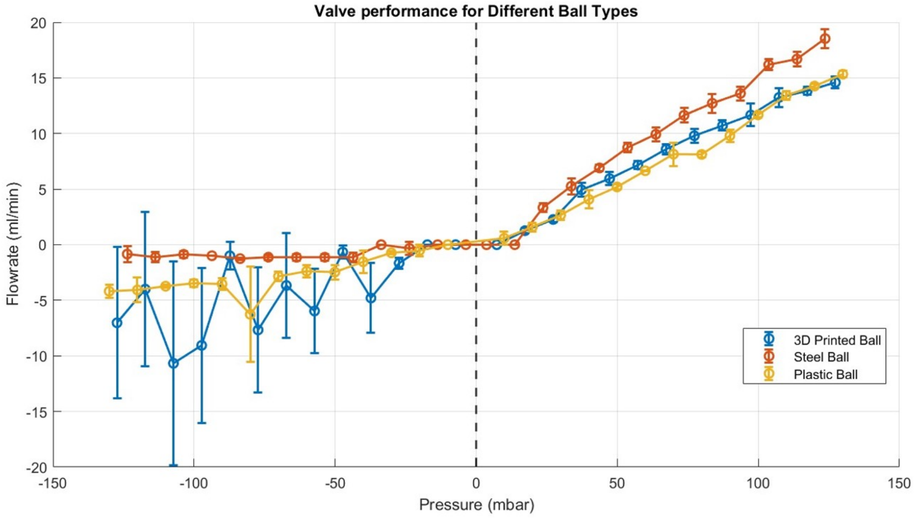

Figure A.6: Flowrate-pressure characterization of valve performance of different ball types. Error bars indicate the sample standard deviation of three repeated tests at the same applied pressure.

	3D printed ball	Steel ball	Plastic ball
Opening mode fluid resistance ($\frac{Pas}{m^3}$)	1.99×10^{10}	1.15×10^{10}	1.86×10^{10}
Closing mode fluid resistance ($\frac{Pas}{m^3}$)	9.58×10^{10}	2.58×10^{12}	1.47×10^{11}

Table A.5: Valve performance of different ball types

A.3. 3D printed membrane

Another problem with a monolithic micropump is the low surface roughness of a printed membrane. As shown in figure A.7, there is a noticeable unevenness at the bottom edge of the membrane. This problem occurs when the printed membrane has a radius greater than 15mm and results in poor contraction between the piezoelectric actuator and the membrane, as the piezoelectric actuator will be bonded to the top of the membrane. In addition, the uncured resin in the chamber is difficult to clean.

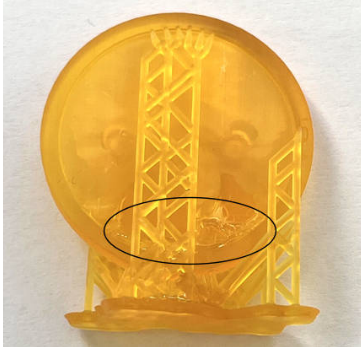

Figure A.7: Schematic diagram of flow measurement

A.4. Conclusion

In conclusion, due to the low unidirectional performance of the 3D printed valve and the surface roughness of the 3D printed membrane, the proposal of monolithic 3D printed micropump is finally chosen. The 3D-printed diaphragm and ball are replaced by a brass diaphragm and polystyrene plastic ball in the micropump prototype.

B

Supplementary Material

The supplementary material discussed the following topics.

1. Fabrication process
2. Flow rate - frequency characterization of prototype 1 and prototype 4
3. Raw data of flow rate measured with prototype 3 micropump concerning frequency, voltage, and backpressure
4. Matlab code for equivalent RLC model analysis
5. Simulation results of piezoelectric actuator central displacement in COMSOL Multiphysics

B.0.1. Fabrication process

Step No.	Image	Description
1	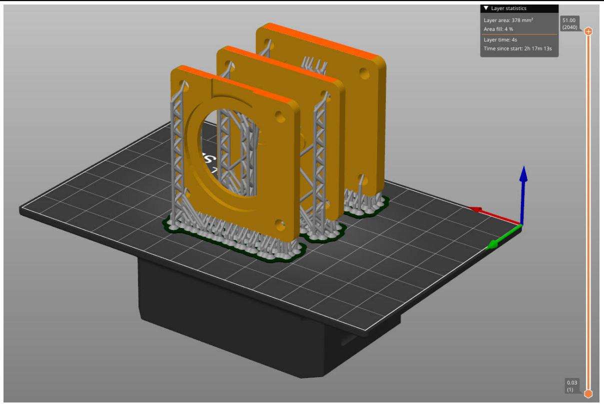 Layer statistics Layer area: 378 mm² Area fill: 4 % Layer time: 4s Time since start: 2h 17m 13s 51.00 (2040) 0.03 (1)	The designed model is saved as an .STL file in SolidWorks then opened in the PrusaSlicer software. The support on the build plate is automatically generated in the software to ensure the model is printable. As shown in this figure, the grey part is the support and the orange part is the designed model. After that, the model is sliced in the software and exported as a .sl1s file.

2		Upload this .sl1s file to the Original Prusa SL1S SPEED 3D Printer. Fill the tank with Prusament Resin tough transparent amber. Then start printing. Wait about 2 hours, the successfully printed parts are shown as white circles in the picture. (Here I printed both the micropump part and the other stuff).
3	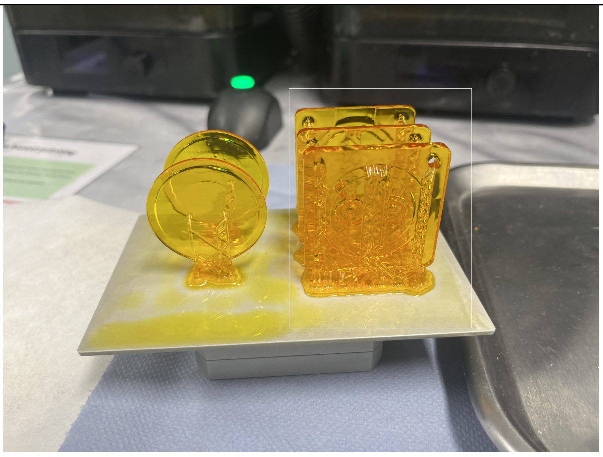	As shown in the figure, the printed parts are stuck to the print head. The printed parts are then removed from the print head.
4		Place the printed parts in the Form Wash for 10 minutes to clean the uncured resin. The Form Wash is filled with IPA.

5		Blow away the liquid on the 3D printed parts with an air gun.
6	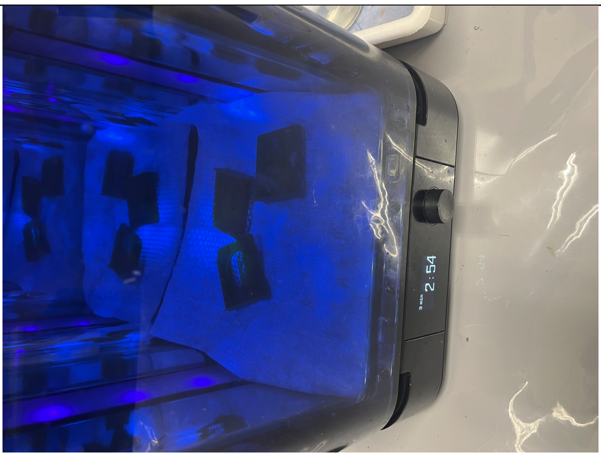	Place 3D printed parts in Form Cure and cure for 15 minutes using UV light.
7	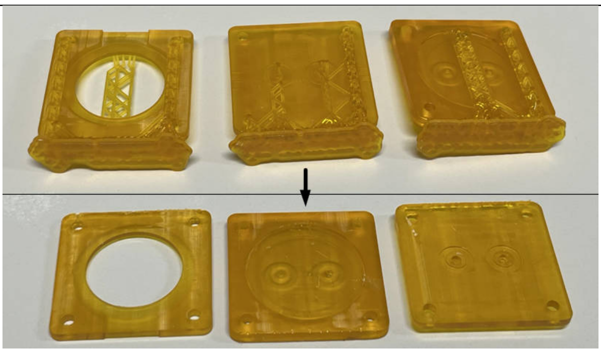	Removed supports from 3D printed parts.
8	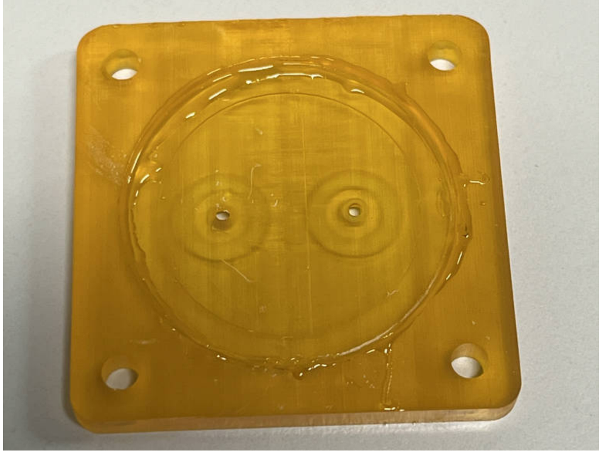	Apply epoxy to the outer edge of the chamber. Be careful not to add epoxy inside the chamber.

9	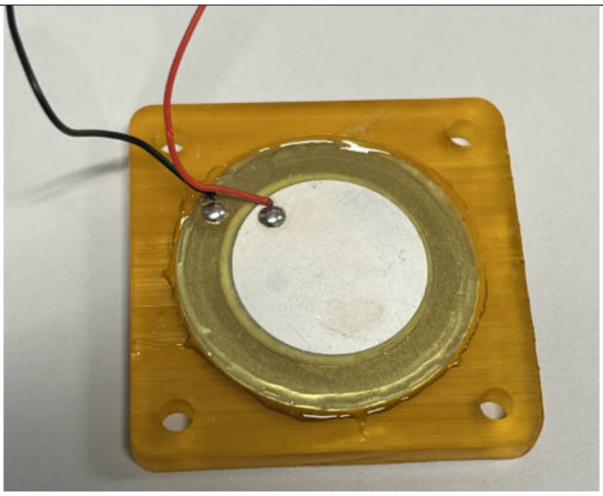	Glue the piezoelectric actuator to the top of the chamber and add epoxy adhesive to the joints.
10	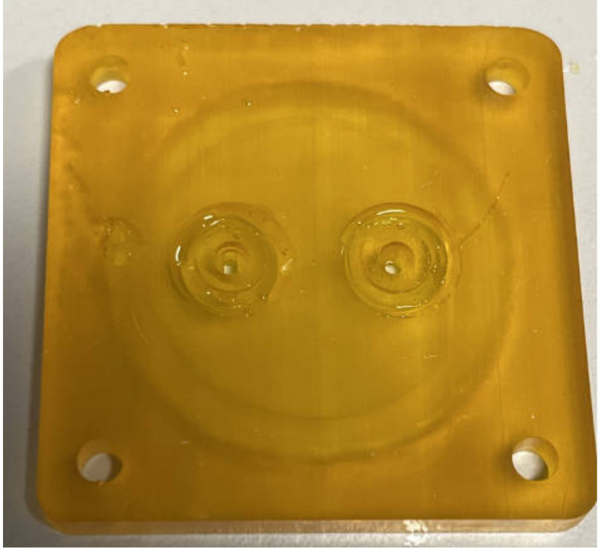	Add epoxy adhesive into the cavity around the conical channel of the pump base and pump chamber. Be careful not to add epoxy to the channel.
11	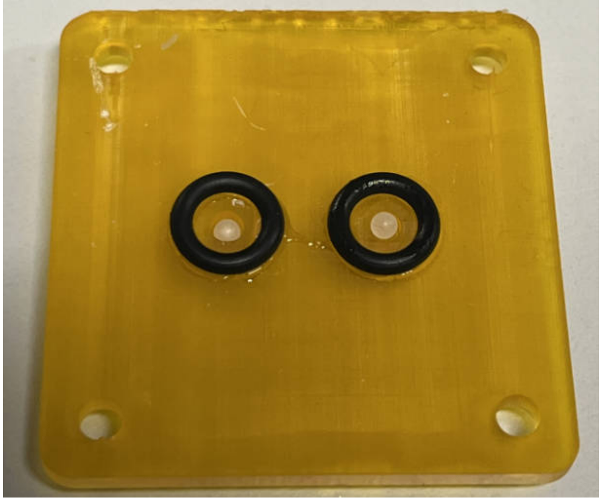	Place polypropylene balls in the tapered channels and two 10mm O-rings on top of the cavity around the channels.

12	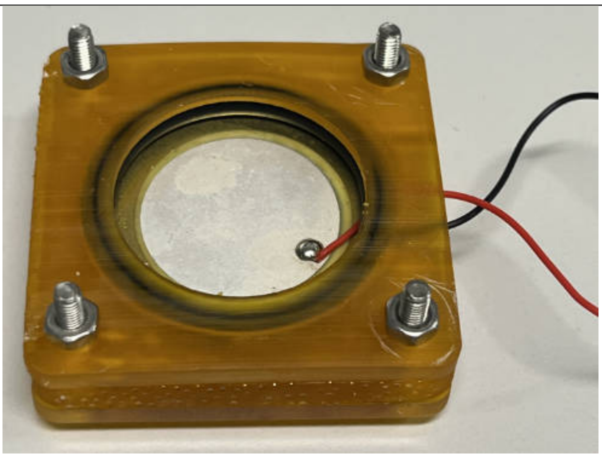	Place a 35mm O-ring on top of the brass diaphragm, then insert four M3 screws into the through holes and use nuts to clamp the three 3D printed layers together.

Table B.1: Fabrication process steps

B.0.2. Flow rate - frequency characterization of rest prototypes

Prototype No.	Image
1	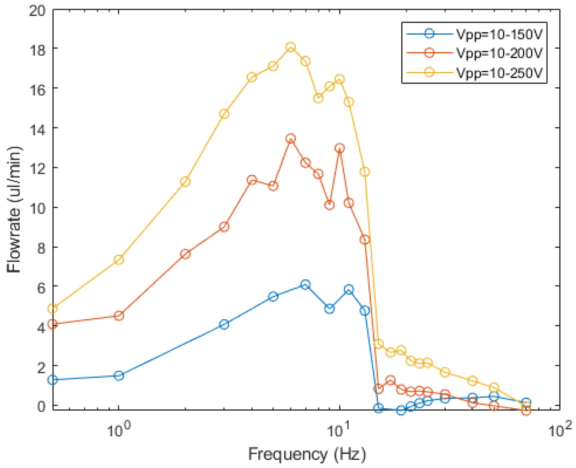
4	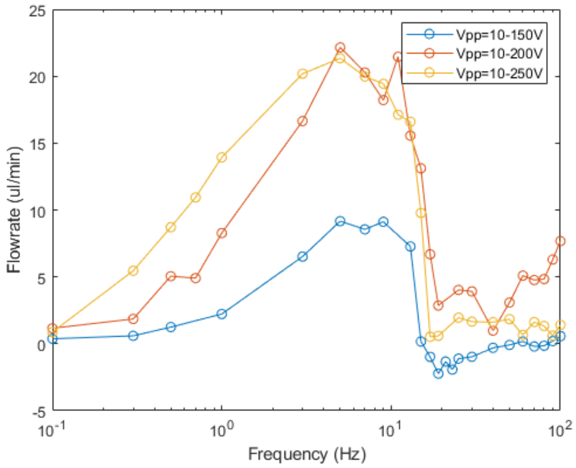

B.0.3. Raw data of flow rate measured with micropump prototype 3

Flow rate - frequency characterization

The following results were measured with 140Vpp voltage applied. An overshoot is observed at the beginning of the flow rate at t_0. This occurs because the voltage applied at time t_0 sometimes reaches the maximum or close to the maximum of the sinusoidal voltage. This voltage induces a high vertical displacement and a large fluid volume change ΔV. Since the time change at that moment Δt is infinitesimal, and the flow rate $Q = \frac{\Delta V}{\Delta t}$, the resulting flow rate becomes extremely large.

Frequency	Image
0.1	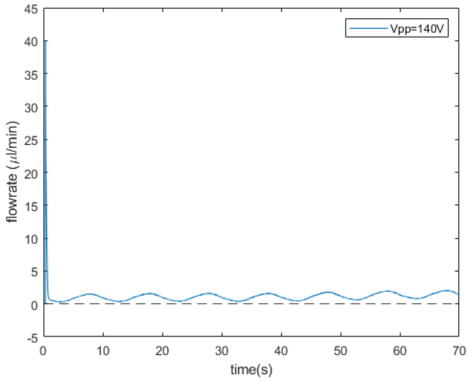
0.3	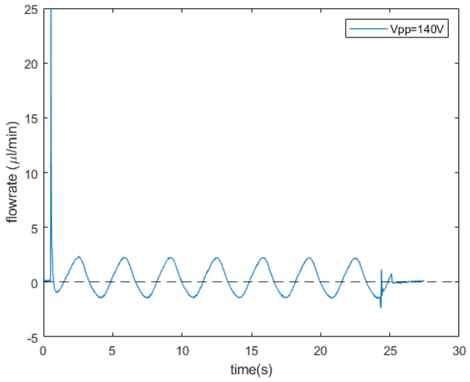
0.5	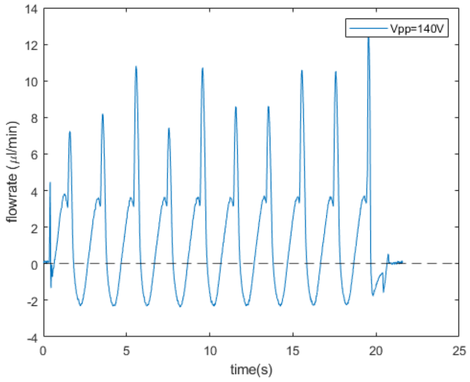

0.7	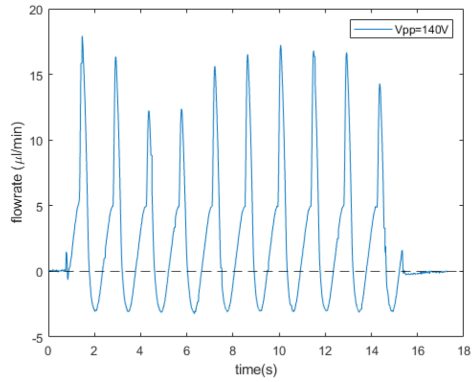Vpp=140V flowrate (μl/min) time(s) 20 15 10 5 0 -5 0 2 4 6 8 10 12 14 16 18
0.9	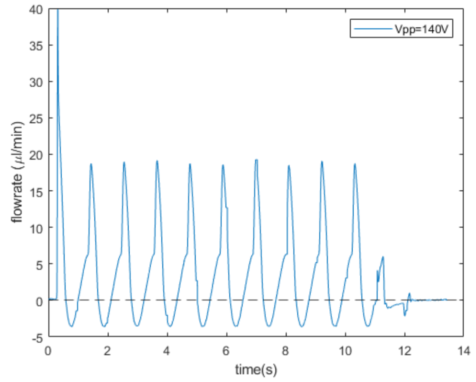Vpp=140V flowrate (μl/min) time(s) 40 35 30 25 20 15 10 5 0 -5 0 2 4 6 8 10 12 14
1	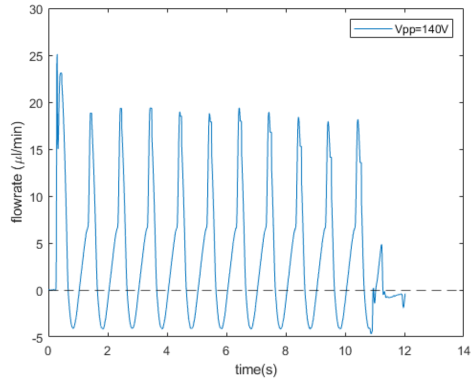Vpp=140V flowrate (μl/min) time(s) 30 25 20 15 10 5 0 -5 0 2 4 6 8 10 12 14
2	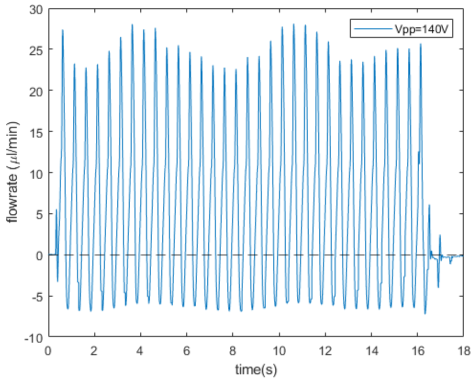Vpp=140V flowrate (μl/min) time(s) 30 25 20 15 10 5 0 -5 -10 0 2 4 6 8 10 12 14 16 18

3	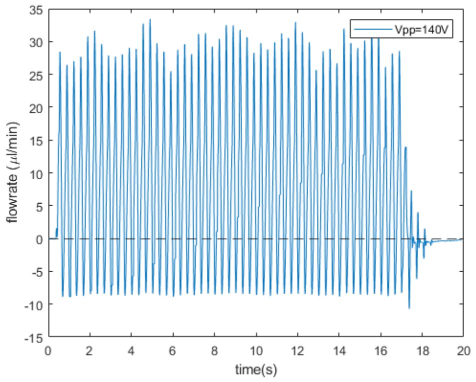Vpp=140V flowrate (μl/min) time(s) 35 30 25 20 15 10 5 0 -5 -10 -15 0 2 4 6 8 10 12 14 16 18 20
4	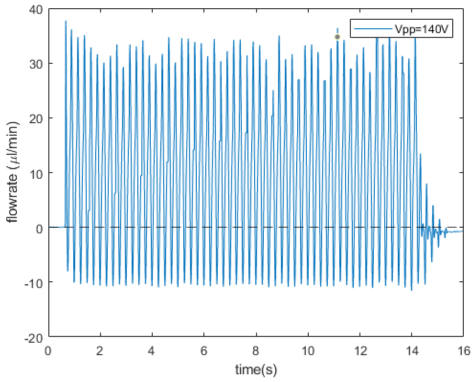Vpp=140V flowrate (μl/min) time(s) 40 30 20 10 0 -10 -20 0 2 4 6 8 10 12 14 16
5	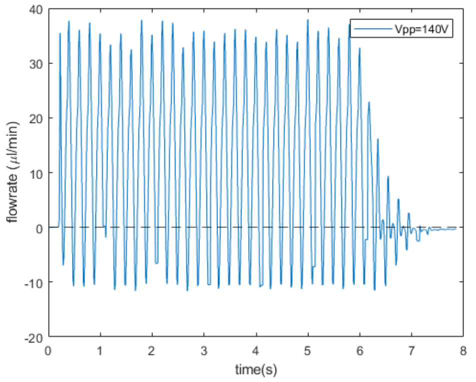Vpp=140V flowrate (μl/min) time(s) 40 30 20 10 0 -10 -20 0 1 2 3 4 5 6 7 8
6	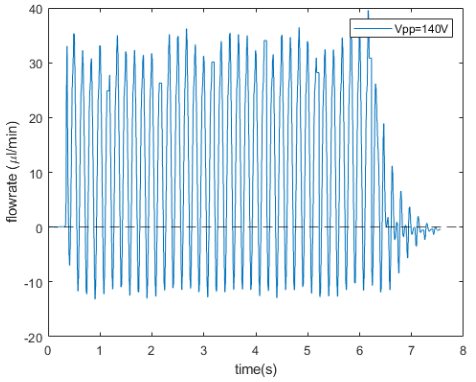Vpp=140V flowrate (μl/min) time(s) 40 30 20 10 0 -10 -20 0 1 2 3 4 5 6 7 8

<table>
<tr><td>7</td><td>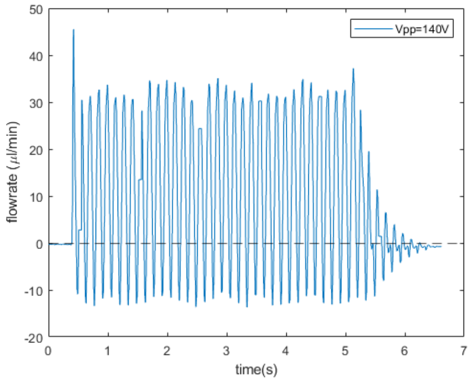
Vpp=140V
flowrate (μl/min)
time(s)
50
40
30
20
10
0
-10
-20
0
1
2
3
4
5
6
7</td></tr>
<tr><td>8</td><td>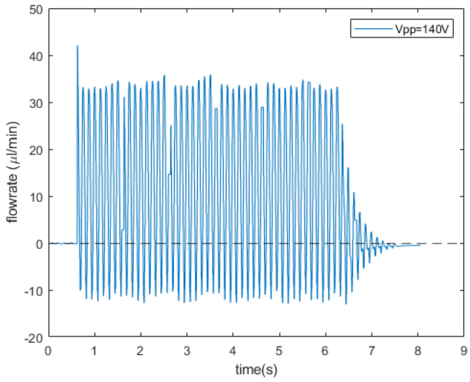
Vpp=140V
flowrate (μl/min)
time(s)
50
40
30
20
10
0
-10
-20
0
1
2
3
4
5
6
7
8
9</td></tr>
<tr><td>9</td><td>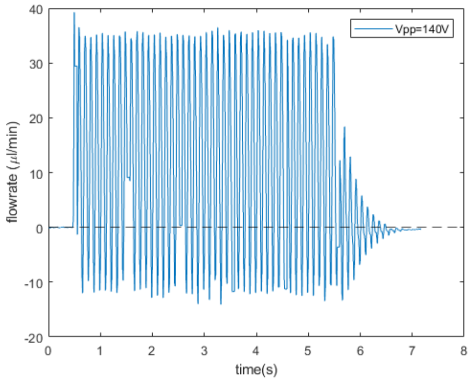
Vpp=140V
flowrate (μl/min)
time(s)
40
30
20
10
0
-10
-20
0
1
2
3
4
5
6
7
8</td></tr>
<tr><td>10</td><td>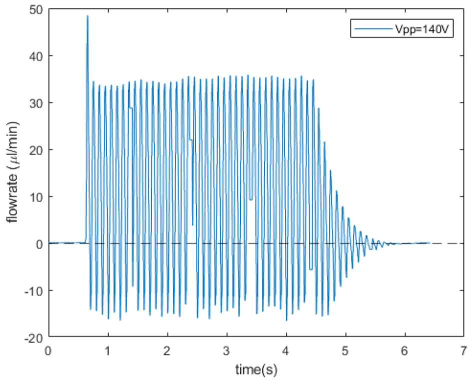
Vpp=140V
flowrate (μl/min)
time(s)
50
40
30
20
10
0
-10
-20
0
1
2
3
4
5
6
7</td></tr>
</table>

11	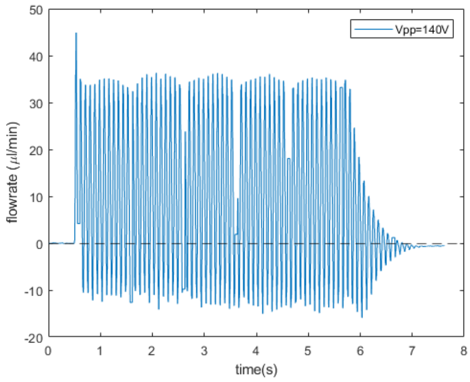Vpp=140V flowrate (μl/min) time(s) 50 40 30 20 10 0 -10 -20 0 1 2 3 4 5 6 7 8
12	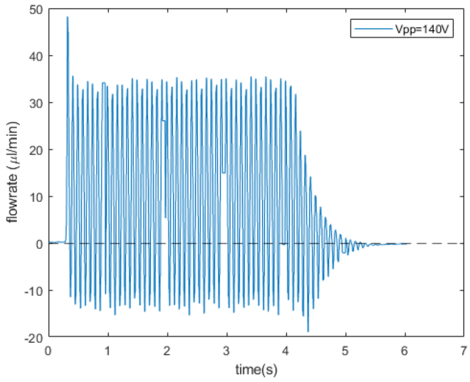Vpp=140V flowrate (μl/min) time(s) 50 40 30 20 10 0 -10 -20 0 1 2 3 4 5 6 7
13	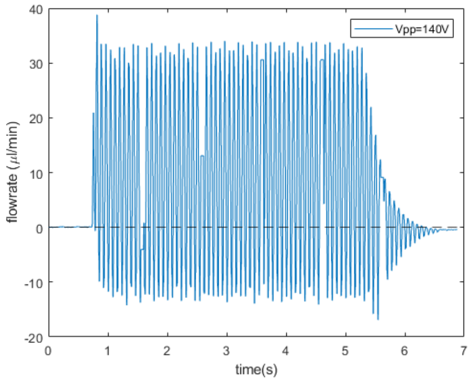Vpp=140V flowrate (μl/min) time(s) 40 30 20 10 0 -10 -20 0 1 2 3 4 5 6 7
14	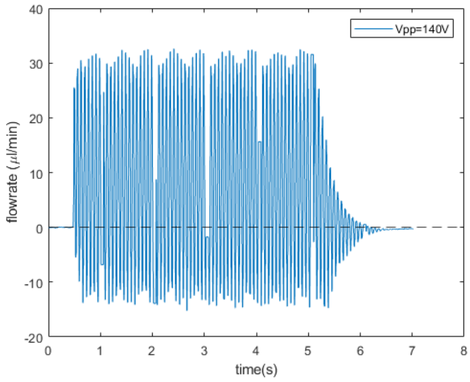Vpp=140V flowrate (μl/min) time(s) 40 30 20 10 0 -10 -20 0 1 2 3 4 5 6 7 8

15	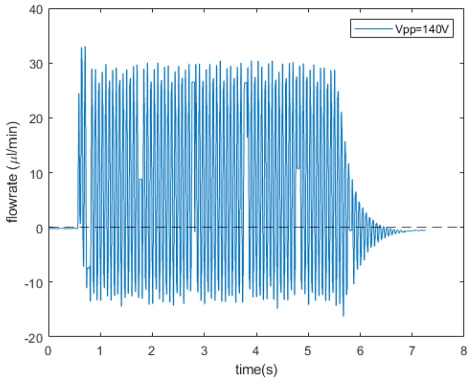Vpp=140V flowrate (μl/min) 40 30 20 10 0 -10 -20 0 1 2 3 4 5 6 7 8 time(s)
17	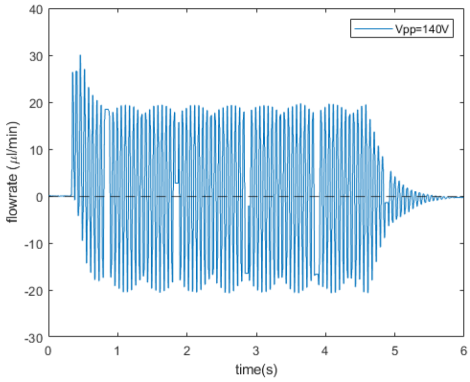Vpp=140V flowrate (μl/min) 40 30 20 10 0 -10 -20 -30 0 1 2 3 4 5 6 time(s)
18	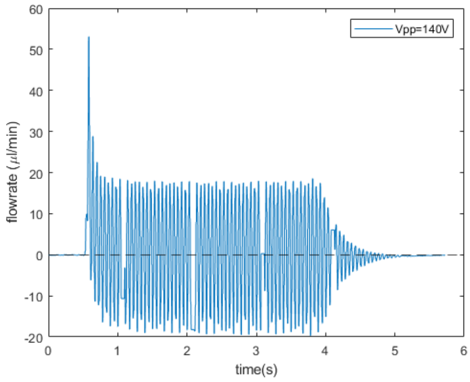Vpp=140V flowrate (μl/min) 60 50 40 30 20 10 0 -10 -20 0 1 2 3 4 5 6 time(s)
19	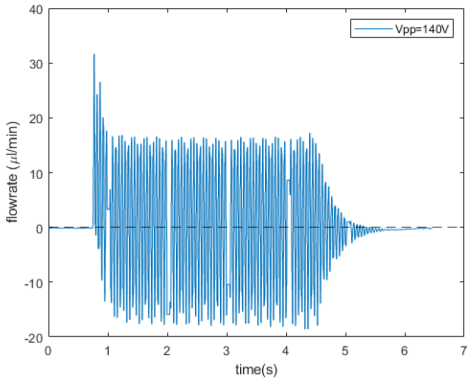Vpp=140V flowrate (μl/min) 40 30 20 10 0 -10 -20 0 1 2 3 4 5 6 7 time(s)

20	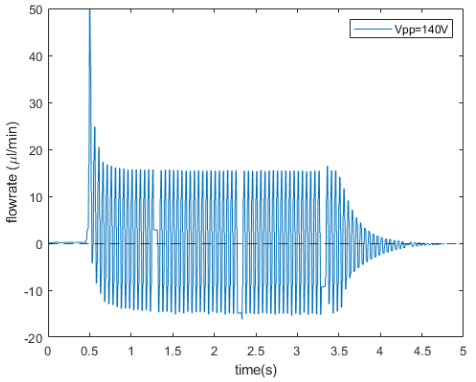Vpp=140V flowrate (μl/min) time(s) 50 40 30 20 10 0 -10 -20 0 0.5 1 1.5 2 2.5 3 3.5 4 4.5 5
22	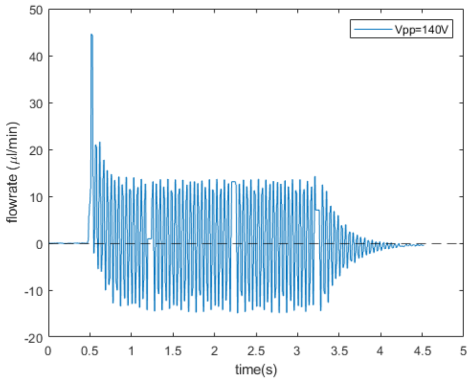Vpp=140V flowrate (μl/min) time(s) 50 40 30 20 10 0 -10 -20 0 0.5 1 1.5 2 2.5 3 3.5 4 4.5 5
24	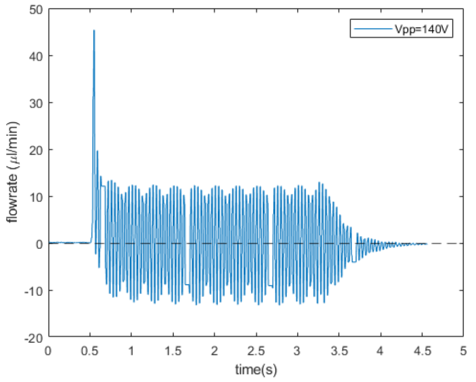Vpp=140V flowrate (μl/min) time(s) 50 40 30 20 10 0 -10 -20 0 0.5 1 1.5 2 2.5 3 3.5 4 4.5 5
25	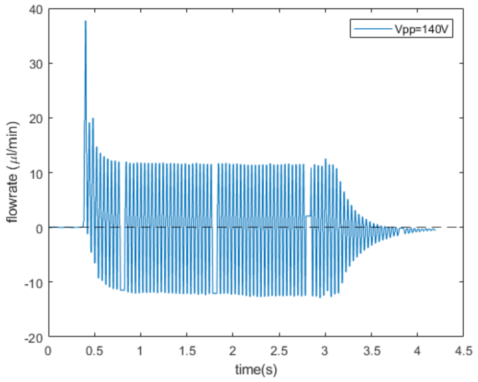Vpp=140V flowrate (μl/min) time(s) 40 30 20 10 0 -10 -20 0 0.5 1 1.5 2 2.5 3 3.5 4 4.5

30	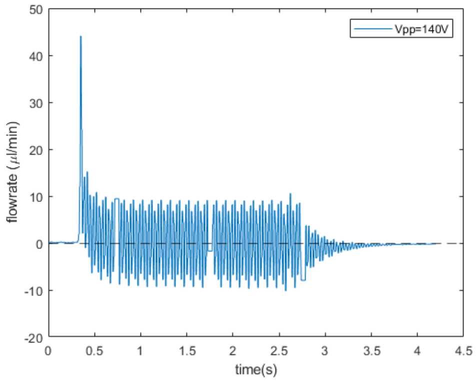 Vpp=140V flowrate (μl/min) time(s) 50 40 30 20 10 0 -10 -20 0 0.5 1 1.5 2 2.5 3 3.5 4 4.5
40	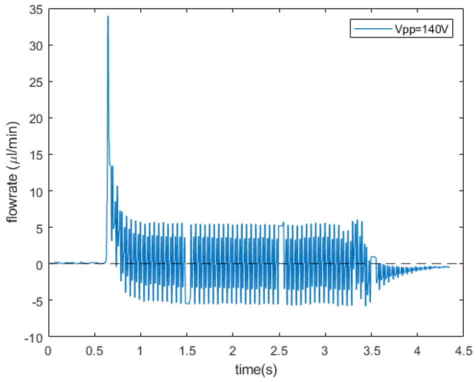 Vpp=140V flowrate (μl/min) time(s) 35 30 25 20 15 10 5 0 -5 -10 0 0.5 1 1.5 2 2.5 3 3.5 4 4.5
50	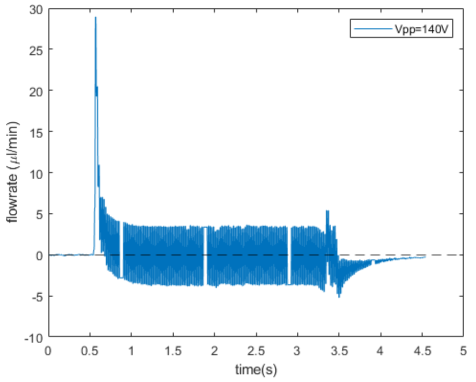 Vpp=140V flowrate (μl/min) time(s) 30 25 20 15 10 5 0 -5 -10 0 0.5 1 1.5 2 2.5 3 3.5 4 4.5 5
60	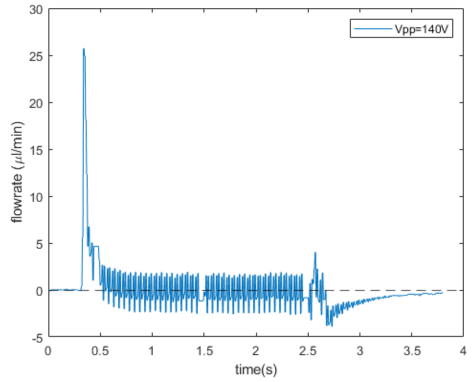 Vpp=140V flowrate (μl/min) time(s) 30 25 20 15 10 5 0 -5 0 0.5 1 1.5 2 2.5 3 3.5 4

<table>
<tr><td>70</td><td>
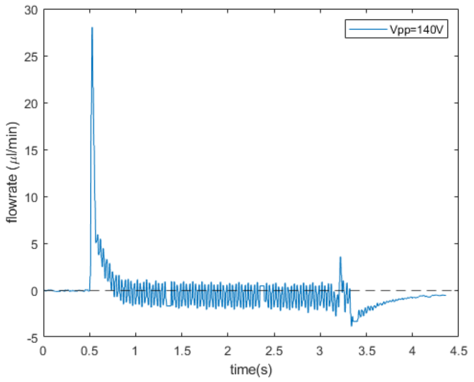
Vpp=140V
flowrate (μl/min)
time(s)
30
25
20
15
10
5
0
-5
0
0.5
1
1.5
2
2.5
3
3.5
4
4.5
</td></tr>
<tr><td>80</td><td>
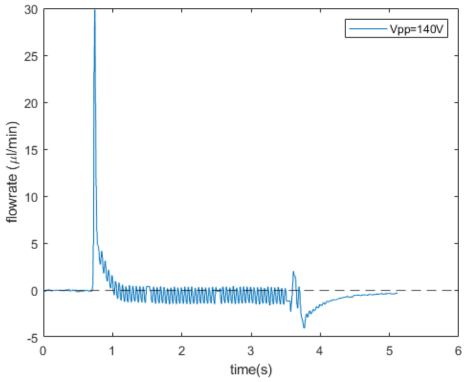
Vpp=140V
flowrate (μl/min)
time(s)
30
25
20
15
10
5
0
-5
0
1
2
3
4
5
6
</td></tr>
<tr><td>90</td><td>
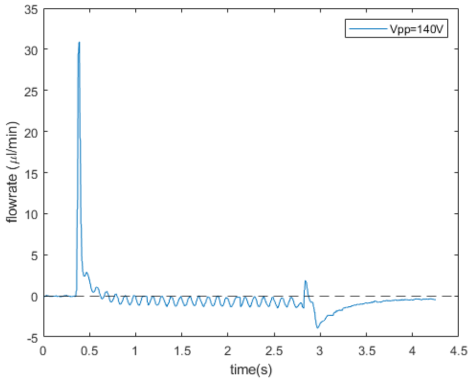
Vpp=140V
flowrate (μl/min)
time(s)
35
30
25
20
15
10
5
0
-5
0
0.5
1
1.5
2
2.5
3
3.5
4
4.5
</td></tr>
<tr><td>100</td><td>
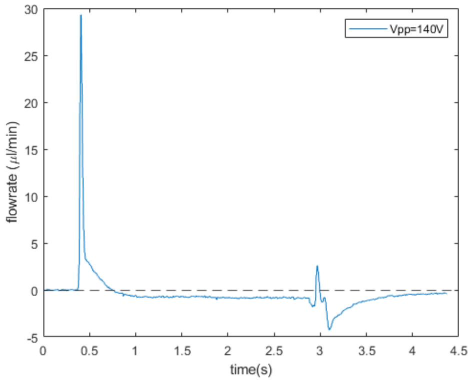
Vpp=140V
flowrate (μl/min)
time(s)
30
25
20
15
10
5
0
-5
0
0.5
1
1.5
2
2.5
3
3.5
4
4.5
</td></tr>
</table>

The following results were measured with 190Vpp voltage applied.

Frequency	Image
0.1	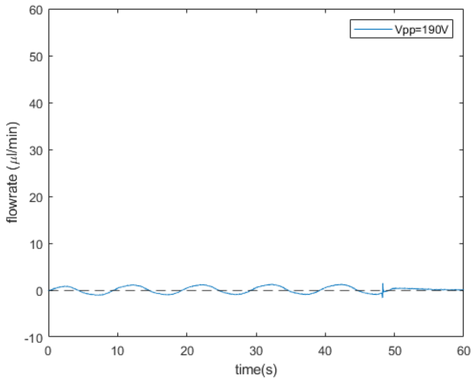
0.5	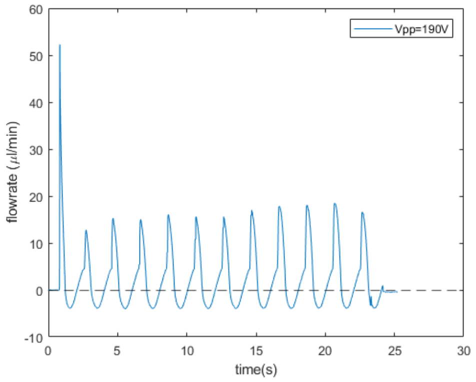
0.7	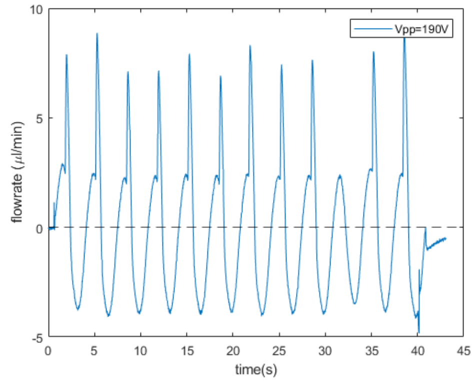
0.9	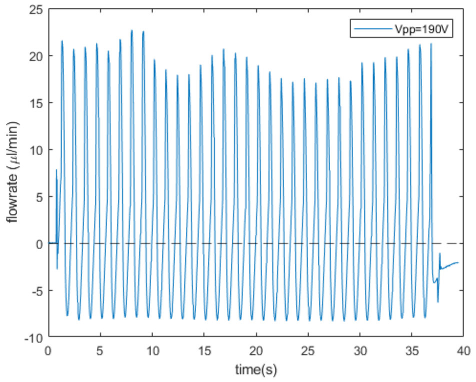

1	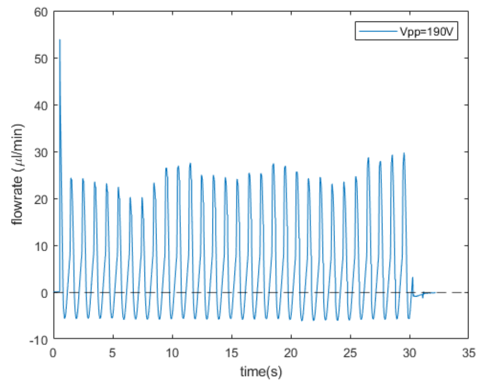Vpp=190V flowrate (μl/min) time(s) 60 50 40 30 20 10 0 -10 0 5 10 15 20 25 30 35
2	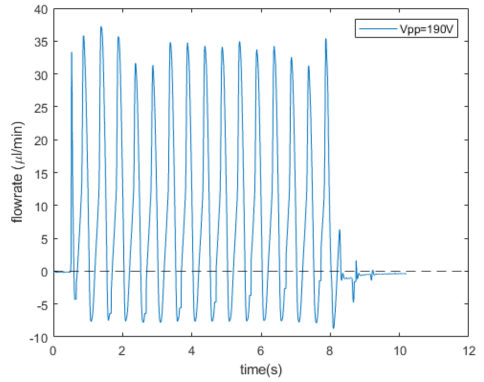Vpp=190V flowrate (μl/min) time(s) 40 35 30 25 20 15 10 5 0 -5 -10 0 2 4 6 8 10 12
3	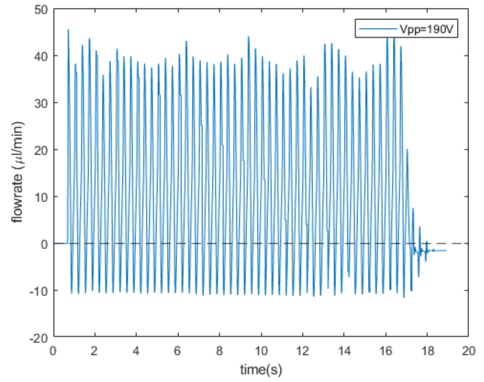Vpp=190V flowrate (μl/min) time(s) 50 40 30 20 10 0 -10 -20 0 2 4 6 8 10 12 14 16 18 20
4	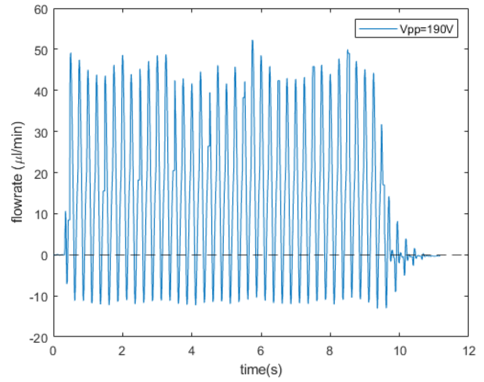Vpp=190V flowrate (μl/min) time(s) 60 50 40 30 20 10 0 -10 -20 0 2 4 6 8 10 12

5	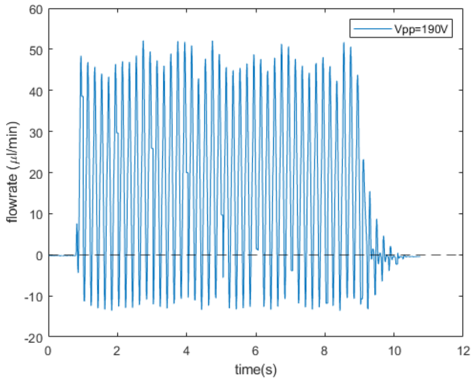Vpp=190V flowrate (μl/min) time(s) 60 50 40 30 20 10 0 -10 -20 0 2 4 6 8 10 12
6	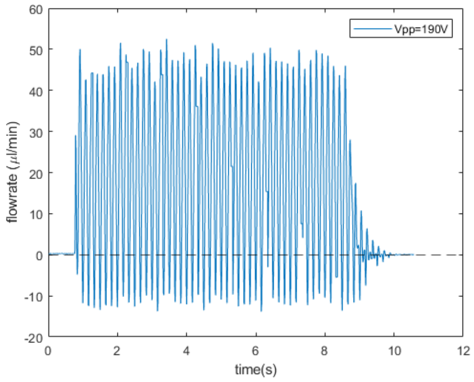Vpp=190V flowrate (μl/min) time(s) 60 50 40 30 20 10 0 -10 -20 0 2 4 6 8 10 12
7	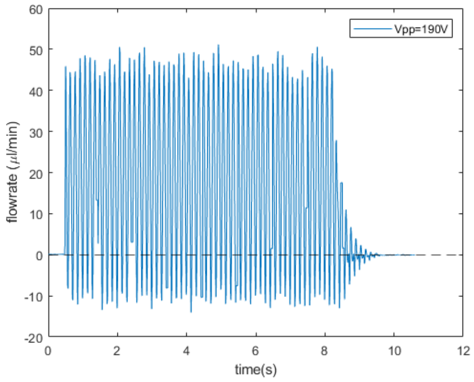Vpp=190V flowrate (μl/min) time(s) 60 50 40 30 20 10 0 -10 -20 0 2 4 6 8 10 12
8	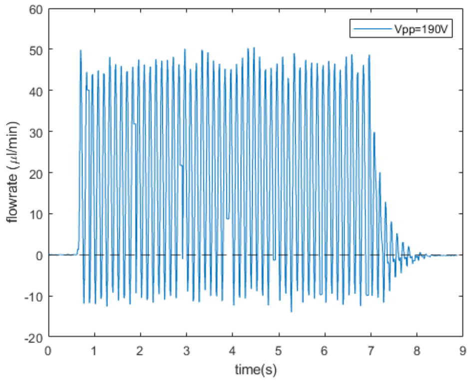Vpp=190V flowrate (μl/min) time(s) 60 50 40 30 20 10 0 -10 -20 0 1 2 3 4 5 6 7 8 9

9	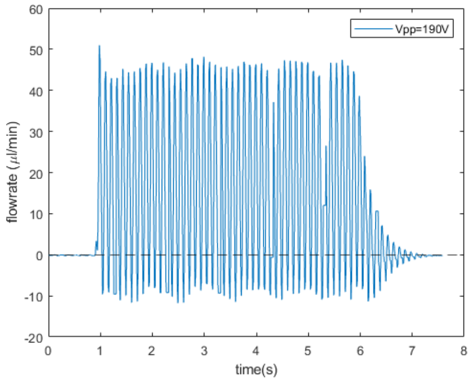Vpp=190V flowrate (μl/min) time(s) 60 50 40 30 20 10 0 -10 -20 0 1 2 3 4 5 6 7 8
10	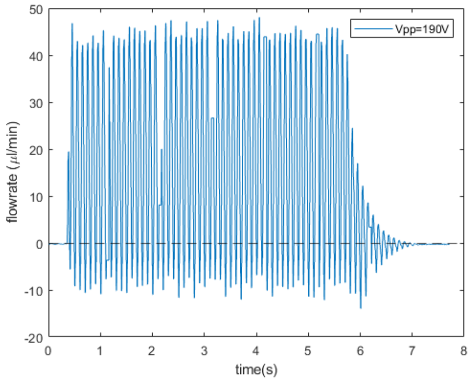Vpp=190V flowrate (μl/min) time(s) 50 40 30 20 10 0 -10 -20 0 1 2 3 4 5 6 7 8
11	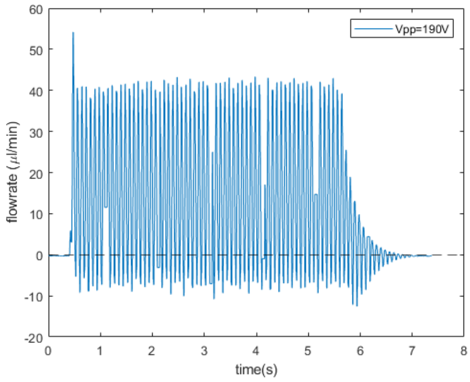Vpp=190V flowrate (μl/min) time(s) 60 50 40 30 20 10 0 -10 -20 0 1 2 3 4 5 6 7 8
13	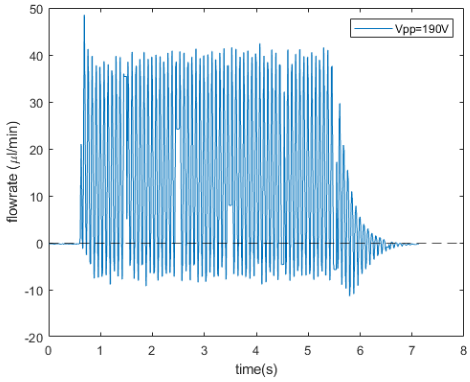Vpp=190V flowrate (μl/min) time(s) 50 40 30 20 10 0 -10 -20 0 1 2 3 4 5 6 7 8

14	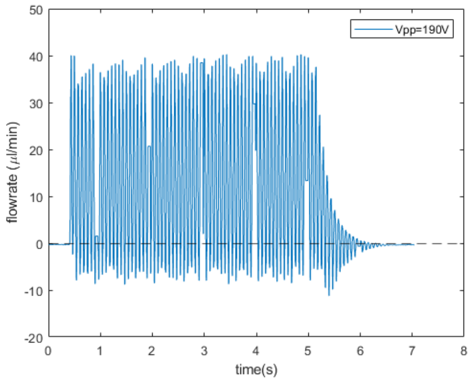Vpp=190V flowrate (μl/min) time(s) 50 40 30 20 10 0 -10 -20 0 1 2 3 4 5 6 7 8
15	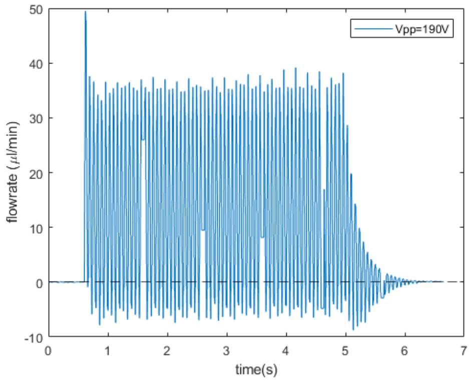Vpp=190V flowrate (μl/min) time(s) 50 40 30 20 10 0 -10 0 1 2 3 4 5 6 7
16	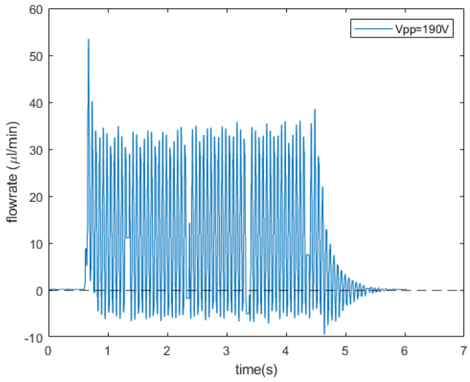Vpp=190V flowrate (μl/min) time(s) 60 50 40 30 20 10 0 -10 0 1 2 3 4 5 6 7
17	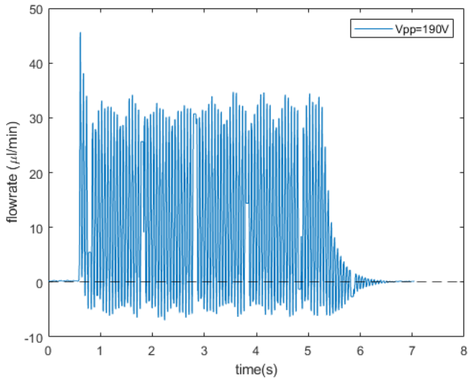Vpp=190V flowrate (μl/min) time(s) 50 40 30 20 10 0 -10 0 1 2 3 4 5 6 7 8

18	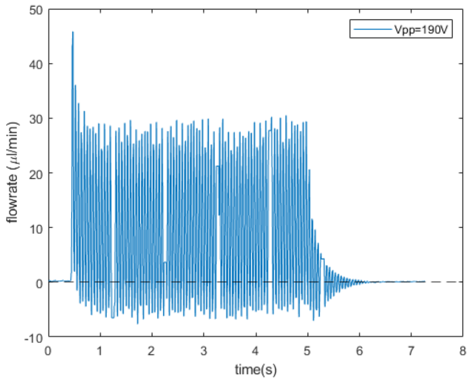Vpp=190V flowrate (μl/min) time(s) 50 40 30 20 10 0 -10 0 1 2 3 4 5 6 7 8
19	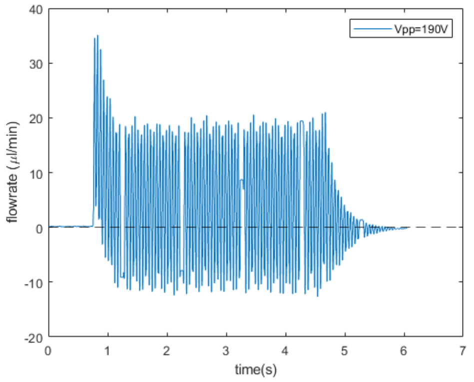Vpp=190V flowrate (μl/min) time(s) 40 30 20 10 0 -10 -20 0 1 2 3 4 5 6 7
20	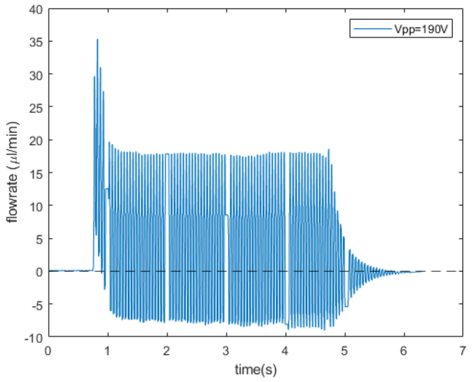Vpp=190V flowrate (μl/min) time(s) 40 35 30 25 20 15 10 5 0 -5 -10 0 1 2 3 4 5 6 7
22	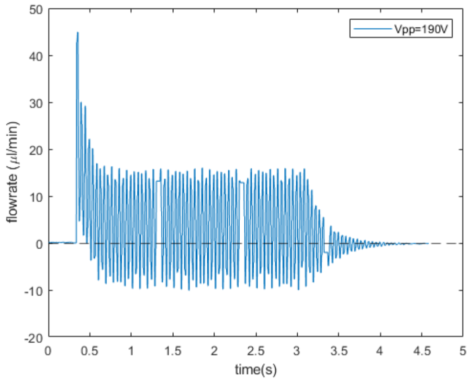Vpp=190V flowrate (μl/min) time(s) 50 40 30 20 10 0 -10 -20 0 0.5 1 1.5 2 2.5 3 3.5 4 4.5 5

24	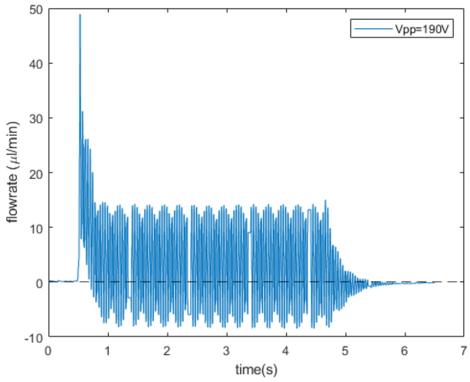flowrate (μl/min) time(s) Vpp=190V 50 40 30 20 10 0 -10 0 1 2 3 4 5 6 7
26	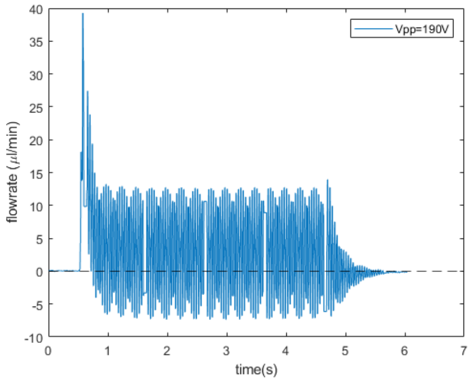flowrate (μl/min) time(s) Vpp=190V 40 35 30 25 20 15 10 5 0 -5 -10 0 1 2 3 4 5 6 7
28	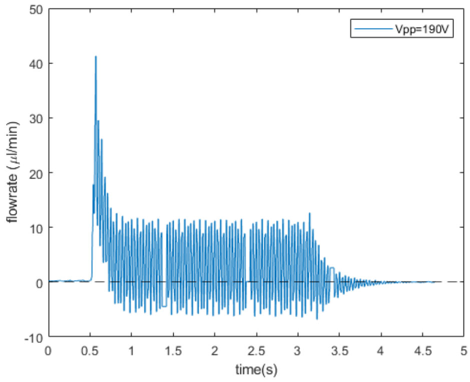flowrate (μl/min) time(s) Vpp=190V 50 40 30 20 10 0 -10 0 0.5 1 1.5 2 2.5 3 3.5 4 4.5 5
30	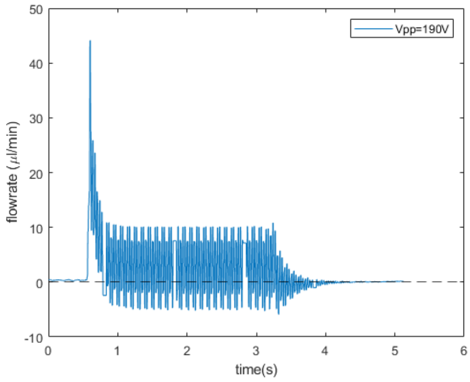flowrate (μl/min) time(s) Vpp=190V 50 40 30 20 10 0 -10 0 1 2 3 4 5 6

35	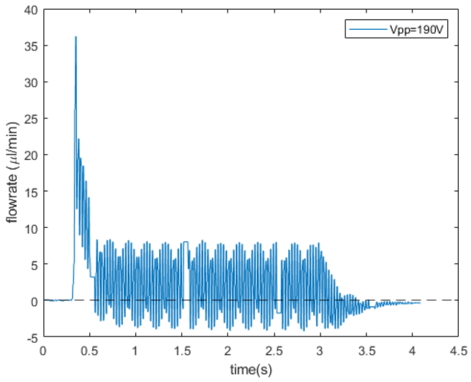Vpp=190V flowrate (μl/min) time(s) 40 35 30 25 20 15 10 5 0 -5 0 0.5 1 1.5 2 2.5 3 3.5 4 4.5
40	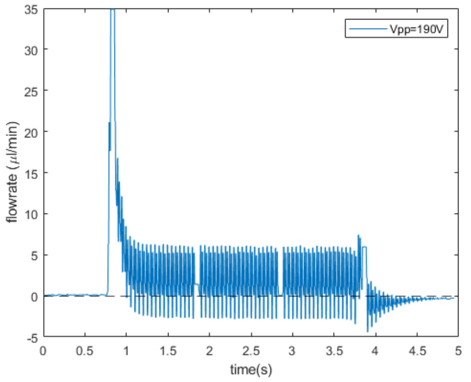Vpp=190V flowrate (μl/min) time(s) 35 30 25 20 15 10 5 0 -5 0 0.5 1 1.5 2 2.5 3 3.5 4 4.5 5
45	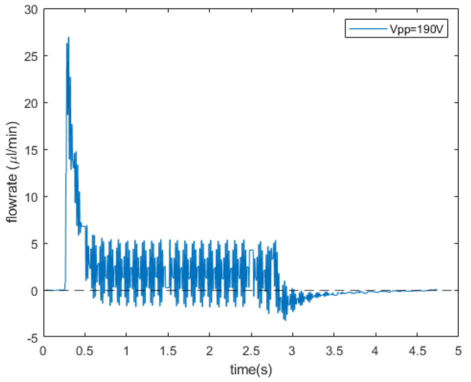Vpp=190V flowrate (μl/min) time(s) 30 25 20 15 10 5 0 -5 0 0.5 1 1.5 2 2.5 3 3.5 4 4.5 5
50	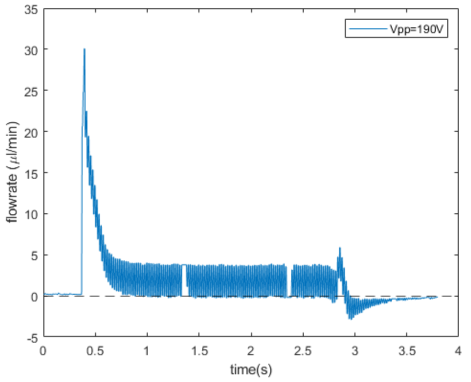Vpp=190V flowrate (μl/min) time(s) 35 30 25 20 15 10 5 0 -5 0 0.5 1 1.5 2 2.5 3 3.5 4

60	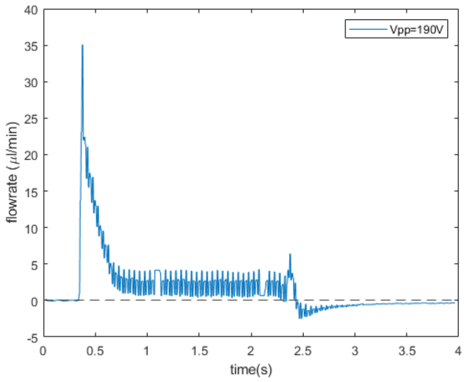Vpp=190V flowrate (μl/min) time(s) 40 35 30 25 20 15 10 5 0 -5 0 0.5 1 1.5 2 2.5 3 3.5 4
70	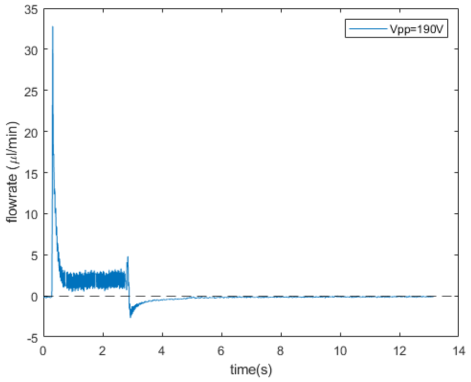Vpp=190V flowrate (μl/min) time(s) 35 30 25 20 15 10 5 0 -5 0 2 4 6 8 10 12 14
80	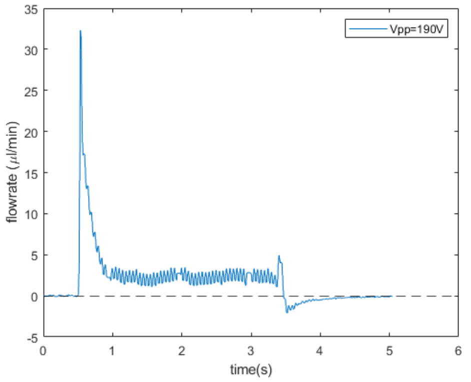Vpp=190V flowrate (μl/min) time(s) 35 30 25 20 15 10 5 0 -5 0 1 2 3 4 5 6
90	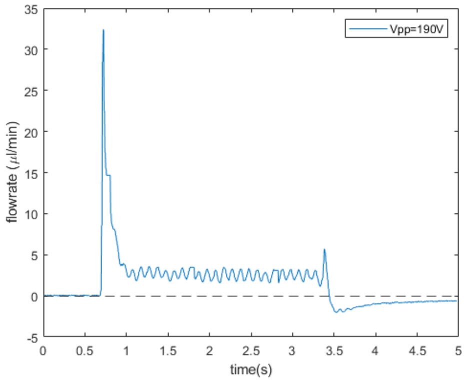Vpp=190V flowrate (μl/min) time(s) 35 30 25 20 15 10 5 0 -5 0 0.5 1 1.5 2 2.5 3 3.5 4 4.5 5

100	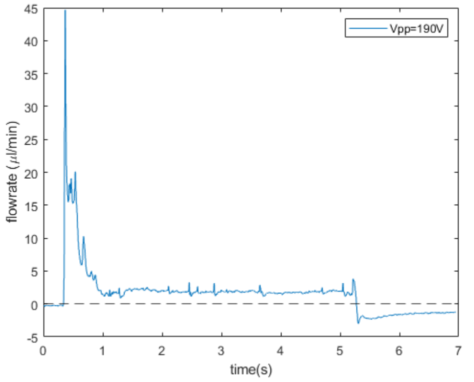

Vpp=190V
flowrate (μl/min)
time(s)
45
40
35
30
25
20
15
10
5
0
-5
0
1
2
3
4
5
6
7

The following results were measured with 240Vpp voltage applied.

Frequency	Image
0.1	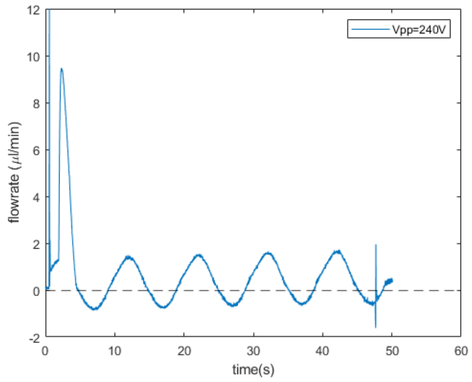
0.3	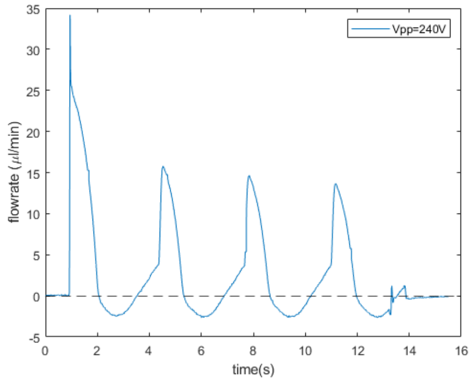
0.5	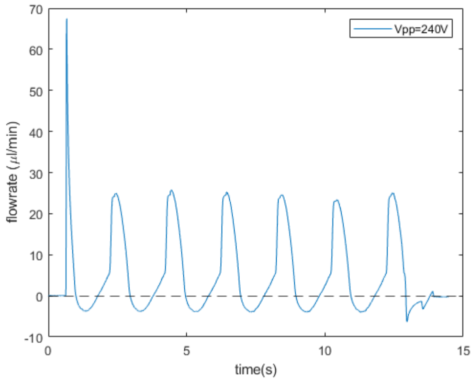
0.7	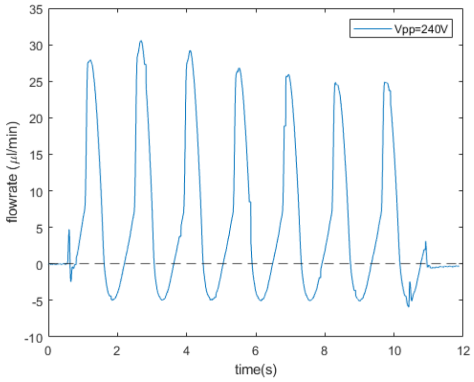

0.9	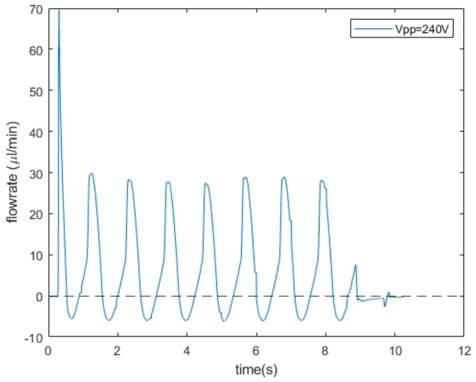Vpp=240V flowrate (μl/min) time(s) 70 60 50 40 30 20 10 0 -10 0 2 4 6 8 10 12
1	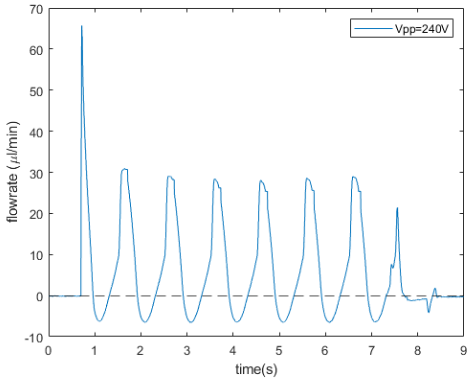Vpp=240V flowrate (μl/min) time(s) 70 60 50 40 30 20 10 0 -10 0 1 2 3 4 5 6 7 8 9
3	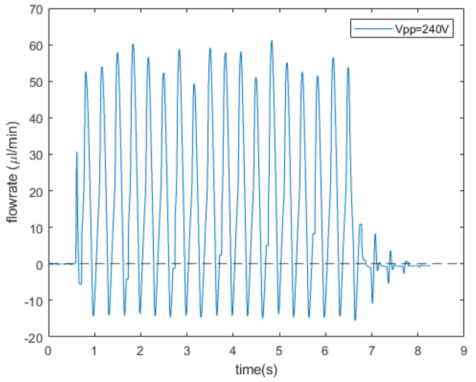Vpp=240V flowrate (μl/min) time(s) 70 60 50 40 30 20 10 0 -10 -20 0 1 2 3 4 5 6 7 8 9
4	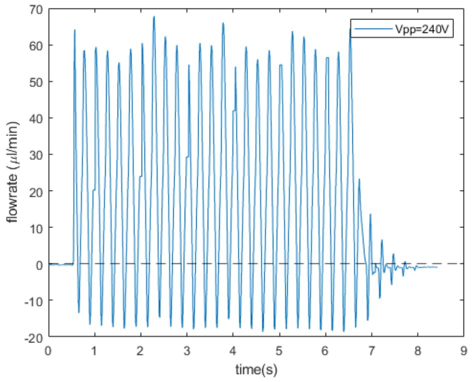Vpp=240V flowrate (μl/min) time(s) 70 60 50 40 30 20 10 0 -10 -20 0 1 2 3 4 5 6 7 8 9

5	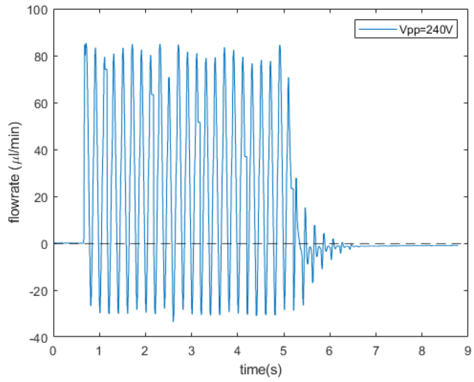Vpp=240V flowrate (μl/min) time(s) 100 80 60 40 20 0 -20 -40 0 1 2 3 4 5 6 7 8 9
6	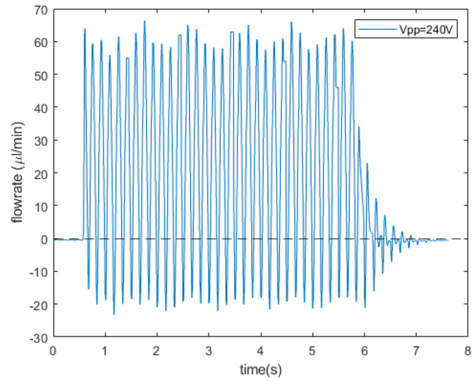Vpp=240V flowrate (μl/min) time(s) 70 60 50 40 30 20 10 0 -10 -20 -30 0 1 2 3 4 5 6 7 8
7	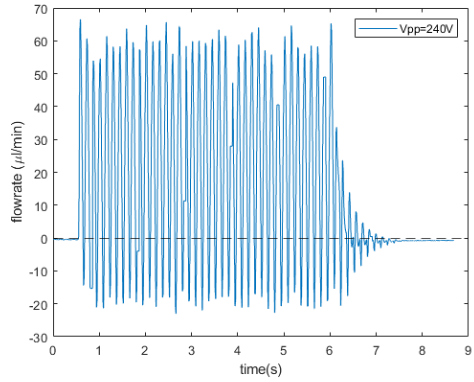Vpp=240V flowrate (μl/min) time(s) 70 60 50 40 30 20 10 0 -10 -20 -30 0 1 2 3 4 5 6 7 8 9
8	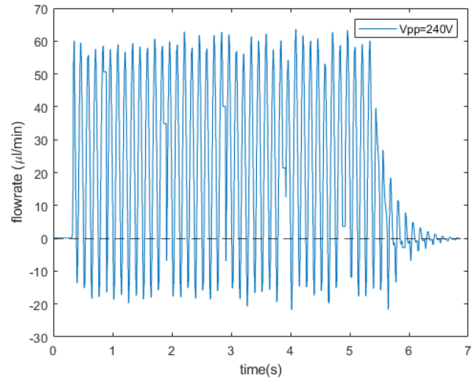Vpp=240V flowrate (μl/min) time(s) 70 60 50 40 30 20 10 0 -10 -20 -30 0 1 2 3 4 5 6 7

9	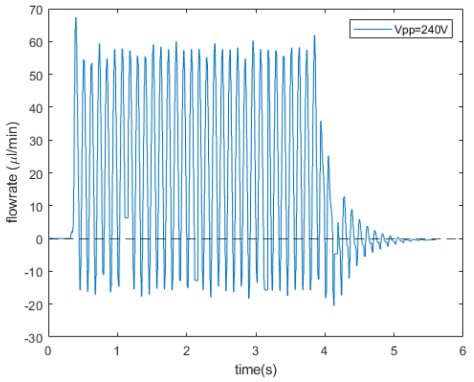Vpp=240V flowrate (μl/min) time(s) 70 60 50 40 30 20 10 0 -10 -20 -30 0 1 2 3 4 5 6
10	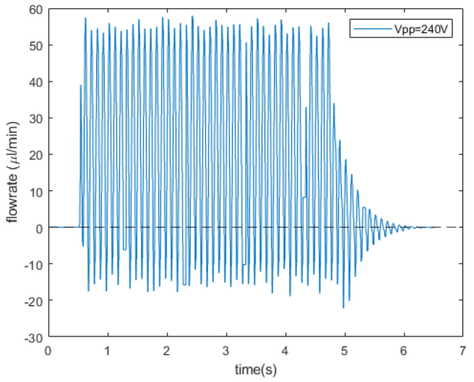Vpp=240V flowrate (μl/min) time(s) 60 50 40 30 20 10 0 -10 -20 -30 0 1 2 3 4 5 6 7
11	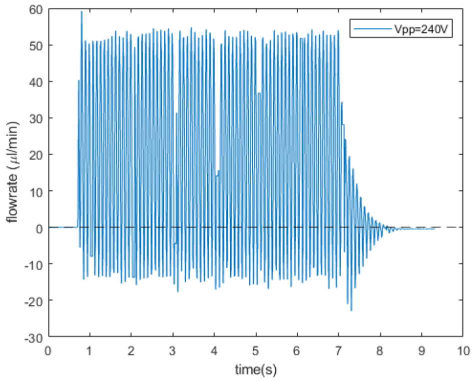Vpp=240V flowrate (μl/min) time(s) 60 50 40 30 20 10 0 -10 -20 -30 0 1 2 3 4 5 6 7 8 9 10
12	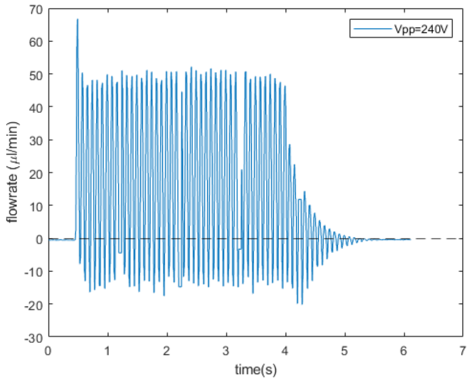Vpp=240V flowrate (μl/min) time(s) 70 60 50 40 30 20 10 0 -10 -20 -30 0 1 2 3 4 5 6 7

13	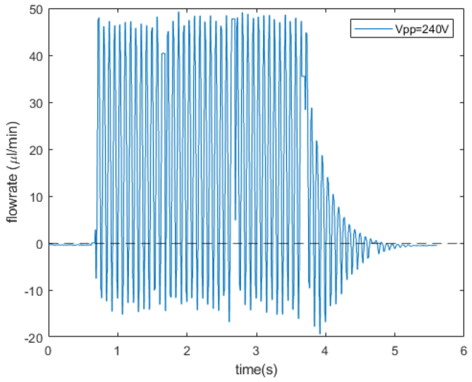 Vpp=240V flowrate (μl/min) time(s) 50 40 30 20 10 0 -10 -20 0 1 2 3 4 5 6
14	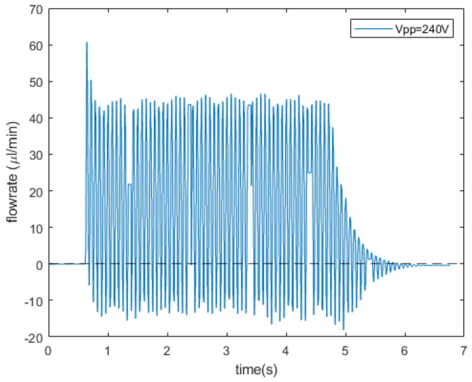 Vpp=240V flowrate (μl/min) time(s) 70 60 50 40 30 20 10 0 -10 -20 0 1 2 3 4 5 6 7
15	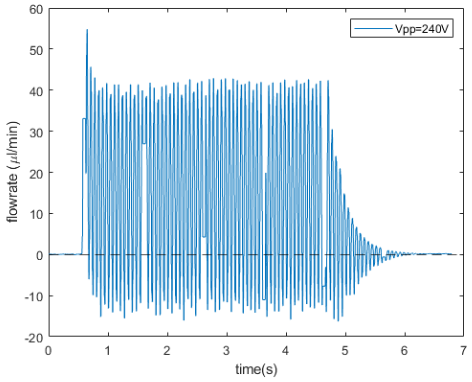 Vpp=240V flowrate (μl/min) time(s) 60 50 40 30 20 10 0 -10 -20 0 1 2 3 4 5 6 7
16	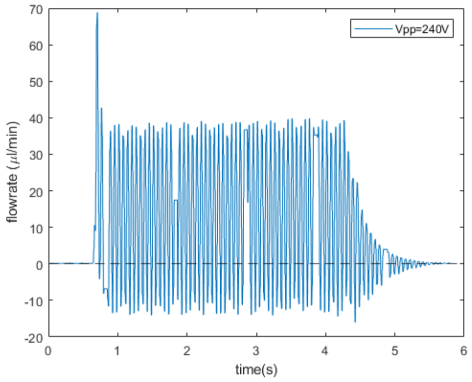 Vpp=240V flowrate (μl/min) time(s) 70 60 50 40 30 20 10 0 -10 -20 0 1 2 3 4 5 6

17	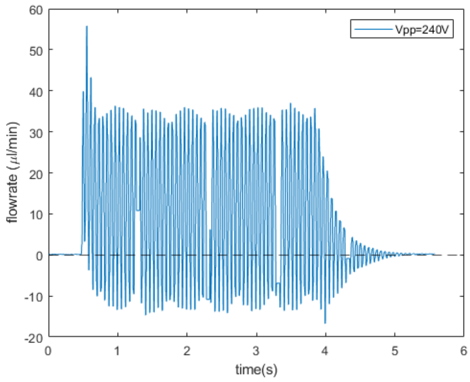Vpp=240V flowrate (μl/min) time(s) 60 50 40 30 20 10 0 -10 -20 0 1 2 3 4 5 6
18	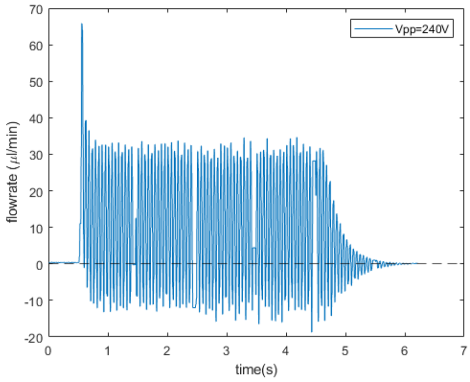Vpp=240V flowrate (μl/min) time(s) 70 60 50 40 30 20 10 0 -10 -20 0 1 2 3 4 5 6 7
19	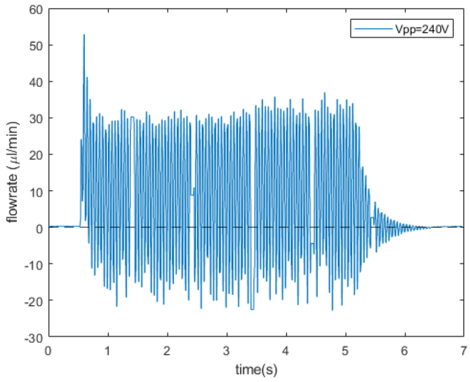Vpp=240V flowrate (μl/min) time(s) 60 50 40 30 20 10 0 -10 -20 -30 0 1 2 3 4 5 6 7
20	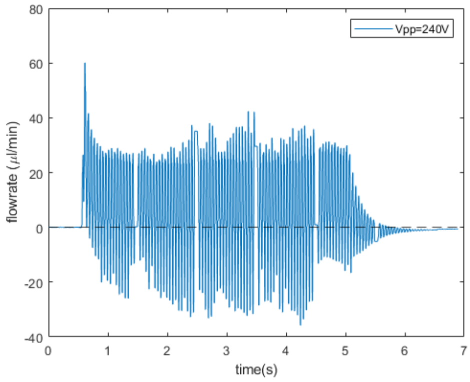Vpp=240V flowrate (μl/min) time(s) 80 60 40 20 0 -20 -40 0 1 2 3 4 5 6 7

21	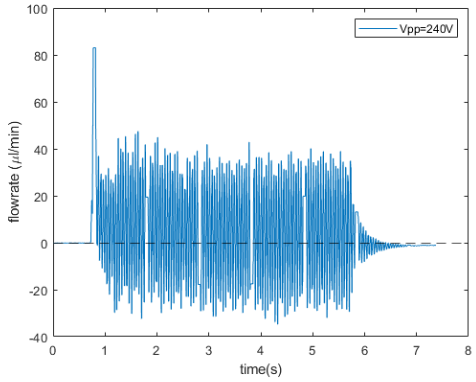Vpp=240V flowrate (μl/min) 100 80 60 40 20 0 -20 -40 0 1 2 3 4 5 6 7 8 time(s)
23	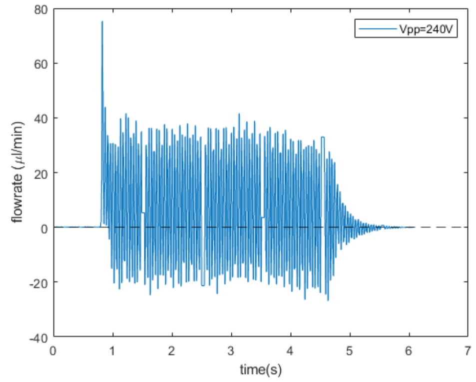Vpp=240V flowrate (μl/min) 80 60 40 20 0 -20 -40 0 1 2 3 4 5 6 7 time(s)
25	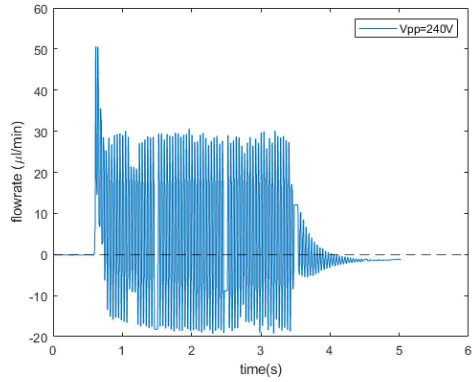Vpp=240V flowrate (μl/min) 60 50 40 30 20 10 0 -10 -20 0 1 2 3 4 5 6 time(s)
27	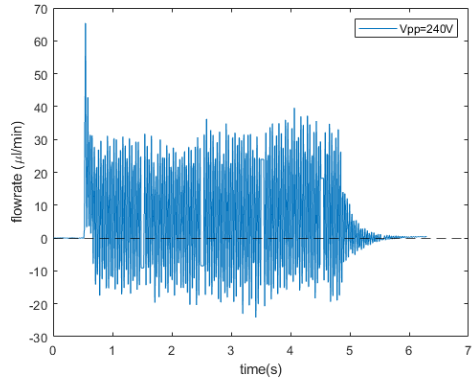Vpp=240V flowrate (μl/min) 70 60 50 40 30 20 10 0 -10 -20 -30 0 1 2 3 4 5 6 7 time(s)

29	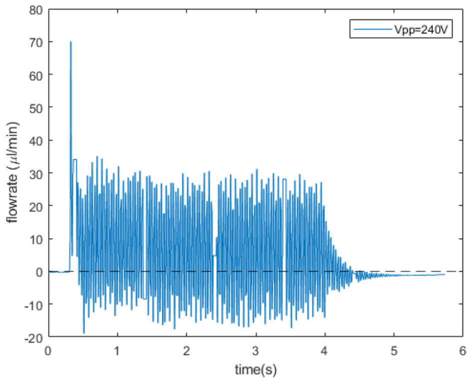Vpp=240V flowrate (μl/min) time(s) 80 70 60 50 40 30 20 10 0 -10 -20 0 1 2 3 4 5 6
31	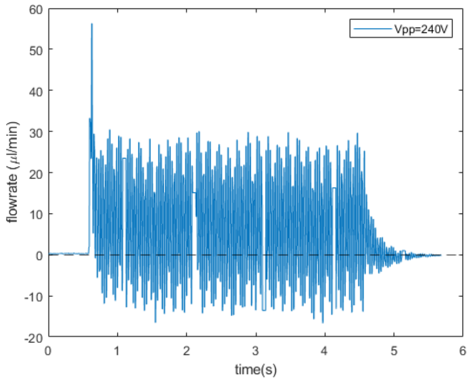Vpp=240V flowrate (μl/min) time(s) 60 50 40 30 20 10 0 -10 -20 0 1 2 3 4 5 6
33	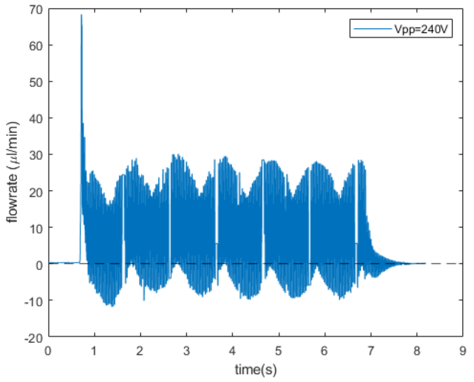Vpp=240V flowrate (μl/min) time(s) 70 60 50 40 30 20 10 0 -10 -20 0 1 2 3 4 5 6 7 8 9
35	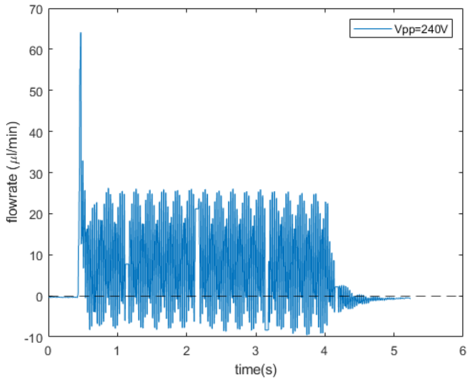Vpp=240V flowrate (μl/min) time(s) 70 60 50 40 30 20 10 0 -10 0 1 2 3 4 5 6

<table>
<tr><td>40</td><td>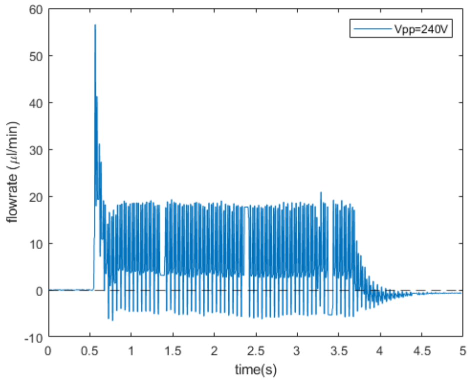
Vpp=240V
flowrate (μl/min)
time(s)
60
50
40
30
20
10
0
-10
0
0.5
1
1.5
2
2.5
3
3.5
4
4.5
5</td></tr>
<tr><td>50</td><td>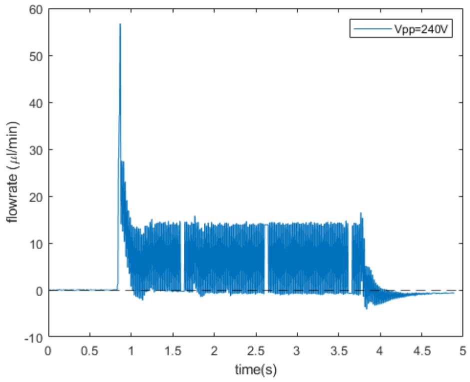
Vpp=240V
flowrate (μl/min)
time(s)
60
50
40
30
20
10
0
-10
0
0.5
1
1.5
2
2.5
3
3.5
4
4.5
5</td></tr>
<tr><td>60</td><td>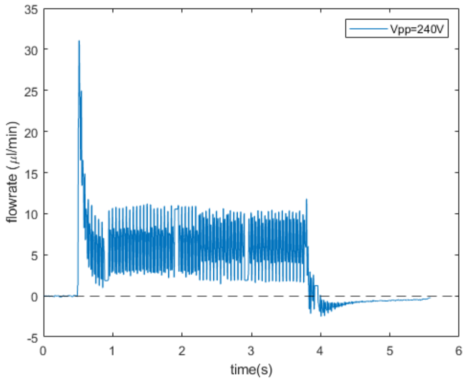
Vpp=240V
flowrate (μl/min)
time(s)
35
30
25
20
15
10
5
0
-5
0
1
2
3
4
5
6</td></tr>
<tr><td>70</td><td>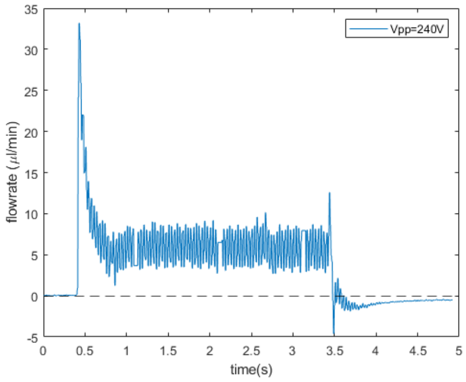
Vpp=240V
flowrate (μl/min)
time(s)
35
30
25
20
15
10
5
0
-5
0
0.5
1
1.5
2
2.5
3
3.5
4
4.5
5</td></tr>
</table>

80	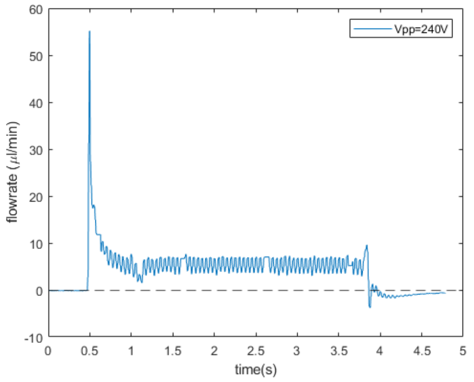Vpp=240V flowrate (μl/min) time(s) 60 50 40 30 20 10 0 -10 0 0.5 1 1.5 2 2.5 3 3.5 4 4.5 5
90	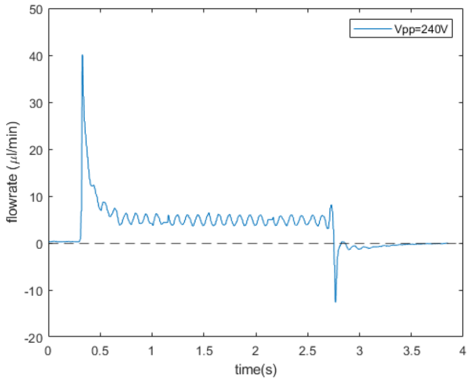Vpp=240V flowrate (μl/min) time(s) 50 40 30 20 10 0 -10 -20 0 0.5 1 1.5 2 2.5 3 3.5 4
100	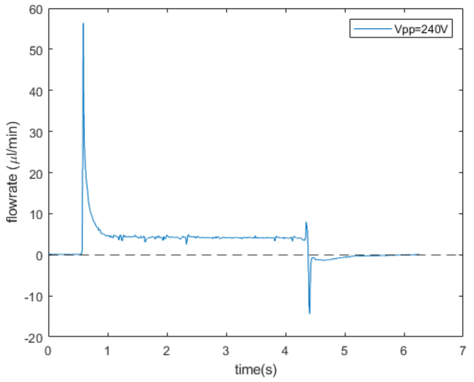Vpp=240V flowrate (μl/min) time(s) 60 50 40 30 20 10 0 -10 -20 0 1 2 3 4 5 6 7

Flow rate - voltage characterization

The following results were measured with applied sinusoidal voltage with 5Hz frequency.

Peak to peak voltage (V)	Image
150	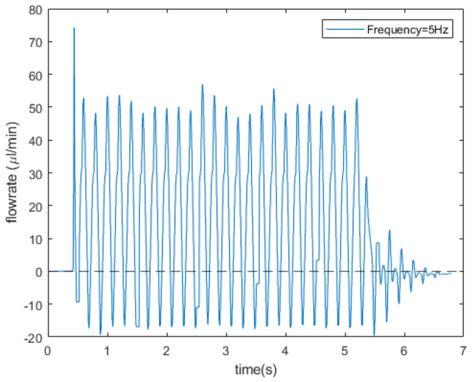
170	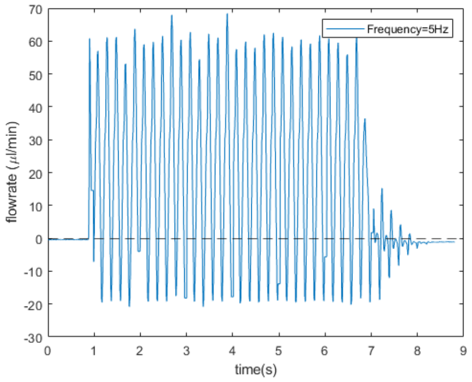
190	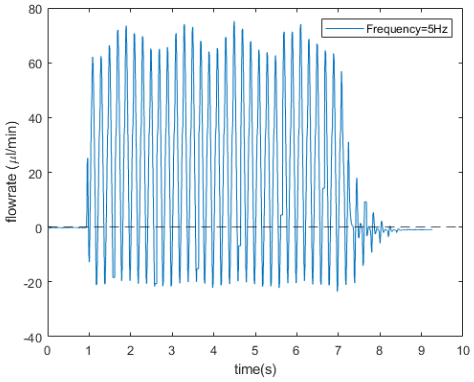
210	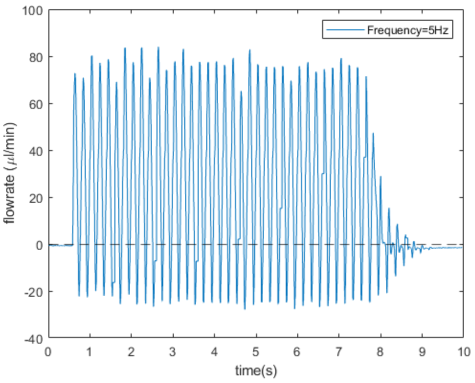

230	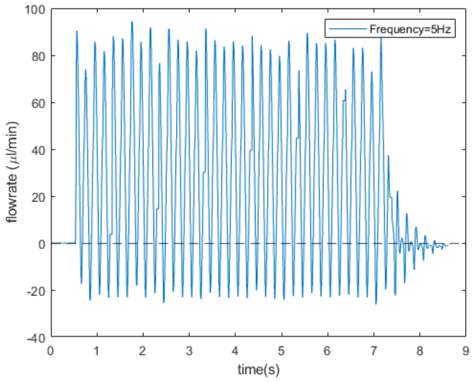Frequency=5Hz flowrate (μl/min) time(s) 100 80 60 40 20 0 -20 -40 0 1 2 3 4 5 6 7 8 9

Flow rate - Backpressure characterization

The following results were measured with 240 Vpp applied sinusoidal voltage with 5Hz frequency.

Backpressure (mbar)	Image
0	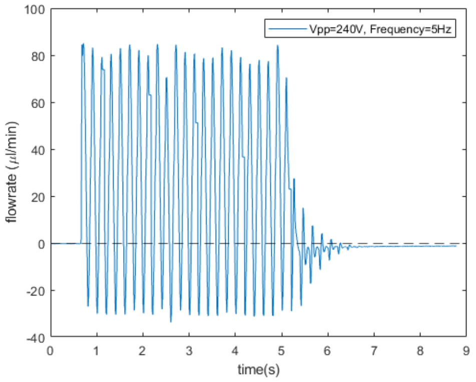
9	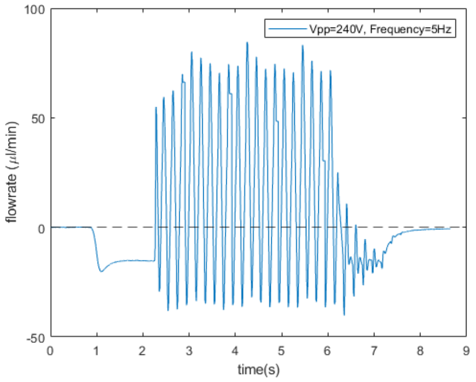
14	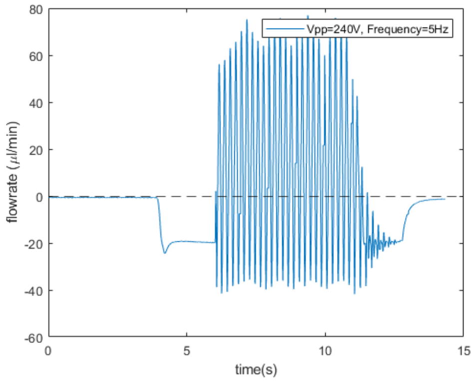
19	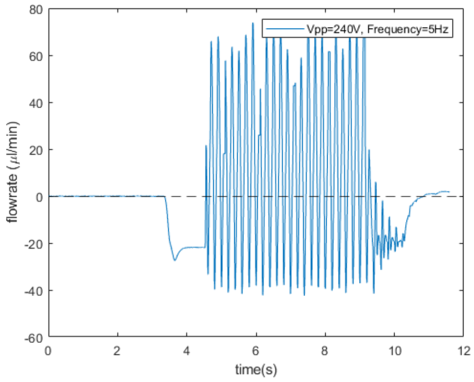

22	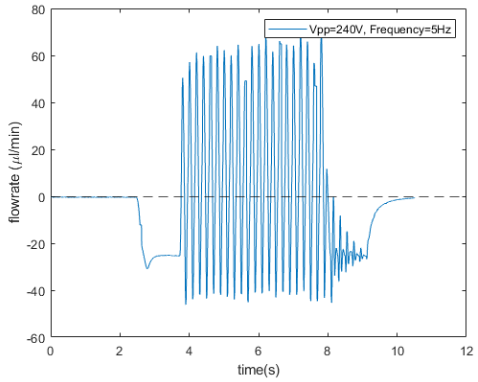Vpp=240V, Frequency=5Hz flowrate (μl/min) time(s) 80 60 40 20 0 -20 -40 -60 0 2 4 6 8 10 12
29	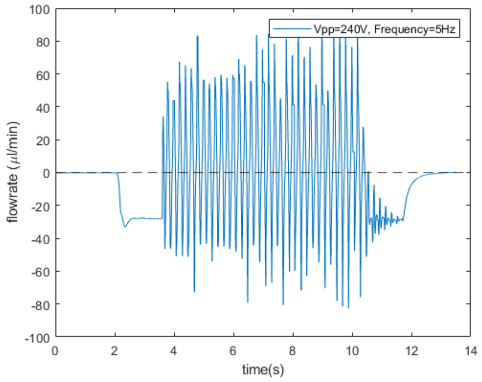Vpp=240V, Frequency=5Hz flowrate (μl/min) time(s) 100 80 60 40 20 0 -20 -40 -60 -80 -100 0 2 4 6 8 10 12 14
33	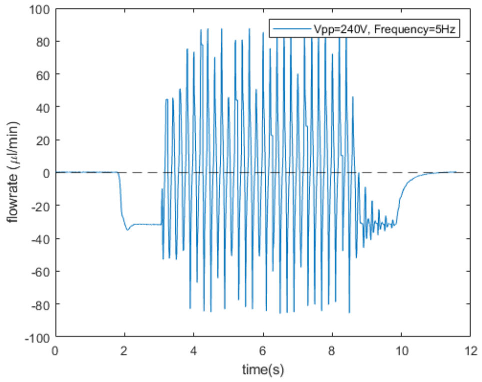Vpp=240V, Frequency=5Hz flowrate (μl/min) time(s) 100 80 60 40 20 0 -20 -40 -60 -80 -100 0 2 4 6 8 10 12
37	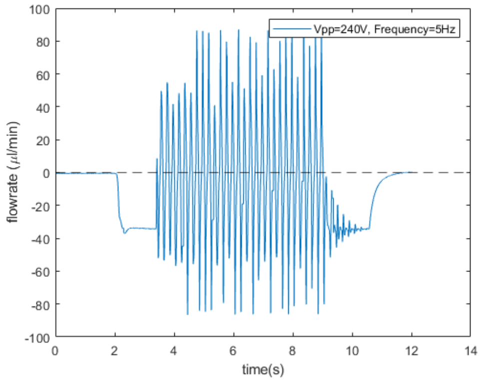Vpp=240V, Frequency=5Hz flowrate (μl/min) time(s) 100 80 60 40 20 0 -20 -40 -60 -80 -100 0 2 4 6 8 10 12 14

43	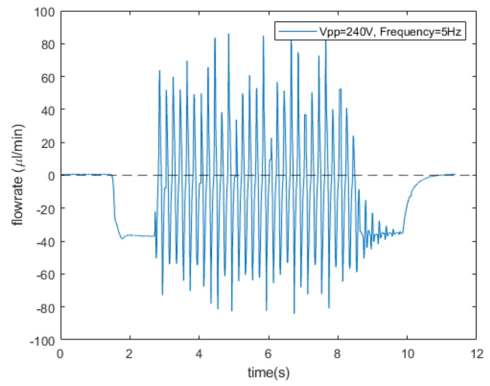Vpp=240V, Frequency=5Hz flowrate (μl/min) 100 80 60 40 20 0 -20 -40 -60 -80 -100 0 2 4 6 8 10 12 time(s)

B.0.4. MATLAB code for equivalent RLC model analysis

```
% Parameters
mu = 2.04e-3; % Viscosity of IPA (Pa·s)
L = 9.1e-3 * 2+14e-3;  % Channel length (m)
r = 0.75e-3; % Channel radius (m)
rho = 785; % IPA density (kg/m^3)
Dchamber = 28e-3; % Chamber diameter (m)
Dbrass = 28e-3; % Brass diameter (m)
DPZT = 25e-3; %PZT film diameter(m)
E_brass = 100e9; % Young's modulus of brass (Pa)
t_brass = 0.25e-3; % Thickness of brass membrane (m)
v_brass = 0.34; % Poisson's ratio of brass
E_PZT = 60e9; % Young's modulus of PZT-5H (Pa)
t_PZT = 0.26e-3; % Thickness of PZT film (m)
v_PZT = 0.31; % Poisson's ratio of PZT-5H

% Channel and Chamber Calculations
Dchannel = r * 2; % Channel diameter (m)
Schannel = pi * r^2; % Channel cross-sectional area (m^2)
A = pi * (Dchamber / 2)^2; % Chamber area (m^2)
Q0 = 18.83; % Flow rate achieved at resonance frequency (uL/min)

% Flexural Rigidity and Structural Calculations
D_Bending_brass = E_brass * t_brass^3 / (12 * (1 - v_brass^2)); % Flexural rigidity (N·m)
K_brass = 8 * D_Bending_brass / (Dbrass / 2)^2; % Spring constant of brass membrane (N/m)

% Piezoelectric film
D_Bending_PZT = E_PZT * t_PZT^3 / (12 * (1 - v_PZT^2)); % Flexural rigidity (N·m)
K_PZT = 8 * D_Bending_PZT / (DPZT / 2)^2; % Spring constant of brass membrane (N/m)
K = K_brass + K_PZT;

% Fluid Resistance and Inductance
R = 128 * mu * L / (pi * Dchannel^4) + 2.8e8; % Fluid resistance (Pa·s/m^3)
L_fluid = rho * L / Schannel; % Fluid inductance (kg/m^4)

% Compliance Calculation
C = A^2 / K; % Capacitance (m^5/N)

% Resonance Frequency Calculation
omega0 = 1 / sqrt(L_fluid * C); % Natural frequency (rad/s)
f0 = omega0 / (2 * pi); % Natural frequency in Hz
disp(['Resonance␣frequency:␣', num2str(f0), '␣Hz']);

% Frequency Range for Plotting
omega = 0.1:0.01:700; % Frequency range (rad/s)
ratio = omega / omega0; % Frequency ratio

% Damping Factor Calculation
xi = R / 2 * sqrt(C / L_fluid); % Damping factor

% Flow Rate Calculation (Analytical Oscillator Model)
Q = Q0 * 2 * xi .* sqrt(ratio.^2 ./ ((1 - ratio.^2).^2 + (2 * xi * ratio).^2));

% Plotting Results
f = omega / (2 * pi); % Convert omega to frequency in Hz
hold on;
plot(f, Q, ':'); % Plot flow rate vs frequency
xlabel('Frequency␣(Hz)');
ylabel('Average␣flowrate␣(\mu{}l/min)', 'Interpreter', 'tex');
set(gca, 'XScale', 'log'); % Set X-axis to log scale
legend('Experimental␣results', 'Equivalent␣RLC␣system␣model');
xlim([0.1 100]); % Limit the x-axis range
```

Listing B.1: MATLAB Code for Flow Rate vs Frequency

B.0.5. MATLAB code for theoretical PZT film displacement

```matlab

% PZT Material Parameters (from the table)
E11 = 60e9;          % Young's Modulus of PZT (Pa)
S11 = 1/E11;         % Compliance constant of PZT (m^2/N)
d31 = -350e-12;      % Piezoelectric constant of PZT (V/N)
v = 0.31;            % Poisson's ratio of PZT
hp = 0.26e-3;        % Thickness of PZT layer (m)
r1 = 25e-3 / 2;      % Radius of PZT layer (m)
V = 100:1:240;       % Applied voltage (V), from 100 to 240 with a step of 1

% Membrane Material Parameters (from the table)
Em = 100e9;          % Young's Modulus of the membrane (Pa)
Sm = 1/Em;           % Compliance constant of the membrane (m^2/N)
hm = 0.25e-3;        % Thickness of the membrane (m)
r2 = 28e-3 / 2;      % Radius of the membrane (m)

% Calculation of constants C1, C2, and C3 for theoretical displacement
C1=3*d31*hm*S11*Sm*(hm+hp);
C2=4*S11*hp*hm^3*Sm+6*S11*hm^2*hp^2*Sm+4*S11*hm*hp^3*Sm+1/2*hp^4*Sm^2*(1+v)+2*hm^4*S11^2/(1+v);
C3=4*S11*hp*hm^3*Sm+6*S11*hm^2*hp^2*Sm+4*S11*hm*hp^3*Sm+hp^4*Sm^2*(1+v);

% Theoretical central displacement calculation w(r)
w=(C1*(2*r1^2*log(r1/r2))*V)*1e6/(C2-C3*(r1/r2)^2+1/2*hp^4*Sm^2*(1+v)*(r1/r2)^4); %um

% Plotting the voltage-displacement curve
plot(V, w)
```

Listing B.2: MATLAB code for theoretical PZT film displacement

B.0.6. Simulation results of piezoelectric actuator central displacement in COMSOL Multiphysics

The following results were achieved when the frequency of the sinusoidal voltage was 5 Hz.

Peak to peak voltage (V)	**Displacement field, Z-component (mm)**
100	0.030186584775277796
110	0.03318098252423664
120	0.036198748182521154
130	0.03921328725035082
140	0.04224025857375002
150	0.04524696955731602
160	0.048312363452420876
170	0.051280265788819515
180	0.05432805238949205
190	0.05734627752242129
200	0.06032722807226581
210	0.0634042761042264
220	0.06640224336926005
230	0.06940959347663839
240	0.07240515045636202